Measurement of Jet Production in Proton Antiproton Collisions with the DØ Detector

von

Lotte Wilke

Diplomarbeit in Physik

vorgelegt der

Fakultät für Mathematik, Informatik und Naturwissenschaften
der Rheinisch-Westfälischen Technischen Hochschule Aachen

im Dezember 2004

angefertigt im

3. Physikalischen Institut A
Prof. Dr. Thomas Hebbeker

Contents

Abstract

In this diploma thesis the jet production in proton antiproton collisions is studied using data from the DØ detector. The data analysed was taken during Run II of the TEVATRON collider at a center of mass energy of 1.96 TeV. The integrated luminosity of the data sample used is $112 \pm 7\,\mathrm{pb}^{-1}$. The analyzed jets have been reconstructed using a cone algorithm with a radius of 0.7.

In the first part of this analysis the inclusive jet cross section $d\sigma/dp_T$ is studied in five different ranges of the pseudorapidity η. The data is compared to a next to leading order QCD calculation and to a PYTHIA Monte Carlo prediction. A good agreement between data and theory is found for most of the η regions. However, for $0.5 < |\eta| < 1.5$ the next to leading order prediction is slightly below the measurement. This might indicate an incomplete understanding of the detector in this region.

The multijet production is studied in the second part. Here the rate of events with n jets ($n = 3..6$) is compared to the two-jet-event rate. The data is unfolded from measured jets in the detector to jets on particle level with a Bayesean approach. The results are compared to ALPGEN and PYTHIA Monte Carlo predictions. The agreement is reasonable, although a tendency for an excess in the ALPGEN Monte Carlo prediction is seen.

The dominant source for the uncertainties of these results is the precision by which the calorimeter energy scale is known.

Zusammenfassung

In dieser Diplomarbeit wird die Jet-Produktion in Proton-Antiproton-Kollisionen anhand von Daten des DØ-Experiments studiert. Die analysierten Daten, die im Run II des TEVATRON bei einer Schwerpunktsenergie von 1.96 TeV aufgenommen wurden, entsprechen einer integrierten Luminosität von $112 \pm 7\ \mathrm{pb}^{-1}$. Die analysierten Jets wurden mit Hilfe eines Cone-Algorithmus mit einem Radius von 0.7 rekonstruiert.

Im ersten Teil der Analyse wird eine Studie des inklusiven Jet-Wirkungsquerschnitts $d\sigma/dp_T$ in fünf verschiedenen Regionen der Pseudorapidität η vorgestellt. Die Daten werden sowohl mit einer Next-To-Leading-Order-Berechnung verglichen als auch mit einer PYTHIA Monte-Carlo-Simulation. In einem Großteil der η-Regionen wird eine gute Übereinstimmung festgestellt. Im Bereich $0.5 < |\eta| < 1.5$ liegt die Next-To-Leading-Vorhersage jedoch leicht unterhalb der Messung. Dies kann auf ein unvollständiges Verständniss des Detektors in dieser Region hindeuten.

Im zweiten Teil wird die Multijet-Produktion untersucht. Dabei wird die Produktionsrate von n Jets ($n = 3..6$) relativ zur 2-Jet-Rate bestimmt. Die gemessenen Daten werden mit Hilfe eines Ansatzes nach Bayes von Detektor-Level auf Teilchen-Level entfaltet. Die sich daraus ergebenden Resultate werden mit einer ALPGEN und mit einer PYTHIA Monte-Carlo-Vorhersage verglichen. Die Übereinstimmung ist gut, wobei in den ALPGEN Monte-Carlo-Vorhersagen ein leichter Überschuss festgestellt wird.

Die Hauptursache für die Fehler dieser Messung ist die Ungenauigkeit mit der die Jet-Energie-Kalibration bekannt ist.

Chapter 1

Introduction

Particle physics tries to describe basic constituents of matter and their interactions. In this context the atempt is made to set up theories that are as simple as possible. Ideally, a theory would be found describing all phenomena. Up to now it has been possible to unify two of the three fundamental forces in the Standard Model. The third force of the Standard Model, the strong force, can still not be combined with the two other forces, namely the electromagnetic and weak force. Moreover the strong interaction, descibed by Quantum Chromo Dynamics (QCD), is the most difficult to compute in theoretical terms. That is why experimental checks of QCD are indispensable.

At hadron colliders like the TEVATRON jet production is of particular interest since jets originate mainly from the dominant QCD processes. Analysing these processes should give valuable information on the degree to which the detector and the physics behind these events are understood. Deviations from the measurement could be indicators for new physics.

In this diploma thesis, jet production at the proton antiproton collider TEVATRON is studied. The data used in this analysis was taken with the DØ detector at a centre of mass energy of 1.96 TeV and corresponds to a luminosity of 112 pb^{-1}.

In this chapter an introduction to the Standard Model of particle physics is given. Some aspects of Quantum Chromo Dynamics are explained in further detail, since this is the theory describing jet production. The experimental setup of the DØ detector is explained in Chapter 2. A definition of what is understood as jet in this analysis is given in Chapter 3. In Chapter 4 data reconstruction and the selection of events and jets are illustrated. The measurement of the inclusive cross section is described in Chapter 5. The results of the multijet measurement are given in Chapter 6.

At this place units and conventions are set once and for all. "Natural units" of high energy physics are used by setting the important constants to one:

$$\hbar = 1 \quad \text{and} \quad c = 1\,, \tag{1.1}$$

instead of

$$\hbar = 1.0546 \cdot 10^{-34}\,\mathrm{Js} \quad \text{and} \quad c = 2.998 \cdot 10^{8}\,\mathrm{m/s}\,. \tag{1.2}$$

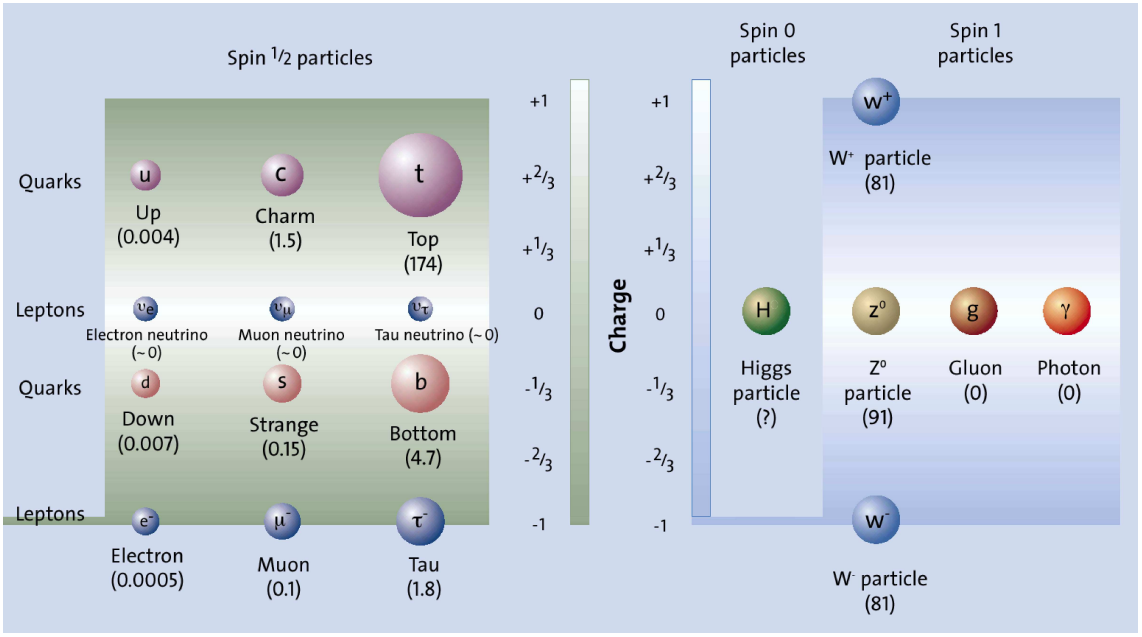

Figure 1.1: *The Standard Model particles. In brackets the mass of the particles in* GeV *[1].*

As unit for the energy (E) the Electronvolt (eV) is used. This is the energy a particle with the charge $e = 1.602 \cdot 10^{-19}$ C (i.e. the charge of an electron) gains, if it traverses a potential difference of 1 V. This results in the following units for the commonly used variables. Let m be the synonym for mass, p for momentum, t for time and l for length.

$$[m] = [p] = \text{eV}\,, \tag{1.3}$$

$$[t] = [l] = \text{eV}^{-1}\,. \tag{1.4}$$

1.1 The Standard Model

The Standard Model is the theory describing all point like elementary particles and forces discovered up to now. The elementary particles can be divided into two groups, fermions and bosons. "Fermions" are spin $\frac{1}{2}$ particles. Matter surrounding us is made up of fermions. "Bosons", are spin 1 particles, responsible for the forces between fermions. Every particle in the standard model has an antimatter counterpart with the same mass but opposite quantum numbers (this means e.g. opposite charge).

Within the Standard Model, twelve fermions exist. They can be further divided into two subgroups, leptons and quarks, which themselves again can be divided into three "families" (see Fig. 1.1). In the world surrounding us only particles from the first family occur. This is due to the fact that the particle mass increases from one to the next family. The heavier particles decay via the electroweak force into lighter particles. Whereas leptons like the electron can exist on their own, quarks cannot. "Glued" together by the strong interaction they can only exist within hadrons (see Section 1.1.1).

Three types of forces are described in the Standard Model. They are carried by different types of bosons (See Tab. 1.1). The photon (γ) is the carrier of the electromagnetic force, the $W^{\pm}$ and Z^0 bosons are the carriers of the weak force and the gluons (g) are the carriers of the strong interaction. The electromagnetic and the weak force can be unified into the electroweak force.

The Standard Model is governed by symmetries. Each symmetry under a transformation is equivalent to a conserved property, this is stated by Noether's theorem [2]. For example the invariance under translations in space leads to conservation of momentum, or invariance under rotation leads to conservation of angular momentum. These two are global symmetry transformations i.e. they do not depend on time and space. Different to this, the Standard Model uses local gauge transformations depending on space and time. The corresponding gauge symmetry is $\mathrm{SU}(2)_L \times \mathrm{U}(1)_Y \times \mathrm{SU}(3)_C$.

The electroweak theory developed by Glashow, Salam and Weinberg combines the electromagnetic and the weak force. It is described by an $\mathrm{SU}(2)_L \times \mathrm{U}(1)_Y$ symmetry. The lefthanded fermions are grouped in weak isospin doublets ($T = \frac{1}{2}$, $T_3 = \pm\frac{1}{2}$), righthanded fermions build a weak isospin singlet ($T = 0$). Only the doublet fermions couple with the gauge fields W^a ($a = 1, 2, 3$) of the $\mathrm{SU}(2)_L$ symmetry. The gauge field B of the $\mathrm{U}(1)_Y$ symmetry couples to all fermions, where Y denotes the hypercharge ($Y = 2(Q - T_3)$. The observed boson fields are linear combinations of the fields W^a and B, with

$$\begin{aligned} W^{\pm} &= \frac{1}{\sqrt{2}}\left(-W^1 \pm iW^2\right) , \\ Z^0 &= -B\sin\theta_W + W^3\cos\theta_W , \\ A &= B\cos\theta_W + W^3\sin\theta_W . \end{aligned} \tag{1.5}$$

The photon (γ) is described by A and θ_W is the Weinberg angle which has to be measured since it can not be determined from theory. Other than the photon and gluons, the $W^{\pm}$ and Z^0 bosons do have a mass, which is in contradiction to the local $\mathrm{SU}(2)_L \times \mathrm{U}(1)_Y$ gauge symmetry on which the Standard Model is based. This theory predicts massless force carriers. To solve this problem the higgs field is introduced. One of the main goals of today's particle accelerators is to find the higgs boson.

The strong interaction is described by an $\mathrm{SU}(3)_C$ symmetry, described in more detail in Section 1.1.1. Attempts are made to unify the electroweak and the strong force in a Grand Unified Theory (GUT). But this leads to various problems, e.g. for the simple unified gauge group SU(5) [3], baryon number would have to be violated, which has not been observed yet.

For a more detailed description of the Standard Model see e.g. [4] or [5].

1.1.1 Quantum Chromo Dynamics

The strong force is described by Quantum Chromo Dynamics and acts only on quarks, not on leptons. Quarks come in six flavours grouped in three families, where each contains an up type quark with electric charge $q = \frac{2}{3}e$ and a down type quark with $q = -\frac{1}{3}e$. The

Force	relative strength	range	force carrier
strong force	1	10^{-15} m	8 gluons (g)
weak force	10^{-5}	10^{-17} m	$W^{\pm}$, Z
electromagnetic force	10^{-2}	∞	photon (γ)

Table 1.1: *The forces described by the Standard Model.*

quark model was developed in 1964 by Gell-Mann and Zweig. At this time it was only a model to describe baryons and mesons. Baryons are three quark states and mesons quark antiquark states. Thus they all have an electric charge which is an integer multiple of e (including zero).

The first quarks were discovered in 1969 at the Stanford Linear Accelerator. Electrons with a momentum of 16 GeV were shot onto nucleons. It was detected that the nucleons consist of pointlike particles, called partons. The strange quark had been found indirectly before, bound in hadrons like the Λ and K^0. In 1974 the J/Ψ meson was found in two different experiments independently. This J/Ψ meson is a bound state of a charm (c) and anticharm ($\bar{c}$) quark. Similar to this the bottom (b) quark was observed in 1977 at Fermilab, bound in a meson. The new particle, a $b\bar{b}$ bound state, was called Υ. In 1995 the top (t) quark was discovered in proton antiproton collisions at the Fermilab in the Run I of the TEVATRON. Since it is so heavy, it decays too fast to form bound states like mesons. It decays almost instantaneously into a bottom quark and a $W^{\pm}$ boson.

A problem arose because baryons like the Δ^{++} were found. Δ^{++} consists of three up quarks with the same spin ($\Delta^{++} = u^{\uparrow}u^{\uparrow}u^{\uparrow}$). Thus all quark quantum numbers are equal and the wave function is symmetric under exchange of two quarks. This violates Pauli's Principle, requiring an antisymmetric wave function for particles with half-integer spin. In order to fulfil this principle, a new quantum number, colour, was introduced in 1964. The colour can have three different values (e.g. r = red, b = blue, g = green). All observed particles are colourless, i.e. they either consist of colour and anticolour (mesons) or all three colours/anticolours (baryons). This means that they are invariant under $SU(3)_C$ colour transformations (= rotations in colour space). Now an antisymmetric wavefunction for the Δ^{++} can be constructed:

$$\Delta^{++} = \frac{1}{\sqrt{6}}\left(u_r^{\uparrow}u_g^{\uparrow}u_b^{\uparrow} + u_g^{\uparrow}u_b^{\uparrow}u_r^{\uparrow} + u_b^{\uparrow}u_r^{\uparrow}u_g^{\uparrow} - u_g^{\uparrow}u_r^{\uparrow}u_b^{\uparrow} - u_b^{\uparrow}u_g^{\uparrow}u_r^{\uparrow} - u_r^{\uparrow}u_b^{\uparrow}u_g^{\uparrow}\right) . \quad (1.6)$$

Every quark exists in three colours and colour is a conserved quantity similar to the electric charge ($\Rightarrow$ colour charge). Experimental evidence for the fact that three colours exist is for example given by the cross section ratio for $e^+e^- \rightarrow$ hadrons and $e^+e^- \rightarrow \mu^+\mu^-$.

Dirac's equation for the wave function Ψ of a free quark is given by:

$$(i\gamma_\mu \partial^\mu - m)\Psi = 0 , \quad (1.7)$$

where μ indicates the four space-time coordinates, γ_μ are the dirac matrices with rank 4×4, ∂_μ the gradient in space-time coordinates. Ψ has twelve components, four components of a dirac spinor all having three colour components:

$$\Psi = \psi(\mathbf{r}, t) \otimes \chi_C . \quad (1.8)$$

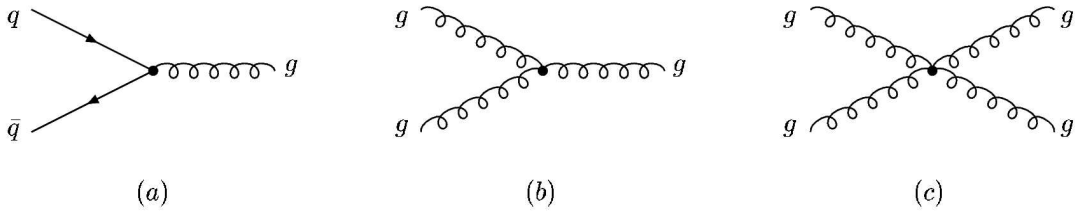

Figure 1.2: *The fundamental vertices of QCD. (a) shows quark gluon interaction, (b) and (c) show gluon self interaction.*

The dirac spinors have four entries, for particle and antiparticle with spin $+\frac{1}{2}$ and spin $-\frac{1}{2}$ respectively. The colour spinors are defined by:

$$\chi_r = \begin{pmatrix} 1 \\ 0 \\ 0 \end{pmatrix}, \quad \chi_g = \begin{pmatrix} 0 \\ 1 \\ 0 \end{pmatrix} \quad \chi_b = \begin{pmatrix} 0 \\ 0 \\ 1 \end{pmatrix}. \tag{1.9}$$

Dirac's equation must be invariant under local $SU(3)_C$ transformations:

$$\Psi' = e^{i\phi_s(x)t^s} \cdot \Psi \,. \tag{1.10}$$

t^s are the eight generators of the $SU(3)_C$. To obtain this invariance a gluon field has to be introduced. This leads to eight different gluons which have a colour combination of colour and anticolour. They build a colour octet, e.g.:

$$r\bar{g},\ r\bar{b},\ g\bar{b},\ g\bar{r},\ b\bar{r},\ b\bar{g},\ r\bar{r} - g\bar{g},\ r\bar{r} + g\bar{g} - 2b\bar{b}\,.$$

A colour singlet ($r\bar{r} + g\bar{g} + b\bar{b}$) would lead to an infinite range of the strong force, which has not been observed.

Due to the fact that gluons as force carriers have colour, they can interact with themselves. Thus there are three fundamental vertices of QCD (see Fig. 1.2). The coupling constant of QCD α_s is a measure of the interaction strength. In lowest order the values of α_s at two different energy scales μ_0 and μ are related by:

$$\alpha_s(\mu) = \frac{\alpha_s(\mu_0)}{1 - \beta_0^s \alpha_s(\mu_0) \ln(\mu^2/\mu_0^2)}\,. \tag{1.11}$$

The absolute value of $\alpha_s(\mu_0)$ has to be measured. In contrast to Quantum Electro Dynamics (QED) the coefficient β_0^s is negative:

$$\beta_0^s = \frac{1}{6\pi} \cdot (N_F - 16.5) < 0\,, \tag{1.12}$$

where N_F is the number of quarkflavours of quarks with $m \ll \mu$. The negative number is due to the selfcoupling. This leads to the fact that the coupling constant decreases with the increasing energy scale, the asymtotic freedom of α_s. The coupling constant has been measured at the Z-peak to be $\alpha_s(m_Z) = 0.1187 \pm 0.0013$ [6]. This is large compared to the electromagnetic coupling with $\alpha(m_Z) \approx 1/129$. The coupling is greater than one for

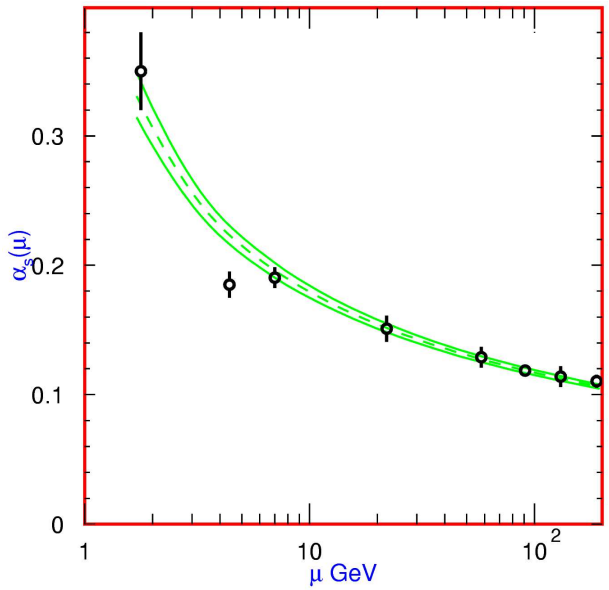

Figure 1.3: *Measured values of the coupling constant $\alpha_s(\mu)$ at different energy scales μ [6].*

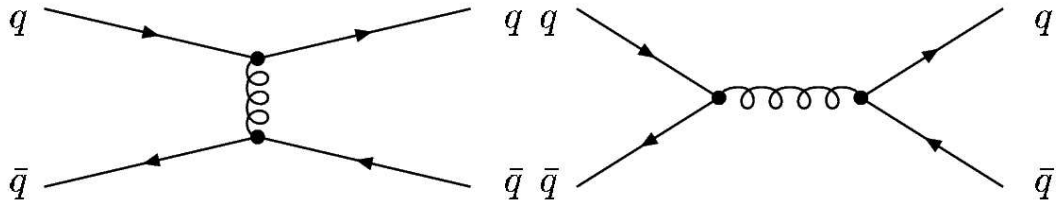

Figure 1.4: *The leading order Feynman diagrams for quark antiquark scattering.*

small energy. This leads to the fact that no free quarks can be observed, which is called "confinement". Perturbative calculations are thus only possible at large energies. The "running" of the coupling constant is shown in Fig. 1.3.

The most common case of hard interaction at hadron colliders is the scattering of one of the partons of the proton and one of the partons of the (anti)proton, respectively. The leading order (LO) Feynman diagrams for $q\bar{q} \rightarrow q\bar{q}$ are given in Fig. 1.4. The resulting cross sections are proportional to α_s^2. Next to leading order cross sections proportional to α_s^3 are based on Feynman diagrams like in Fig. 1.5.

1.1.2 Hadronisation

Since free quarks do not exist, the simple formula $q\bar{q} \rightarrow q\bar{q}$ does not describe the scattering process completely. Quarks and remnants of the proton and antiproton hadronise. This means that new quarks are created until all quarks are bound in mesons and baryons. This happens at a low energy scale thus the coupling constant is large. So hadronisation

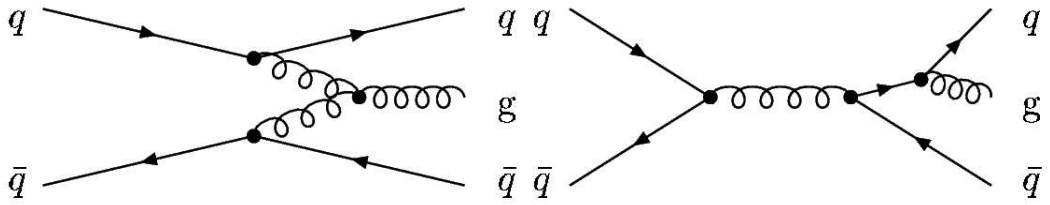

Figure 1.5: *Some next to leading order Feynman diagrams for quark antiquark scattering.*

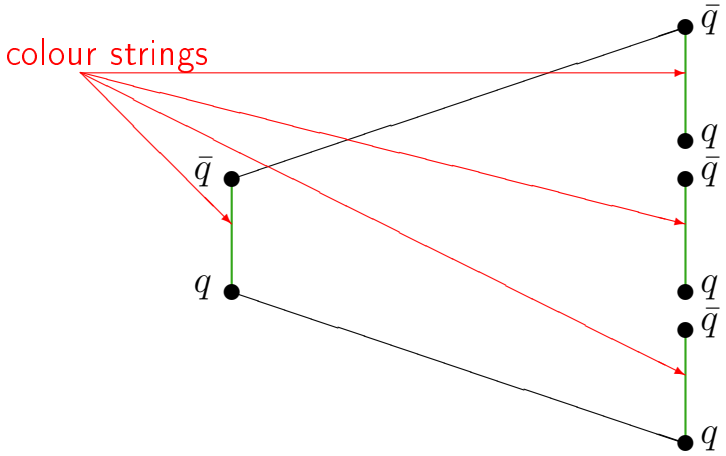

Figure 1.6: *Drawing to illustrate the idea of string fragmentation.*

can not be described by perturbative QCD. Different models have been developed for hadronisation. The Monte Carlo generator PYTHIA uses the LUND string fragmentation model. The idea of this model is that the two quarks produced in the interaction move apart from each other. The strong interaction increases with the distance of the two quarks, comparable to a rubber band (colourstring) between the two quarks. If the quarks are far enough from each other, the rubber band breaks and a new pair of quark and antiquark is produced (see Fig. 1.6). This is repeated until all quarks are bound in mesons. All fragmentation models have many open parameters which have to be adjusted to describe the data from experiments.

1.2 Physics at hadron colliders

As mentioned above, protons and antiprotons are not point-like particles like electrons and positrons. They do have a substructure. They do not only consist of three valencequarks, namely two up quarks (u_v) and one down quark (d_v), but also of seaquarks and gluons being generated and annihilated by vacuum fluctuations constantly. All these particles are called partons. When protons and antiprotons collide, in most cases only two of the partons interact in a hard scattering process while the remnants of the (anti)proton hadronise and

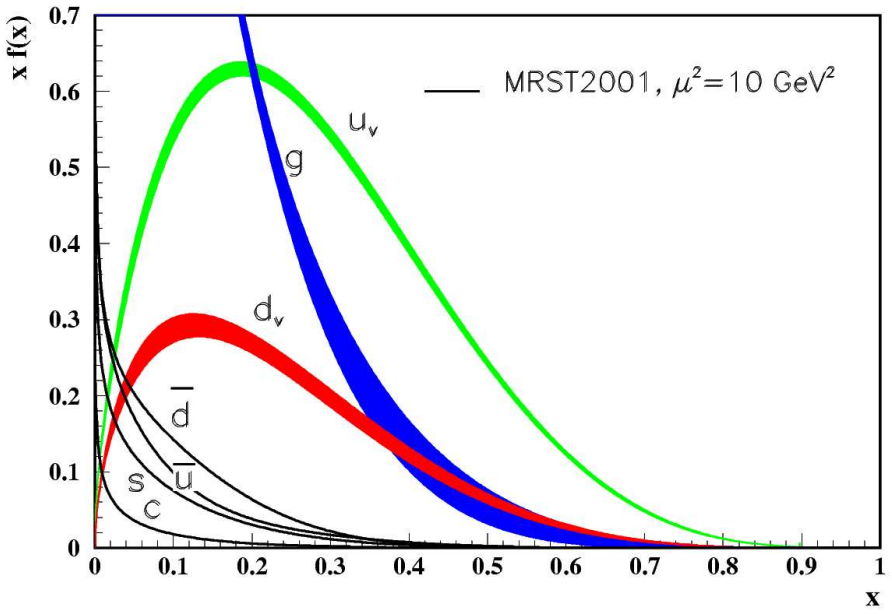

Figure 1.7: *Distribution of $x \cdot f(x)$ with the parton distributions $f = u_v, d_v, \bar{u}, \bar{d}, s, c, g$, the subscrtipt v denotes the valence quarks. The MRST2001 parameterisation is used and the energy scale is $\mu^2 = 10$ GeV^2 [7].*

form jets with a very small angle to the beam pipe. The two partons involved in the hard scattering carry only a fraction of the (anti)proton momentum. Thus not the complete centre of mass energy is used in the interaction. The fraction of the total momentum of the proton is commonly called x. In Fig. 1.7 the distribution of $xf(x)$ depending on x is shown at an energy scale of $\mu^2 = 10$ GeV^2, where $f(x)$ is the parton distribution. Here the MRST2001 parameterisation is used, but other parametisations, like CTEQ, also exist.

Because the hard interacting partons do not necessarily have the same momentum, the centre of mass frame is not the laboratory frame. Thus the interaction is boosted along the z axis with an unknown velocity.

1.2.1 Coordinate systems and angles

A right handed coordinate system is used with the z axis along the beam pipe and the y axis pointing upward. The origin of this system is the centre of the detector. An alternative coordinate system is commonly used at hadrons colliders. This system exploits the cylindrical symmetry of the detector. The polar angle is called θ and the azimuthal angle φ. The distance from the beam pipe is called r. More commonly the direction of particles is given in φ and y or η, the rapidity or pseudorapidity, respectively:

$$\begin{aligned} y &= \frac{1}{2}\ln\left(\frac{E+p_z}{E-p_z}\right) \\ &\approx \eta = -\ln\left(\tan\left(\frac{\theta}{2}\right)\right) \quad (E \approx p \gg m) \ . \end{aligned} \tag{1.13}$$

This variable is used instead of θ because $\Delta\eta$ is invariant under Lorentz transformations along the z axis. This is very convenient, as the momentum along the z-axis is not always zero for the proton antiproton centre of mass system . Another variable, called seperation

$$\Delta R = \sqrt{(\Delta\eta)^2 + (\Delta\varphi)^2} \tag{1.14}$$

is thus also invariant under such transformations and under rotations around the z axis, since φ does not depend on z. For the same reason the transverse momentum:

$$p_T = \sqrt{p_x^2 + p_y^2} \tag{1.15}$$

is commonly used.

1.2.2 Luminosity and cross section

The measure of the probability for a certain outcome of a collision is the total cross section σ:

$$\sigma = \frac{N}{\mathcal{L}_{int}}\,, \tag{1.16}$$

where N denotes the number of events with this specific outcome. $\mathcal{L}_{int}$ is the integrated luminosity, a measure for the total number of proton antiproton collisions. The instantaneous luminosity $\mathcal{L}_{inst}$ is the time derivative of the total luminosity. It can be determined if all beam parameters are known:

$$\mathcal{L}_{inst} = \frac{f\, n_B\, n_p\, n_{\bar{b}}}{4\pi\, \sigma_x\, \sigma_y}, \tag{1.17}$$

where f is the rotational frequency of the bunches in the collider, n_B the number of proton and antiproton bunches, n_p and $n_{\bar{p}}$ the number of protons and antiprotons in a bunch. σ_x and σ_y are the widths of a gaussian shaped bunch in x and y direction. Since most of these parameters are not known very well, the luminosity is determined with a reference process, see Chapter 2.

Often one is interested in the differential cross section $d\sigma/dx$. Here x can be one or more variables, e.g. angle or momentum. The differential cross section gives information on the distribution of the cross section in this variable. The inclusive cross section is measured as a function of the transverse momentum p_T.

The cross section has the dimension of length squared. Usually it is measured in barn ($1\,\mathrm{b} = 10^{-24}\,\mathrm{cm}^2 = 10^{-28}\,\mathrm{m}^2$). Thus the integrated luminosity is measured in reciprocal barn (b^{-1}). The instantaneous luminosity is commonly measured in $\mathrm{cm}^{-2}\cdot\mathrm{s}^{-1}$and not in $\mathrm{b}^{-1}\cdot\mathrm{s}^{-1}$.

Different cross sections for hadron colliders are given in Fig. 1.8. One can see that for jets with a transverse momentum greater than 3% of the centre of mass energy (corresponding to 60 GeV at the TEVATRON) the cross section is much higher than for other Standard Model processes. It appears that the cross section for $b\bar{b}$ production is higher although it should be included in the jet cross section. This is due to the constraint on the jets transverse momentum. No such cut is required for the $b\bar{b}$ cross section. This shows that QCD is the dominant process at hadron colliders and thus needs further investigation.

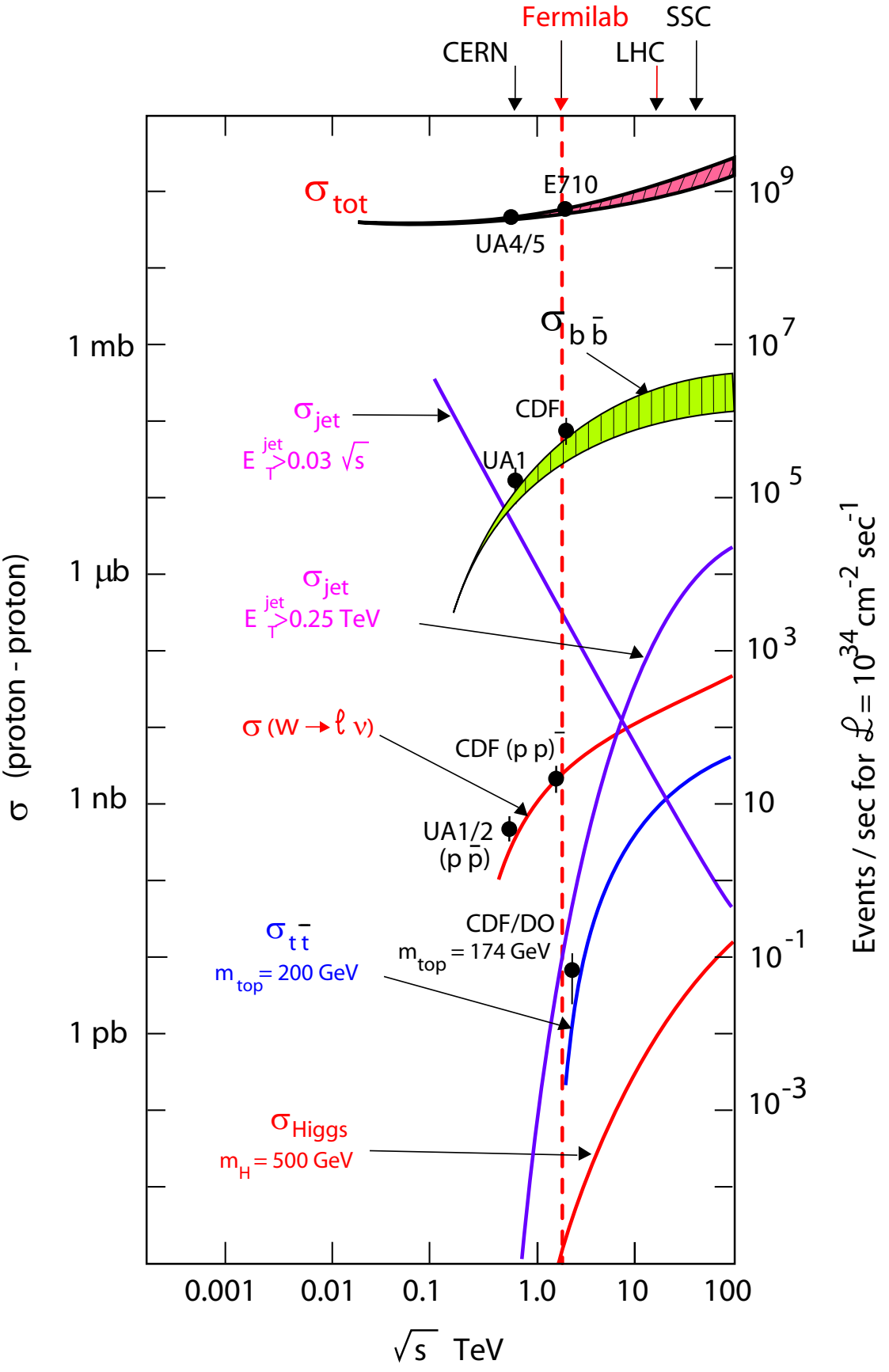

Figure 1.8: *Cross section and even rates at hadron colliders for different processes as a function of the centre of mass energy.*

Chapter 2

Experimental Setup

This chapter gives an introduction to the accelerator chain at Fermilab and the DØ detector which recorded the data used for this analysis. The different subsystems of the DØ detector responsible for the reconstruction of jets, which are of major interest in this analysis, are described in further detail.

2.1 Tevatron

To reach a centre of mass energy of 1.96 TeV protons as well as antiprotons have to be accelerated to 980 GeV. In order to gain such a high energy, a long chain of accelerators (Fig.2.1) is needed. Additionally, the antiprotons have to be produced as they do not occur naturally.

At the beginning a Cockcroft-Walton accelerator brings negatively charged hydrogen ions up to an energy of 750 keV. These get accelerated to an energy of 400 MeV by a linear accelerator (LINAC). When the Hydrogen-Ions enter the Booster the two electrons are stripped off leaving a positively charged proton. After reaching an energy of 8 GeV in the Booster the protons enter the main injector, which has a circumference of 3.2 km. Here they are accelerated to an energy of 120 GeV. In order to produce antiprotons these protons are shot onto a nickel target producing many different secondary particles, some of them antiprotons. For 20 antiprotons one needs to have 1 million protons. These antiprotons with an average energy of 8 GeV then circulate in the main injector in the opposite direction to the protons. When enough antiprotons are accumulated in the main injector, they are accelerated to an energy of 150 GeV before they are injected into the Tevatron ring where reach their final energy of 0.98 TeV.

In order to keep the protons and antiprotons on a circular orbit superconducting magnets cooled by liquid helium are necessary. With an electric current of more than 400 A in the coils these magnets can create magnetic fields of 4.2 T.

The Tevatron ring has a circumference of 6.4 km and is divided into six segments (AØ to FØ). At FØ the main injector and the Tevatron are connected. The two high energy

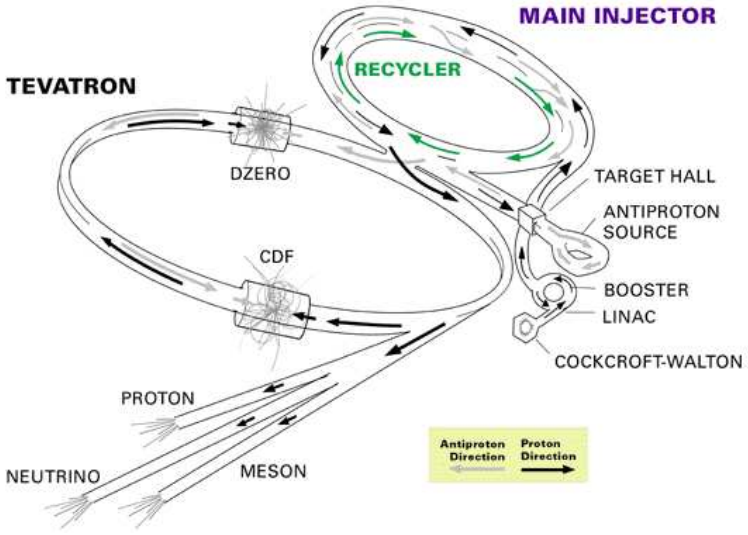

Figure 2.1: *The Fermilab accelerator chain [9]*

physics experiments CDF (Collider Detector Facility) and DØ are situated at BØ and DØ where the protons and antiprotons collide head on.

The protons and antiprotons are grouped into bunches containing approximately 10^{11} protons and 10^{10} antiprotons, respectively. Twelve bunches with a separation in time of 396 ns are called a bunch train. Three of these trains of protons and antiprotons are inside the TEVATRON ring at a time. These trains are separated by 7 μs. Because the protons and antiprotons travel with nearly the speed of light, bunch crossings occur at the two experiments with a rate of 1.7 MHz. Because the bunches lose particles, and since the luminosity is proportional to the amount of particles in one bunch, the luminosity decreases with time, with a half time of ≈ 10 h. After about one day the beams of protons and antiprotons are dumped and the detector is filled again with protons and antiprotons since the luminosity has become too small. The time between filling and dumping is called store.

2.2 The DØ detector

DØ is a multipurpose detector measuring the energy and momentum of electrons, muons and hadron jets with high precision (detailed description in [10] and [11]). It is 20 m long, 13 m high and has a mass of 5000 t. The detector was built in 1992 for the Run I of the TEVATRON in which the centre of mass energy was 1.8 TeV. Major upgrades were made for Run II which started in 2001.

Fig. 2.2 shows the main parts of the detector. The inner tracking system at the centre of the detector (gray) is situated in a solenoid coil which can produce a 2 T magnetic field. This magnet, which is new for Run II, makes it possible to measure the momentum of charged particles. Thus the vertex of the collision as well as the momentum of these

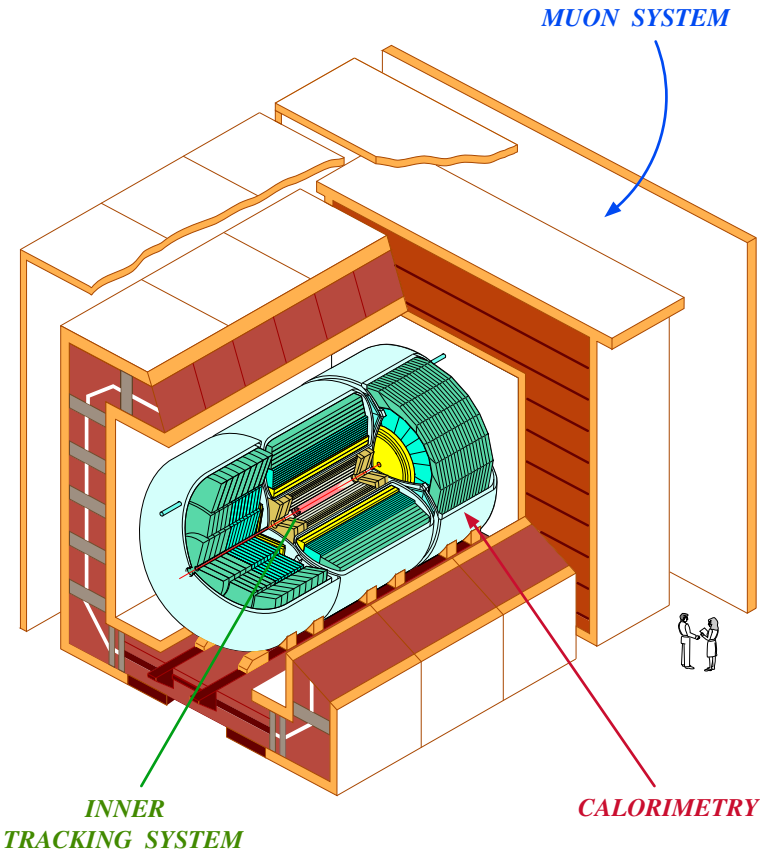

Figure 2.2: *A 3-dimensional view of the DØ detector[10].*

particles can be measured as they describe a curved track depending on the momentum and the strength of the magnetic field. Further outside the calorimeter follows (yellow and green). It is basically the same as in Run I, only changes to the readout electronics were made. The calorimeter measures the energy of electromagnetic particles such as electrons and photons and of hadrons which can be detected as hadronic jets in the detector. On the outside of the calorimeter a muon system with a 1.8 T toroid magnetic field follows. It was modified considerably for Run II, too. The muon system is the outermost system because muons at such high energies are the only particles which have not been absorbed up to this distance (except neutrinos, which cannot be detected at all). Other important parts of the detector not shown in Fig. 2.2 are the luminosity monitors and the forward proton detectors in the forward region. A 3 level Trigger system is used to select the relevant events.

2.2.1 The Inner Tracking System

The main task of the tracking system is to determine the vertices and to measure the momentum of the particles. The transverse momentum p_T of particles can be determined

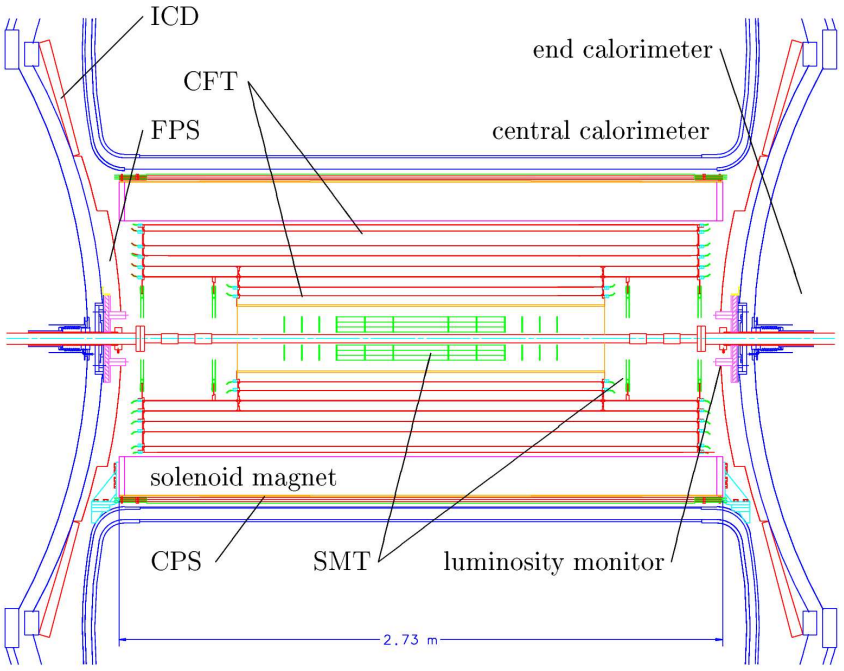

Figure 2.3: *Longitudinal view of the central part of the detector with tracking systems.*

by measuring the curvature of their tracks in the $r-\varphi$ plane. The momentum, magnetic field and radius are connected as follows:

$$r[\,\mathrm{m}] \;=\; \frac{p_T[\,\mathrm{GeV}]}{0.3B[\,\mathrm{T}]}\,. \tag{2.1}$$

Since the main error of this measurement of the transverse momentum is given by the spatial resolution, the relative error of the p_t measurement is proportional to the transverse momentum. The momentum resolution of the whole tracking system is given by:

$$\frac{\Delta p_T}{p_T} \;=\; 0.002 \cdot \frac{p_T}{\mathrm{GeV}}\,. \tag{2.2}$$

The full information of the track can be obtained by measuring the $r-z$ coordinate.

The DØ tracking system consists of a Silicon Vertex Detector, a Scintillating Fibre Tracker and a Solenoid. This can be seen in Figure 2.3.

Silicon Microstrip Tracker

The Silicon Microstrip Tracker (SMT) is the innermost part of the DØ experiment. Its task is to measure the position of vertices with a very high precision, in order to find secondary vertices produced by decaying bottom quarks and thus to distinguish them from other lighter quarks.

In Fig.2.4 one can see that the Silicon Microstrip Tracker consists of six barrel segments and twelve double-sided F disks, 4 of them sandwiched between the barrel segments and four single sided H segments. The barrel segments are 120 mm long in total.

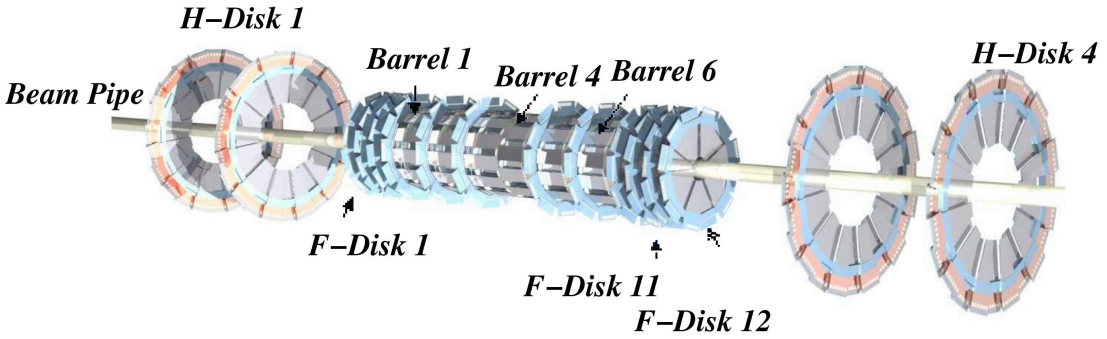

Figure 2.4: *The Silicon Microstrip Detector in the very centre of the detector.*

The SMT has 793.000 readout channels and can measure up to a pseudorapidity of $\eta = 3.0$ with an accuracy of 10 µm perpendicular and 100 µm parallel to the direction of the beam.

Central Fibre Tracker

The Central Fibre Tracker (CFT) consists of 74.000 scintillating fibres with a diameter of 835 µm. These fibres emit light with a wavelength of 530 nm which is visible green-yellow light. They are read out by Visible Light Photon Counters (VLPCs) with a quantum efficiency of 70%. To achieve this high efficiency for a single photon detection, the VLPCs have to be kept at a temperature of 7 K.

Eight concentric cylinders (Fig. 2.3) with radii between 19.5 cm and 51.5 cm support a doublet of fibres which are parallel to the beam pipe. The inner two cylinders are 1.71 m long and the outer six are 2.57 m long. Half of the cylinders support a doublet of fibres at a stereo angle between $\pm 2.0°$ and $\pm 3.0°$. The spatial resolution of these doublets is 100 µm perpendicular to the beam pipe.

Solenoid

The complete tracking system is embedded in a 2 T solenoid magnetic field with a stored energy of 5 MJ. This field is provided by a 2.73 m long superconducting two layer coil with a mean radius of 60 cm. By using two different kinds of conductors a highly uniform field is achieved without a field-shaping iron return yoke. The conductor with the higher current density is used towards the ends of the coil.

2.2.2 Calorimetry

The calorimeter is the most important instrument to measure jet properties. Particles like electrons, photons and hadrons lose their complete energy in the calorimeter. All of these particles build showers in the calorimeter. The main processes in which high energy electrons (positrons) and photons build showers are pair production and bremsstrahlung.

Particles like pions, Kaons, protons and neutrons interact inelastic with the absorber material, producing hadronic showers. These showers ionise the active medium, in the case of DØ liquid Argon. The ionisation is a measure of the energy of the shower.

By measuring this energy and the position in the calorimeter at which it was lost, one can reconstruct the energy and momentum of the electrons, photons or jets produced in the proton antiprotons interaction. The missing transverse energy is determined by adding up all momenta determined from the energy depositions in the calorimeter. In the x and y directions the momenta should add up to zero. If they do not, the missing part is called missing transverse Energy ($\not\!\!E_T$):

$$\not\!\!E = \sqrt{\left(\sum p_x\right)^2 + \left(\sum p_y\right)^2} . \tag{2.3}$$

The DØ Calorimeter is a Liquid Argon Calorimeter which is placed in three cryostats to keep the temperature at 78 K.

Preshower Detectors

For Run II the new solenoid magnet, having approximately 1 radiation length, required the insertion of so called preshower detectors into the 5.1 cm gap between the coil and the cryostat. It helps to identify electromagnetic objects and corrects the energy measured in the main calorimeter for effects of the solenoid.

The Central Preshower Detector (CPS) covers a pseudorapidity range of $|\eta| < 1.2$ and consists of three layers of scintillating fibres, one layer parallel to the beam pipe and two layers at stereo angles of 23°. The readout works with wavelength shifting fibres which are connected to Visible Light Photon Counters (VLPCs) via 10 m long clear light-guide fibres.

The Forward Preshower Detector (FPS) covers a pseudorapidity range of $1.4 < |\eta| < 2.5$ and is mounted on the inner surface of the End Calorimeters (EC). It is made of two layers of scintillating fibres with a layer of lead absorber (two radiation lengths) sandwiched between them.

Both of the preshower detectors are not used for the analysis yet but read out. Studies are made to test the Central Preshower Detector.

Liquid Argon Calorimeter

As mentioned above DØ uses a liquid argon calorimeter. Due to the very low temperature of the liquid argon the calorimeter has to be hosted in cryostats. Since the centre of the detector with the tracking system has to be accessible, three cryostats are needed (see Fig. 2.5). The middle one with the Central Calorimeter (CC) covering a pseudorapidity up to $|\eta| < 1.0$ and the two Endcap Calorimeters North and South (ECN / ECS) which extend the coverage up to a pseudorapidity of $|\eta| < 4.0$ (See Fig. 2.6). Liquid argon is used as active medium because it is radiation hard, relatively easy to calibrate and can

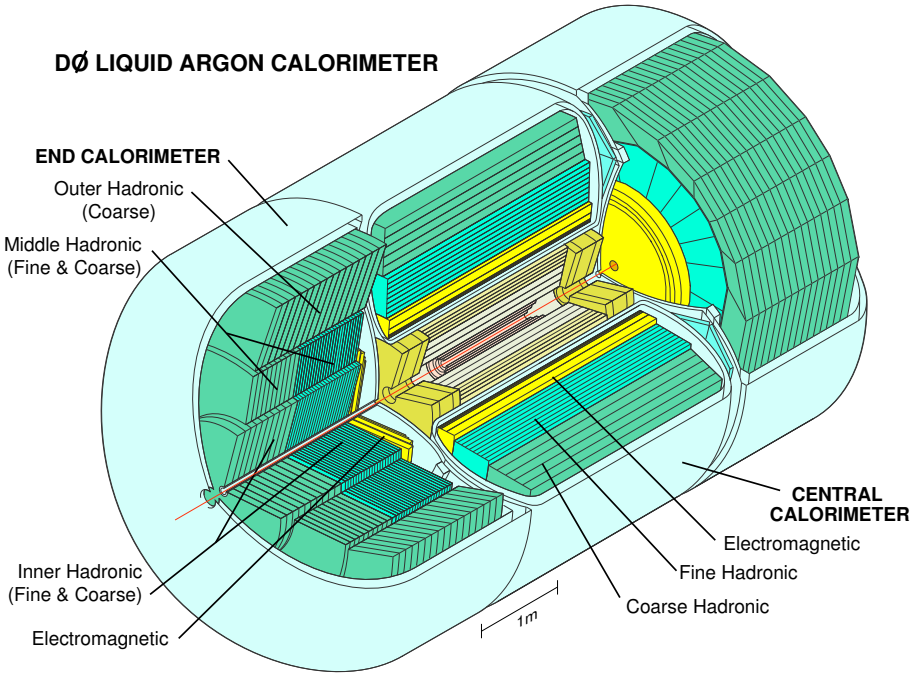

Figure 2.5: *The DØ Calorimeter, in yellow the electromagnetic part and in green the hadronic part [10].*

Figure 2.6: *A Photo of one of the DØ End cap Calorimeters, in the middle one can see the beam pipe[9].*

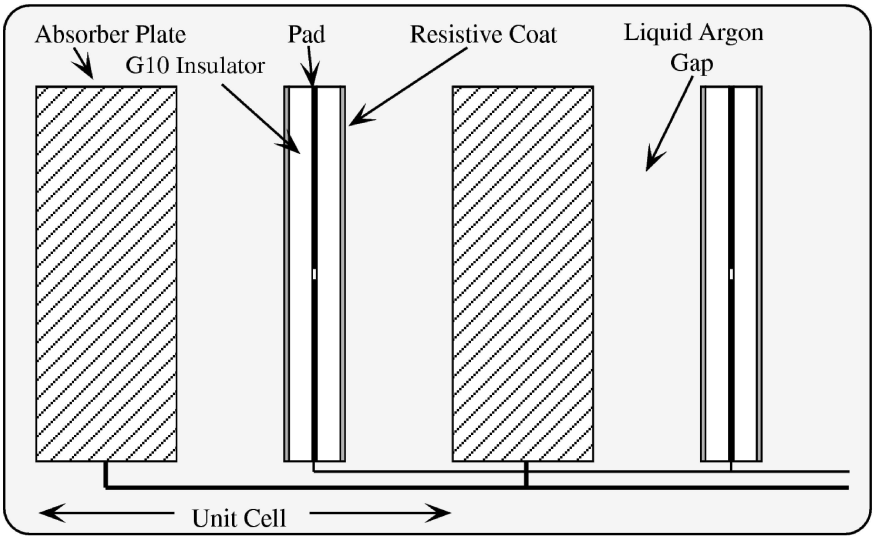

Figure 2.7: *An unit cell in the calorimeter [12].*

be segmented in small longitudinal as well as transverse cells. The main problem with a liquid argon calorimeter is that it has to be kept at a low temperature. Thus a cryostat is needed, making it almost impossible to access the calorimeter for repairs later on. A typical calorimeter cell is shown in Fig. 2.7. The absorber plate is grounded while the signal boards (pads with insulator and resistive coat) are connected to a positive high voltage of 2.0 kV to 2.5 kV. The corresponding electric field causes a drift time for the electrons of $\approx$ 450 ns to cross the 2.3 mm gap. The calorimeter can be divided into three different sections using different absorber materials (see Fig. 2.5). The innermost is the electromagnetic section which uses only 3 mm and 4 mm thick plates of very pure depleted uranium in the Central and Endcap Calorimeter respectively. The fine hadronic section is equipped with 6 mm thick uranium alloy with 2% niobium. Outside the coarse hadronic section uses 46.5 mm thick plates of copper or stainless steel for the Central Calorimeter and Endcap Calorimeter, respectively.

As shown in Fig. 2.8 the Central Calorimeter consists of three cylindrical shells with 32 electromagnetic modules in the inner ring and 16 fine and 16 coarse hadronic modules in the middle and outer shell. The boundaries of the modules are rotated so that projective ray encounters more than one of the gaps between the modules. The Endcap Calorimeter contains four different types of modules. In order to avoid dead spaces between the modules, there is only one electromagnetic module and one inner hadronic module (i.e. small distance to the beam pipe). There are 16 middle and outer hadronic modules building rings around the beam pipe.

The calorimeter modules are read out in pseudo-projective towers, i.e. the centres of the cells in one tower lie on a virtual ray coming from the centre of the detector. Fig. 2.9 shows a side view of the segmentation pattern of one quarter of the DØ detector. The electromagnetic section is divided into four layers in depth in the Central Calorimeter and Endcap Calorimeter. The fine hadronic sections consist of three and four layers,

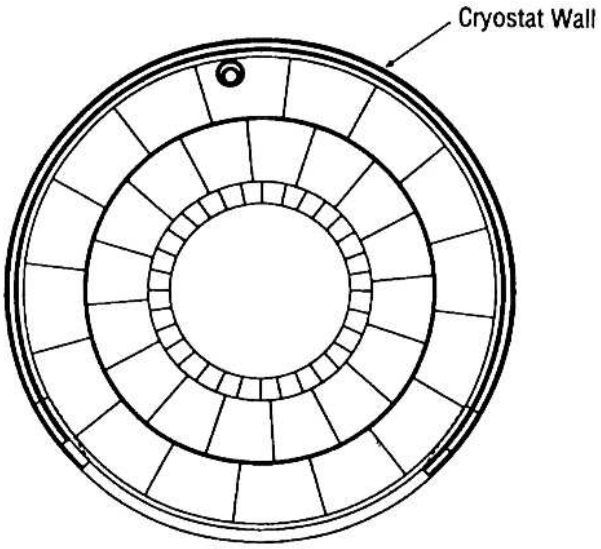

Figure 2.8: *End view of the central calorimeter with the arrangement of the different modules [10].*

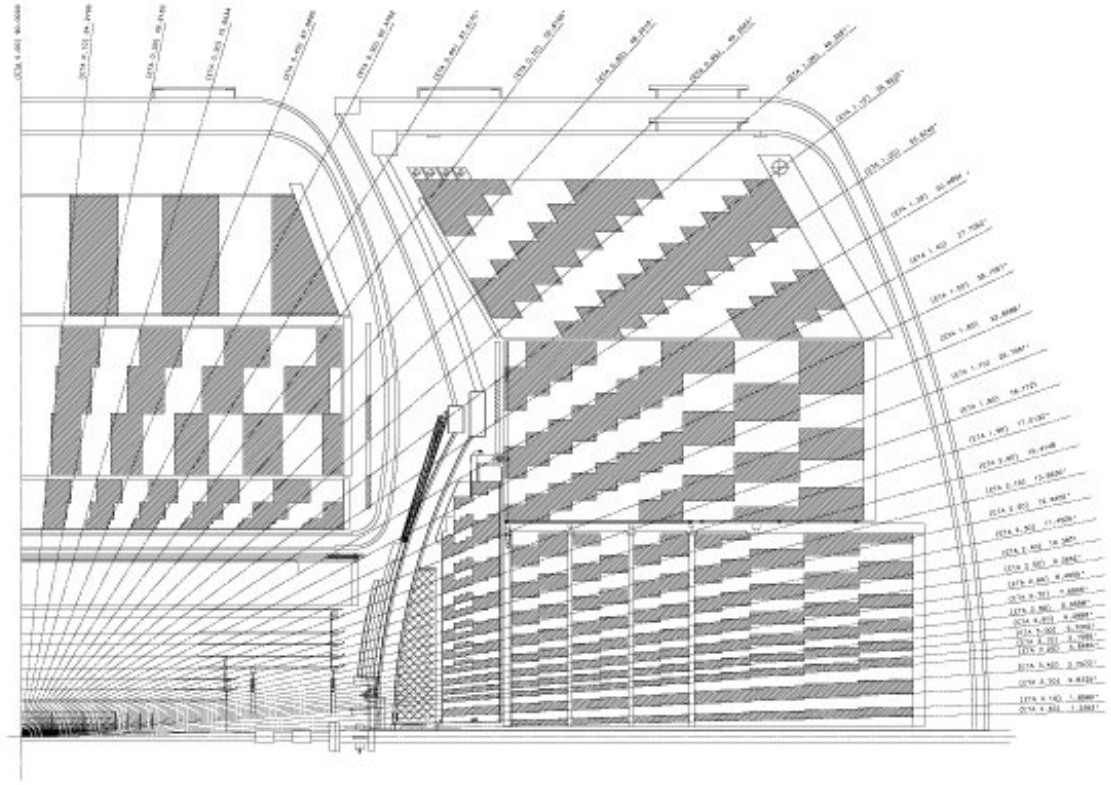

Figure 2.9: *Side view of one quarter of the calorimeter, the projective towers of the calorimeter can be seen well [13].*

respectively, while the coarse hadronic sections have one or three layers. The layers are segmented in transverse size in $\Delta\eta = 0.1$ and $\Delta\varphi = 2\pi : 64 \approx 0.1$, except the third layer of the electromagnetic section which is twice as finely segmented.

The resolution of the calorimeter can be parametrised the following way:

$$\frac{\Delta E}{E} = \sqrt{C^2 + \left(\frac{S}{\sqrt{E/\mathrm{GeV}}}\right)^2 + \left(\frac{N}{E/\mathrm{GeV}}\right)^2}. \tag{2.4}$$

The single parts in this equation have different reasons:

- C: This systematic error arises from uncertanties in the calibration of the calorimeter. It dominates for electrons and hadron jets with a high energy.
- S: The resuting error is due to statistcal fluctuations in the number of particles in the shower. Since this number of particles is proportional to the energy of the shower, this error is dominant for low energy jets.
- N: This contribution does not depend on the energy. It is caused by noise in the calorimeter.

The values for electron as well as hadron jet resolution depent on η. Here the average values are given for a comparison, the exact values can be found in [14]:

	C	S	N
electons	≈ 0.1	≈ 0.3	≈ 0.0
hadron jets	≈ 0.1	≈ 1	≈ 5

Inter Cryostat Detector

The Inter Cryostat Detector (ICD) helps to measure jet energies as well as missing transverse energies in the otherwise un-instrumented area between the Central Calorimeter and the Endcap Calorimeter. Each of the two Inter Cryostat Detectors is made of 384 scintillator tiles which have the same size as the calorimeter towers ($\Delta\eta = 0.1$ and $\Delta\phi = 0.1$) and cover the same η and φ directions. The light signals of the scintillators are picked up by wavelength shifting fibres connected to clear fibre ribbon cables leading to photomultiplier tubes outside the strong magnetic field.

2.2.3 The Muon System

Because it is not used in this analysis just a very brief overview over the Muon System is given in this section. It is split into a Wide Angle MUon Spectrometer (WAMUS) for the central pseudorapidity region up to $\eta \leq 1$ and the Forward Angle MUon Spectrometer (FAMUS) for higher pseudorapidities up to $\eta \leq 2$. The muon system consists of three layers of drift tubes in the central and in the forward pseudorapidity region and two and three layers of scintillators, respectively. The first layers are inside a toroid iron magnet with 1.8 T allowing to measure the momentum of the muons.

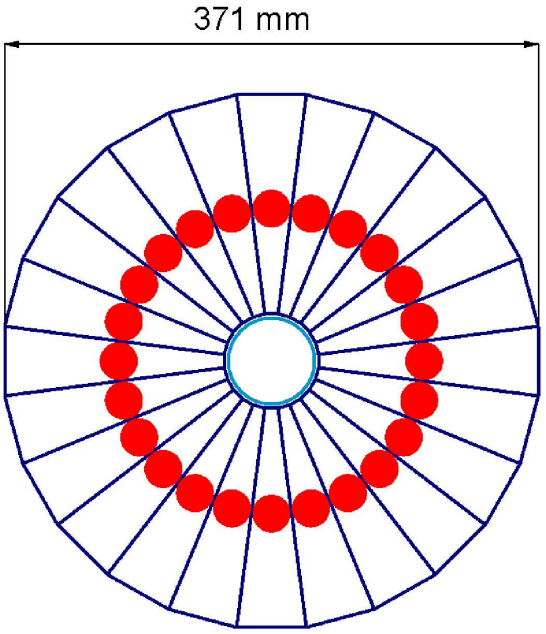

Figure 2.10: *Geometry of one of the luminosity monitors, the filled red dots are the photomultipliers, the beam pipe runs down the centre.*

2.2.4 Trigger & Luminosity

Luminosity measurement

The luminosity is measured with the help of two luminosity monitors (see Fig. 2.10) at a distance of ≈ 1.4 m in z from the centre of the detector. They are mounted on the face of the end cryostats (see Fig. 2.3 in pink). The hodoscopes of scintillation pixels cover a range of $2.6 < |\eta| < 4.5$. They measure the rate of hard, single diffractive and double diffractive processes. With the knowledge of the total cross section σ for these processes and the acceptance and efficiency of the hodoscopes the luminosity can be determined. The resulting systematic error on the measurement is 6.5%.

The luminosity is measured and stored in luminosity blocks (LBNs) which cover the time of 1 min.

Trigger

Beam crossings take place with a rate of 1.7 MHz. Since this would lead to a data rate of 500 GB/s a selection and reduction of the data is necessary straight away. This is done by triggers. DØ uses a 3 level trigger system to downscale the rate of events which can be written to tape with 50 Hz at maximum. Before the data is read out, the so called Level-0 requirement has to be satisfied, i.e. that hits in the two luminosity monitors coincide. (This is not counted as proper trigger).

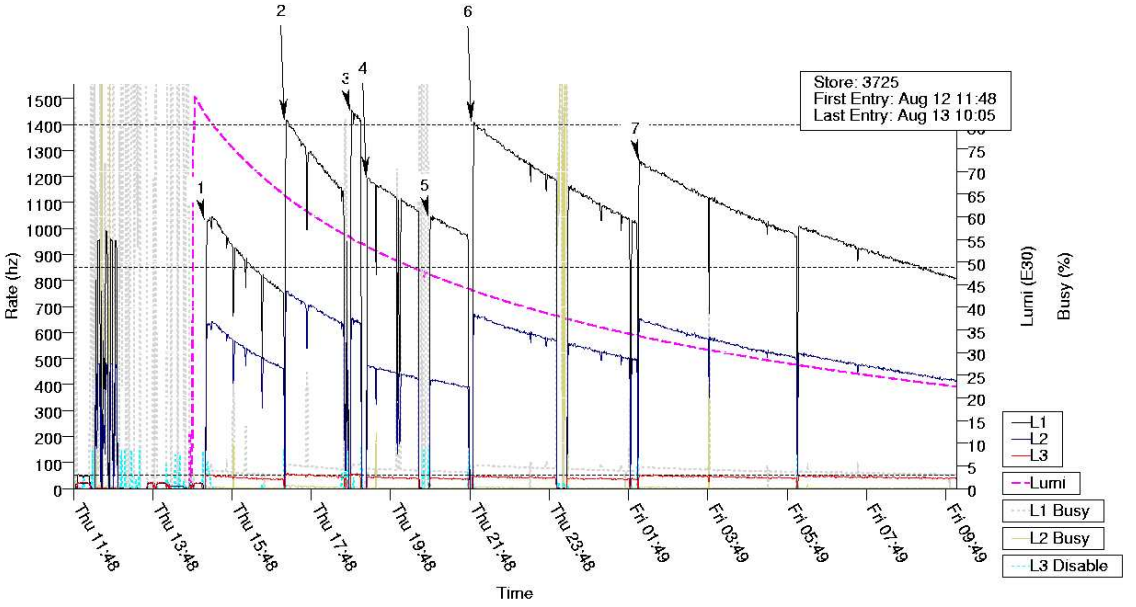

	Run	Duration	inL	Live	scl/hr	pause	<Tape Rate>	Prescale_File
1	196234	1.99 h	84.2	96%	4.0	0.01 h	38.4 hz	80-90E30
2	196235	1.58 h	65.4	93%	8.2	0.03 h	44.5 hz	60-70E30
3	196238	0.27 h	56.0	92%	0.0	0.02 h	45.9 hz	35-40E30
4	196239	1.43 h	54.0	91%	9.8	0.14 h	33.8 hz	35-40E30
5	196241	0.98 h	47.8	95%	0.0	0.01 h	34.6 hz	30-35E30
6	196242	4.19 h	44.2	94%	3.6	0.26 h	34.8 hz	40-45E30
7	196243	3.99 h	33.9	96%	0.5	0.03 h	41.7 hz	30-35E30

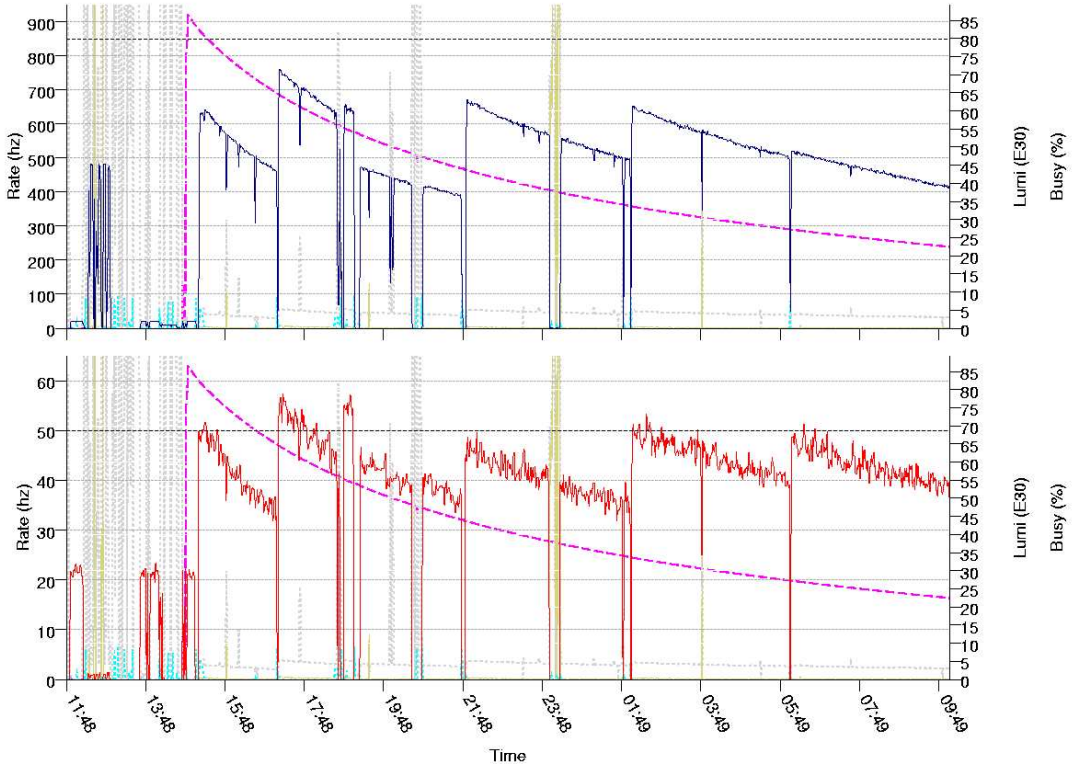

Figure 2.11: *The instantaneous luminosity measured over the time of one store as well as the different trigger rates. The level-1 rate at the top, level-2 in the middle and level-3 at the bottom.*

The Level-1 trigger is a hardware trigger reducing the event rate to 1.4 kHz. Only four detector components are used on Level-1, the Central Fibre Tracker (CFT) together with the Preshower Detectors, the muon system and the calorimeter. The relevant triggers for this analysis are jet triggers which use calorimeter information only. On Level-1 this information is the energy deposited in towers of the size $\Delta\eta = 0.2$ and $\Delta\varphi = 0.2$. The requirement CJT(3,5), for example, is satisfied if three calorimeter towers exceed 5 GeV each. If any of the Level-1 requirements is satisfied, the complete detector is read out and the event is passed on to the Level-2 trigger.

The Level-2 trigger is a mixed hardware and software trigger. The calorimeter towers are clustered into five by five groups of the Level-1 towers around the towers with the highest p_T. If the energy of this cluster is above a certain threshold, the event is accepted. Not all jet triggers have a Level-2 requirement, i. e. they are passed on to Level-3 when they satisfy the corresponding Level-1 requirement.

Level-3 is a pure software trigger partially reconstructing the event. For jets a simple cone algorithm is used assuming the vertex to be at $z = 0$ (For a more detailed description on jet algorithms see Chapter 3). The trigger is satisfied if the transverse energy of the jet is above a certain threshold.

In addition to the physics requirements prescales are used after the Level-1 trigger. They reduce the rate of events which are of interest but occur so often that not all of them are needed to obtain a high statistics sample. The prescales for rare events containing multiple leptons are 1, the prescales for most of the jet triggers used in this analysis are larger than one due to the high cross section for jet production in proton antiproton collisions. The prescales do not remain the same over time. As one can see in Fig. 2.11 the luminosity (pink) decreases during a store. With fixed prescales the rate of used events would decrease in the same way. To be able to keep as many events as possible the store is divided into Runs $(1 - 4\,\mathrm{h})$ where each run has different prescales depending on the instantaneous luminosity. This leads to a relatively constant rate of events passing the different triggers requirements. This is shown in Fig. 2.11.

2.2.5 Data Aquisition

Because the triggers need some time to decide on the usage of the event, the event information is first stored in a plipline, only if the corresponding trigger has fired, the information is read out. If all trigger levels have decided positive to keep an event, the raw data information is written to tape and then reconstructed with the latest reconstruction software (See also Chapter 4). The raw data as well as the reconstructed files are stored in a data handling system called SAM (Sequential Access via Metadata, [15]).

To ensure a good quality of data, the detector components are monitored at all times. If one of the compontents had problems during a run, the quality of this run is marked as bad. This information of the run quality is stored in a database.

Chapter 3

Jets and Jet Algorithms

In this chapter a description of jets is given and explanations are given as to what is understood by parton, particle or detector jet in this analysis. Then different algorithms for jet finding, in particular the cone algorithm most often used in DØ and as a comparison the k_T algorithm are explained.

As shown in Fig. 3.1, in proton and antiproton collisions quarks and gluons might be produced in QCD processes. These particles can radiate further gluons mainly close to their own direction. Then hadronisation takes place, leaving a bunch of particles all going to roughly the same direction. These particles are colourless mesons and baryons (e.g. π, K, p, ...) which then interact with the detector leaving their energy in the calorimeter. Jets can be defined on parton, particle and detector level, where they are a collection of partons, particles and calorimeter towers, respectively. Ideally, these jets would have the same energy and direction on all three levels, making it possible to reconstruct the original partons from the measurement of the energy deposited in calorimeter towers. In order to decide which particles or energy towers belong to which jet, an algorithm has to be defined which can be applied to partons, particles and towers. Inside such a "jet algorithm" a so-called "recombination scheme" is needed, defining the rule how to add momentum and energy of the particles.

3.1 The DØ Cone Algorithm

Cone algorithms form jets by including all partons, particles or energy depositions in the calorimeter (all three are later called objects) into the jet which are within a certain radius R to each other in the $(\eta \times \varphi)$ space. A starting point (seed) is needed around which the cone can be built. Afterwards the energy weighted centroid is calculated from objects within the cone around the seed. This centroid is then used as a new starting point and the calculation is repeated until a solution is found in which the axis of the energy weighted centroid is the same as the geometrical axis of the cone. Often towers above a certain

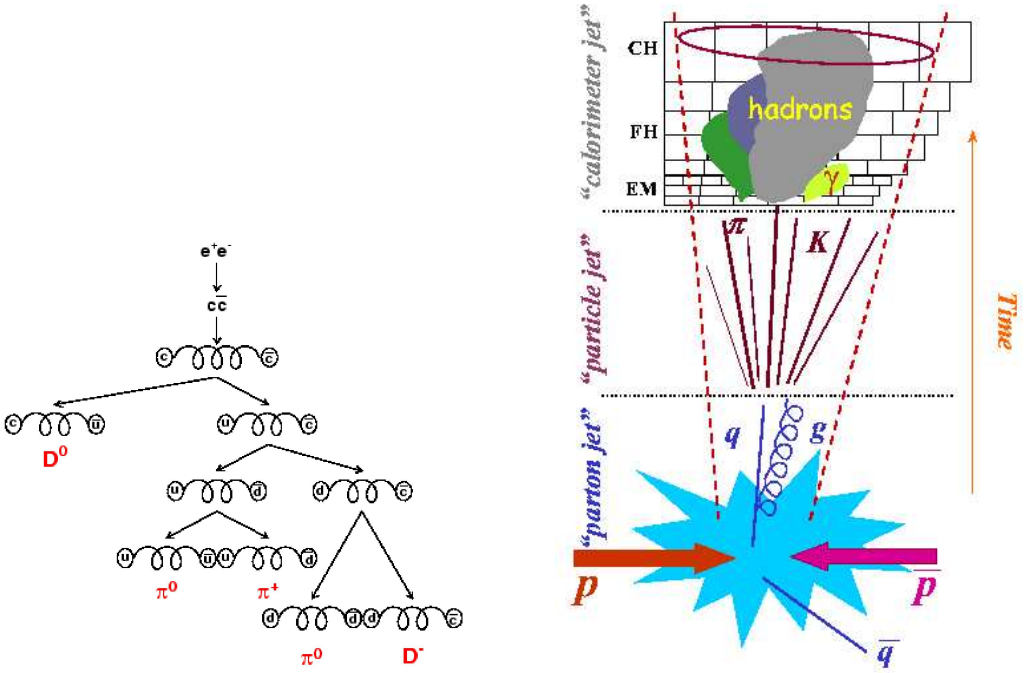

a) b)

Figure 3.1: *In a) the fragmentation process [17] and in b) the evolution of jets from parton level to detector level [18].*

energy threshold are used as seeds for reconstruction on detector level.

A few problems can occur with the cone jet algorithm. A brief overview is given here:

1. *Infrared safety:* This means that the identified jets do not depend on soft radiation. Soft radiation is radiation of low energy gluons at small or large angles relative to the direction of the original particle. But as shown in Fig. 3.2 this can occur easily if two objects are separated by less than $2R$ and more than R. In the absence of soft radiation they will build their own two jets. If there is soft radiation producing an additional seed, the result might be only one jet.

2. *Collinear safety:* This means that the reconstructed jets should not depend on collinear radiation i.e. radiation emitted in nearly the same direction as the parton/particle by which it is emitted. In Fig. 3.3a) one can see on the left that a jet might not be found because its energy is split into different cells which do not exceed the threshold for seeds, whereas on the right the energy is deposited in one cell and is thus big enough to build a seed for jet reconstruction. This is only a problem for low energy jets. If the transverse energy of the jet exceeds 20 GeV, this problem can be neglected if the seed threshold is 1 GeV. In Fig. 3.3b) the sensitivity to ordering by transverse momentum is demonstrated. The two outermost particles are not further apart than $2R$ but more than R. If the particle in the middle is the one with the highest transverse energy only one cone will be found. If the middle one splits into

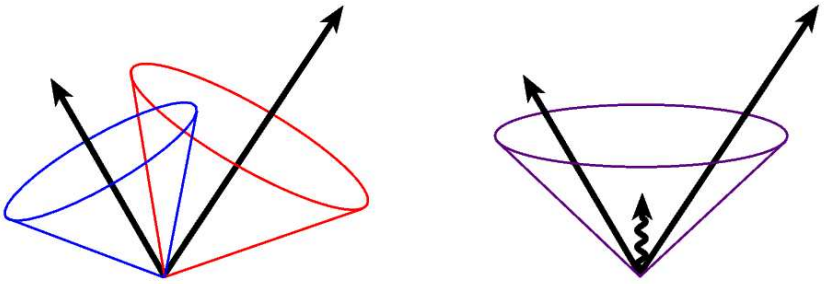

Figure 3.2: *Infrared sensitivity is one of the problems with cone jets if seeds are used without midpoints. Here jet clustering begins around seed particles, which gives two jets in the absence of soft radiation and one in the presence of soft radiation [16].*

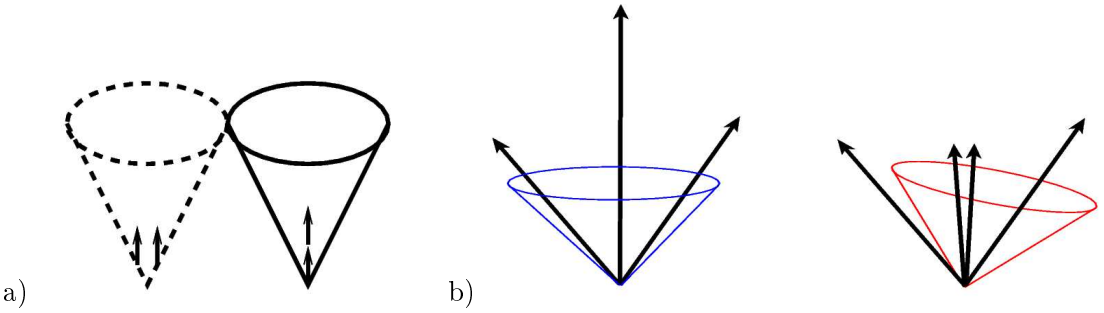

Figure 3.3: *Another problem with cone jets is collinear sensitivity. In a) a common problem with seeds is shown. On the left the energy deposition is spread over several cells producing no seed, on the on the right a seed is found producing a jet. b) is an example for sensitivity to E_T. [16].*

two nearly collinear particles (on the right), each having less transverse energy than the outer particles, two jets will be reconstructed.

3. *Splitting and Merging:* It might happen that the cones of two jets overlap. In this case an algorithm is needed to split or merge these two jets and to make sure that no object is counted twice.

In order to avoid inconsistencies, one should find an algorithm without these problems.

3.1.1 The Improved Legacy Cone Algorithm

DØ uses the so-called Improved Legacy Cone Algorithm (ILCA) for the offline data reconstruction [16]. Each object is assigned a massless four vector. The detector objects correspond to calorimeter towers of size of 0.1×0.1 in $(\eta \times \varphi)$ space. The position of the primary vertex of the hard scatter determined from the tracking system and the energy deposition in the towers is used to assign the four vector to the detector objects. The energy of these objects is simply the energy deposited in the calorimeter tower and the direction of the momentum pointing from the primary vertex to the centre of the tower.

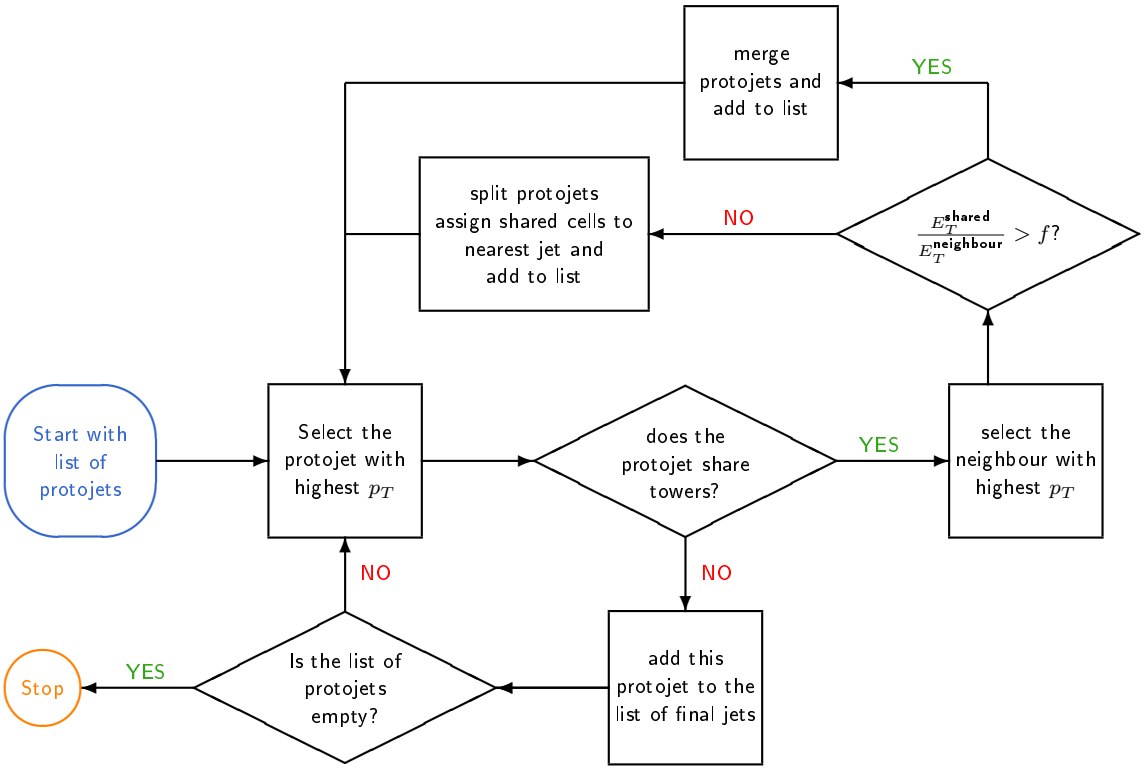

Figure 3.4: *The splitting and merging algorithm.*

An object is used as a seed if the transverse energy is greater than a threshold energy. Around these seeds all objects k within a cone C of radius R are determined.

$$k \in C \iff \Delta\mathcal{R}(k) \leq R \tag{3.1}$$

$$\text{with} \quad \Delta\mathcal{R}(k) = \sqrt{[\eta(k) - \eta(\text{cone})]^2 + [\varphi(k) - \varphi(\text{cone})]^2} \,. \tag{3.2}$$

The transverse momentum $\tilde{p}_T(\text{cone})$ of this "pre-protojet" is then calculated, using for recombination the *E-Scheme* also called *4-vector recombination*:

$$\begin{aligned} \tilde{p}(\text{cone}) &= \left(\tilde{E}(\text{cone}), \tilde{p}_x(\text{cone}), \tilde{p}_y(\text{cone}), \tilde{p}_z(\text{cone})\right) \\ &= \sum_{k \in C} \left(E(k), p_x(k), p_y(k), p_z(k)\right) \,. \end{aligned} \tag{3.3}$$

If the direction in $(\eta \times \varphi)$ space of $\tilde{p}(\text{cone})$ is sufficiently close to the direction of $p(\text{cone})$ (the momentum of the seed), the cone is called stable and this "pre-protojet" is added to the list of "protojets". If not, the direction of $\tilde{p}(\text{cone})$ is used as a new seed and the process is repeated until a stable solution is found.

Now the "midpoints" between the protojets are used as seeds. These midpoints are the sum of the momenta of each group of two, three ... protojets not further apart than $2R$. This makes the algorithm independent of most infrared and collinear radiation effects.

Since the resulting protojets might overlap, an algorithm is needed which decides whether these jets have to be split or merged. In Fig.3.4 the algorithm used for splitting or merging by DØ is explained. First the protojets are sorted by descending transverse energy. If the protojet with highest transverse energy does not share any object with another protojet it is added to the list of final jets. If it does share energy with any neighbours, the one with the highest transverse energy is considered first. If the transverse energy of shared objects is greater than a fraction f of the total transverse energy of the neighbour, the two protojets are merged. Otherwise the jets are split by assigning the shared objects to the nearest protojet. In both cases the centre of the protojet has to be recalculated and the new protojet is added to the list of protojets again. This procedure is repeated until no protojets are left. Only jets above a certain threshold of transverse energy are kept.

The following parameters for the Improved Legacy Cone Algorithm are used in this analysis:

seed threshold:	$E_T(\text{seed}) > 1$ GeV
split merge fraction:	$f = 0.5$
radius of cone:	$R = 0.7$
jet threshold:	$E_T(\text{jet}) > 8$ GeV

Some other analyses, e.g. in top physics use $R = 0.5$ instead of $R = 0.7$.

3.1.2 The Simple Cone Algorithm

This algorithm is used for the Level 3 trigger. It is similar to the Improved Legacy Cone Algorithm but it neither uses midpoints, nor does it split or merge protojets as it has to be faster.

3.2 The k_T Algorithm

Another algorithm often used is the k_T algorithm [16]. This algorithm does not fix the size of the jet explicitly like cone algorithms do. As illustrated in Fig.3.5 this algorithm starts with a list of objects. Now d_i and d_{ij} are calculated as follows where i and j are objects in the list with $i \neq j$:

$$d_i = p_{T,i}^2 \,, \tag{3.4}$$

$$\begin{aligned} d_{ij} &= \min(p_{T,i}^2, p_{T,j}^2) \cdot \frac{\Delta\mathcal{R}_{ij}^2}{D^2} \\ &= \min(p_{T,i}^2, p_{T,j}^2) \cdot \frac{(\eta_i - \eta_j)^2 + (\varphi_i - \varphi_j)^2}{D^2} \,. \end{aligned} \tag{3.5}$$

The parameter D of this algorithm is usually chosen to be close to one, in DØ the possible options are $D = 0.7$ or $D = 1.0$ which results in jets similar to those produced by the cone

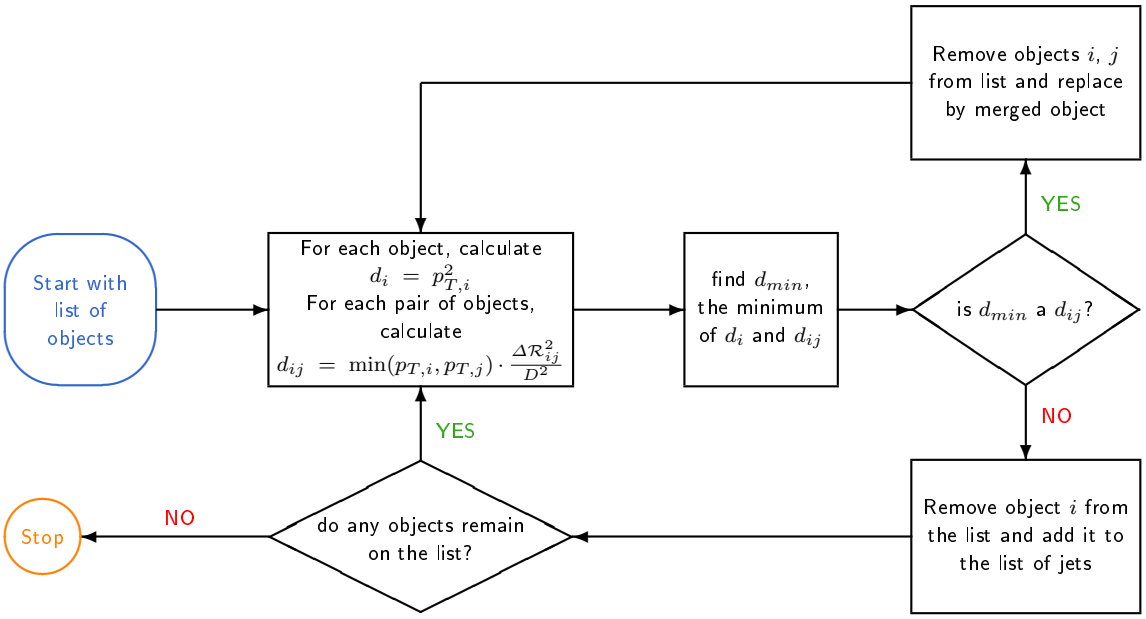

Figure 3.5: *The k_T algorithm.*

with $R = 0.5$ and $R = 0.7$, respectively. If the minimum of all d_i and d_{ij} is of type d_{ij} then the objects i and j are merged by adding their energy and momentum to a new object which is then added to the list of objects again. If the minimum is of type d_i the object i is added to the list of jets. This has to be repeated until no objects remain on the list. The jets found with this algorithm are all separated by $\Delta\mathcal{R} > D$. Because all d_{ij} have to be calculated and compared, this algorithm is very time intensive with $t \propto n_{objects}^3$. Thus running over $\sim$ 45000 cells of the DØ calorimeter would be to time-consuming, which makes it necessary to precluster these cells. This is done by adding up the energy and momentum of cells close to each other in $(\eta \times \varphi)$ space. It is similar to the cone algorithm just with a smaller cone radius. The resulting preclusters are the objects used for the k_T algorithm.

Chapter 4

Monte Carlo & Data Selection

In this chapter the generation of Monte Carlo events is described briefly, followed by an explanation of the reconstruction and selection criteria in this analysis. The cuts which aim to minimise potential detector problems are introduced. Then the selection of events by triggers is studied, driven by the need to make the data sample sufficiently small to be further examined. At the end of this chapter further cuts are explained which ensure that events and jets are well-measured.

4.1 Monte Carlo Generators

In order to be able to compare data with theory, Monte Carlo generators are used. These simulate the interaction of the two incoming particles. It has to be taken into account that it is ambiguous which particle in the proton interacts with which particle in the antiproton. This is randomly chosen for every Monte Carlo event, based on the parton density functions of the proton. The final state particles of the interaction are then generated using theoretical calculations for the cross sections of different processes.

4.1.1 Pythia

Pythia is a Monte Carlo event generator for different colliders, e.g. electron positron collisions as well as proton (anti)proton collisions, it is assumed that fragmentation is the same for both processes. It can generate basically all Standard Model processes including higgs production and beyond. Leading order Matrix elements for $2 \to 2$ and $2 \to 1 \to 2$ processes are used. for generation of more jets initial and final state radiation in the form of gluons and parton plus parton shower in leading log approximationis implemented. This leads to inconsistencies between data and Monte Carlo at high jet multiplicities, because the simulated gluons are too close to the parton from which they are radiated, resulting in only one jet instead of two. For the hadronisation the Lund fragmentation model is used. A more detailed description of Pythia is given in [19].

For a comparison with the inclusive jet cross section a by DØ produced PYTHIA Monte Carlo with full detector simulation is used. See Fig. 4.1 for the chain of production and reconstruction of Monte Carlos. After the production of the events in the generator, their interaction with the detector and the resulting digital signals are simulated by the DØ software called d0gstar and d0sim. These software tools also simulate multiple interactions and smear the Vertex positon with $\sigma = 25\,\text{cm}$ around $z = 0$. Finally, the output is reconstructed with d0reco like normal data signals from the detector. For this analysis they were converted into ROOT trees [20] by the Top Analyze package [21], just like the data.

4.1.2 ALPGEN

ALPGEN [22] is an event generator for multi parton hard processes in hadronic decays in proton (anti)proton collisions. It is used to simulate final states with light as well as heavy quark jets and bosons. In contrast to PYTHIA, ALPGEN uses the exact matrix elements calculated in leading order for $2 \to n$ processes. Because it only generates events on parton level, Pythia is used for the hadronisation process. ALPGEN initially produces weighted events which have to be unweighted in a second step.

These ALPGEN Monte Carlo events are used for the Multijet analysis because PYTHIA, as a parton shower generator, does not describe events with higher jet multiplicities accurately. For this analysis events with $n = 2, 3, 4, 5$ and 6 partons in the final state of proton antiproton collisions were generated separately at a centre of mass energy of $\sqrt{s} = 1.96$ TeV. No final states with heavy quarks (top, bottom) were considered as their contribution is expected to be negligible, only light quarks like up, down, strange and charm, as well as gluons do occur. To minimise the computing time the following constraints were applied at generator level for all partons:

$p_T(\text{parton})$	$>$	20 GeV
$\lvert\eta(\text{parton})\rvert$	$<$	3.0

Since no ALPGEN Monte Carlo events have yet existed, these events were produced for this analysis. Further processing was done by mc_runjob which is a DØ framework package for Monte Carlo production [23]. It works as described above and in Fig. 4.1. As input the unweighted ALPGEN Monte Carlo files are used. The PYTHIA hadronisation is already included in the mc_runjob framework. Thumbnails (TMBs) are the final output of mc_runjob. They are then converted into ROOT trees e.g. by Top Analyze.

4.2 Reconstruction & Preselection

The experimental data for this analysis was taken between November 2003 and April 2004. This corresponds to the run numbers ranging from 185746 to 192159. The recorded luminosity is $\mathcal{L}_{int} = (112 \pm 7)\,\text{pb}^{-1}$. The 4-jet trigger used for the multijet analysis was

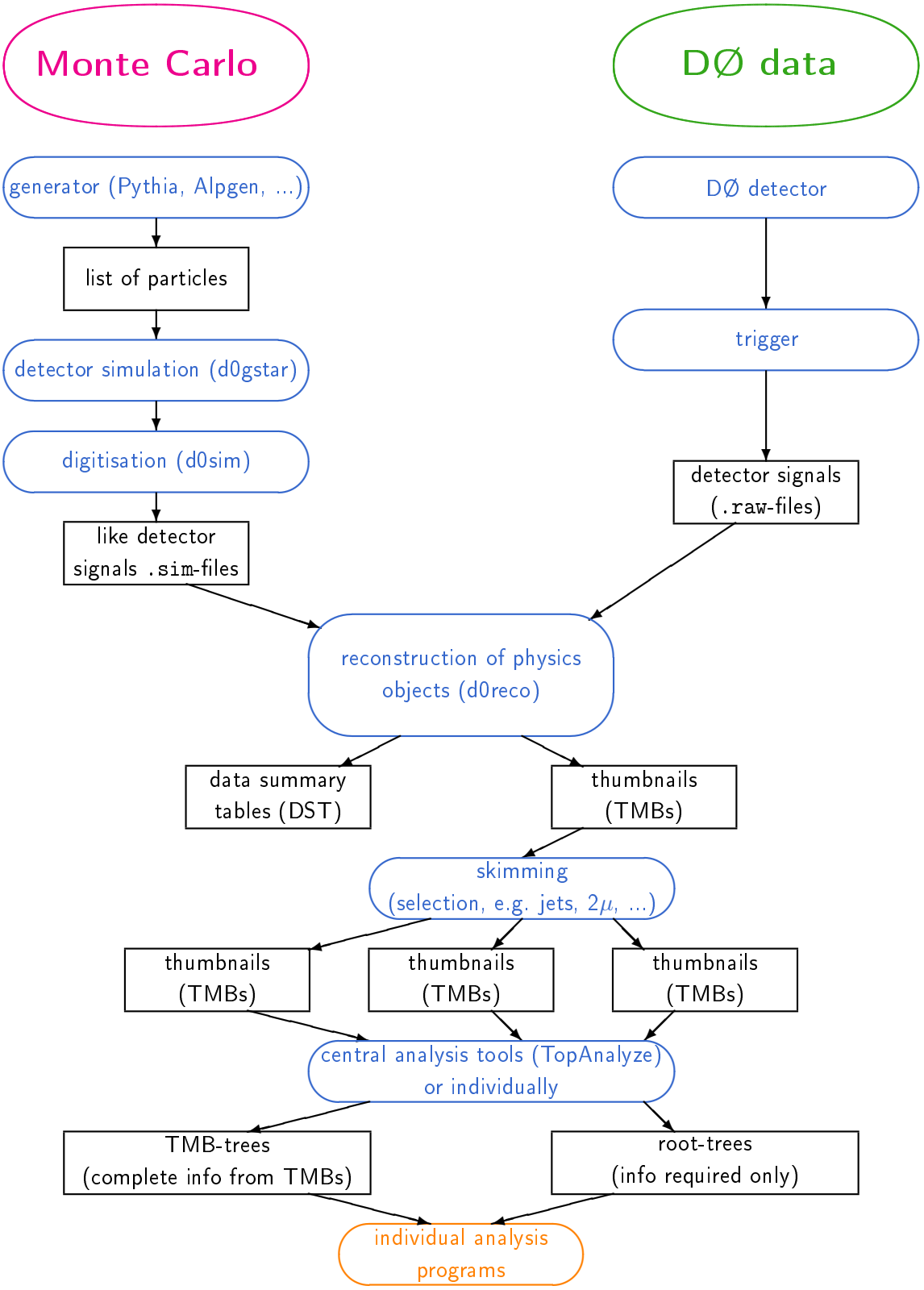

Figure 4.1: *The main steps in the data reconstruction and Monte Carlo production. From the reconstruction on, they are both treated equally. The difference between DST's and TMB's is that the full information of an event is kept in DST's whereas TMB's are a compressed format keeping only the information of interest for the physics analyses.*

only available for a short period before September 2003, resulting in a recorded luminosity of $\mathcal{L}_{int} = (1.2 \pm 0.1)$ pb^{-1} for the run range 160582-176852. Both samples are subsamples of the total recorded luminosity until September 2004 of $\mathcal{L}_{int} \approx 471$ pb^{-1}.

4.2.1 Data Reconstruction

The digital hardware signals of all triggered events were written to tape and then processed by the reconstruction software to identify physical objects (see Fig. 4.1). In particlar the jets are reconstructed with the Improved Legacy Cone Algorithm explained in Section 3.1.1. The reconstruction software exists in different versions, new ones being released every few weeks. All the data used in this analysis were reconstructed by the release p14.06.00. The reconstructed data were saved as thumbnails (TMBs) and stored in the DØ database SAM (Sequential data Access via Metadata [15]). Different skims were made by the Common Sample Group [24]. A skim is a specific selection of events. This selection usually requires specifically reconstructed physics objects or that specific triggers fired in an event. For the inclusive jet spectrum the QCD skim is used. It contains all events triggered by inclusive single jet triggers. For the multijet analysis the 3Jet skim containing all events with at least then 3 jets with a minimum transverse energy of 20 GeV, 15 GeV and 15 GeV, respectively, is used in addition.

4.2.2 Run & Luminosity Block Selection

Due to detector problems in different subsystems the run quality might be marked bad for this specific subsystem. The information on the run quality is stored in the Offline Run Quality Database [25]. Because the instrument to measure jets is the calorimeter, bad runs in this subsystem were not used.

Additionally, different kinds of noise might occur. Some of them are resulting in unphysical reconstructed high energy jets [26]. An example of such a noise event is given in Fig.4.2. Obviously these events should not be used for the analysis. Because these noise events do not occur in all events in a run, only the affected luminosity blocks are not used. Since luminosity blocks are smaller units than runs, the fraction lost due to these problems is smaller than in the case where bad runs are sorted out. The list of bad luminosity blocks was taken from the JET/MET Run & Lumi-Block Selection web page [27].

4.2.3 Trigger

Other event selection criteria are the triggers. Different inclusive single jet triggers are used, all requiring at least one jet reconstructed on Level-3 with the simple cone algorithm (see section 3.1.2) having a transverse energy above a certain threshold. This threshold varies between 8 GeV and 95 GeV with the corresponding triggers having different prescales. Another single jet trigger with a threshold of 125 GeV is available but redundant, as the 95 GeV trigger is already not prescaled and thus should detect all high energy jets. Apart from these six single jet triggers an additional four-jet-trigger is used for the multijet

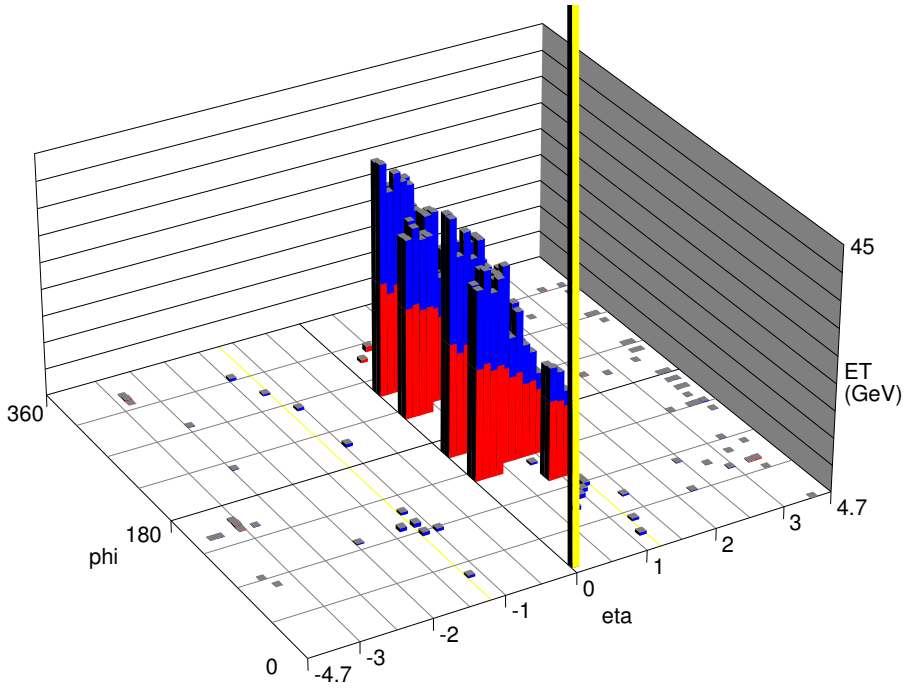

Figure 4.2: *Noise in the calorimeter: two jets were reconstructed with a transverse momentum of* 1134 GeV *and* 1125 GeV. *In red and blue the recorded depositions in the electromagnetic and hadronic calorimeter, the yellow spike at* $\varphi = 0$ *is the missing transverse energy determined by summing up all calorimeter entries.*

analysis. The requirements on the three trigger levels for the different triggers are listed in Tab. 4.1 (one should remember that the Level-1 trigger towers have a size of 0.2×0.2 in $(\Delta\eta, \times\Delta\varphi)$ space). All triggers are instrumented up to $|\eta| = 3.2$.

The effective trigger luminosity is determined by the tool "lm_access" which takes into account the prescales of the different triggers. The bad runs were not used, so that no corrections concerning these selections have to be made. In table 4.2 the integrated effective trigger luminosities are listed as well as the prescales for the different triggers. The luminosity has an overall systematic uncertainty of 6.5%.

Trigger Efficiency

A first attempt was made to measure the trigger efficiency from minimum bias events. But due to the fact that only one in about 10^7 events would have a jet with transverse momentum above 30 GeV in $|\eta| < 2.4$ statistics would be too low, even if all minimum bias events were used. Thus another way to determine the trigger efficiency had to be found.

This method assumes that the trigger reaches 100% efficiency above a certain value of the transverse momentum of the leading jet. Due to the different jet algorithms used on trigger Level-3 and in the reconstruction, the threshold does not have to be the same as on trigger Level-3. But it is taken for granted that the one with the lower threshold reaches 100% efficiency before the one with the higher threshold on trigger Level-3. To find the region of 100% efficiency of each trigger, the raw differential cross sections (Fig. 4.3) of one trigger

are divided by the raw differential cross sections of the lower neighbour trigger where the raw differential cross section is defined as follows:

$$\frac{d\sigma_{\text{raw}}}{dp_T} = \frac{N_{\text{trigger}}(p_T)}{\mathcal{L}_{\text{trigger}} \cdot \Delta p_T} . \tag{4.1}$$

So the trigger efficiency e.g. for the trigger JT_65TT is:

$$\varepsilon_{\texttt{JT\_65TT}} = \frac{N_{\texttt{JT\_65TT}} \cdot \mathcal{L}_{\texttt{JT\_45TT}}}{N_{\texttt{JT\_45TT}} \cdot \mathcal{L}_{\texttt{JT\_65TT}}} . \tag{4.2}$$

In Fig. 4.4 the trigger efficiencies are plotted for each trigger except for the trigger JT_8TT, because it is the one with the lowest threshold. As one can see the triggers are fully efficient at a transverse momentum of approximately twice the trigger threshold on Level-3. Thus it is assumed that the trigger JT_8TT is fully efficient for jets above 30 GeV.

For the inclusive cross section measurement the region in p_T is taken in which the trigger is fully efficient and the statistics are high enough, except for the trigger JT_95TT. This trigger has a lower limit due to the trigger threshold but no upper limit to cover the complete p_T spectrum. In Tab. 4.2 the minimum and maximum p_T values for each trigger are given.

For the multijet cross section measurement the trigger JT_15TT is used for jet multiplicities up to three. Here it is only required that the transverse momentum of the leading jet is above the threshold of 50 GeV. For jet multiplicities above three the trigger 4JT10 is used

trigger name	trigger requirement		
	level-1	level-2	level-3
JT_8TT	1 calorimeter tower with $E_T > 5$ GeV	—	one simple cone jet with $E_T > 8$ GeV
JT_15TT	2 calorimeter towers with $E_T > 3$ GeV	—	one simple cone jet with $E_T > 15$ GeV
JT_25TT_NG	2 calorimeter towers with $E_T > 5$ GeV	—	one simple cone jet with $E_T > 25$ GeV
JT_45TT	2 calorimeter towers with $E_T > 5$ GeV	—	one simple cone jet with $E_T > 45$ GeV
JT_65TT	3 calorimeter towers with $E_T > 5$ GeV	1 jet candidate with $E_T > 20$ GeV	one simple cone jet with $E_T > 65$ GeV
JT_95TT	4 calorimeter towers with $E_T > 5$ GeV	1 jet candidate with $E_T > 30$ GeV	one simple cone jet with $E_T > 95$ GeV
4JT10	4 calorimeter towers with $E_T > 5$ GeV	3 jet candidates with $E_T > 8$ GeV and transverse hadronic energy of all jets($E_T > 8$ GeV) greater than 90 GeV	4 simple cone jets with $E_T > 10$ GeV, 2 of these jets with $E_T > 20$ GeV

Table 4.1: *The trigger requirements for the triggers used in this analysis.*

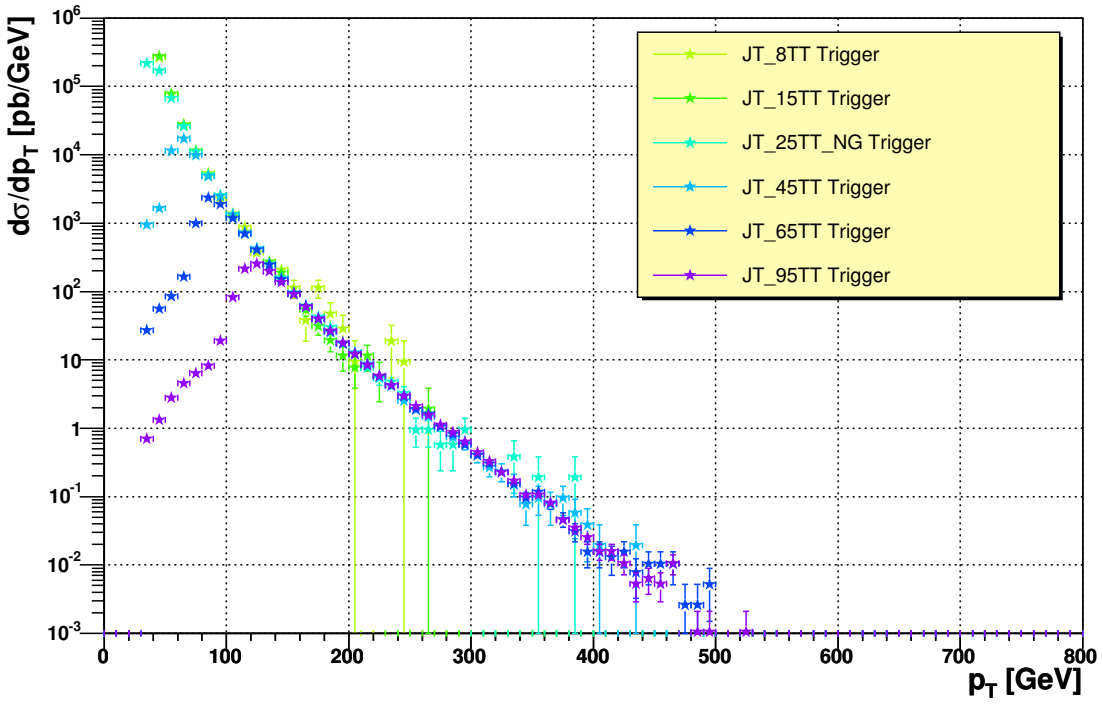

Figure 4.3: *The raw cross sections for all single jet triggers in* $|\eta| < 2.4$.

due to better statistics. It is assumed that it is fully efficient for a transverse momentum of the leading jet above 50 GeV and of the other jets above 30 GeV because the measured four-jet cross section is the same for both triggers, `JT_15TT` and `4JT10`.

4.3 Event Selection

As explained in Chapter 3, jet reconstruction uses the information of the primary vertex reconstruction. In order to ensure a good reconstruction, the measurement of the primary

trigger name	$\mathcal{L}_{trigger}$ [pb^{-1}]	prescale	number of events	minimum p_T [GeV]	maximum p_T [GeV]
`JT_8TT`	0.0106	≈ 8934	157202	30	50
`JT_15TT`	0.0518	≈ 1828	66502	50	90
`JT_25TT_NG`	0.523	≈ 181	56595	80	110
`JT_45TT`	5.18	≈ 18.3	162792	100	140
`JT_65TT`	38.6	≈ 2.45	261235	130	200
`JT_95TT`	94.7	1	56633	190	—
`4JT10`	1.19	1	91843	50, 30, 30, 30	—

Table 4.2: *Luminosities, prescales, number of events and transverse momentum range for the different triggers used in this analysis.*

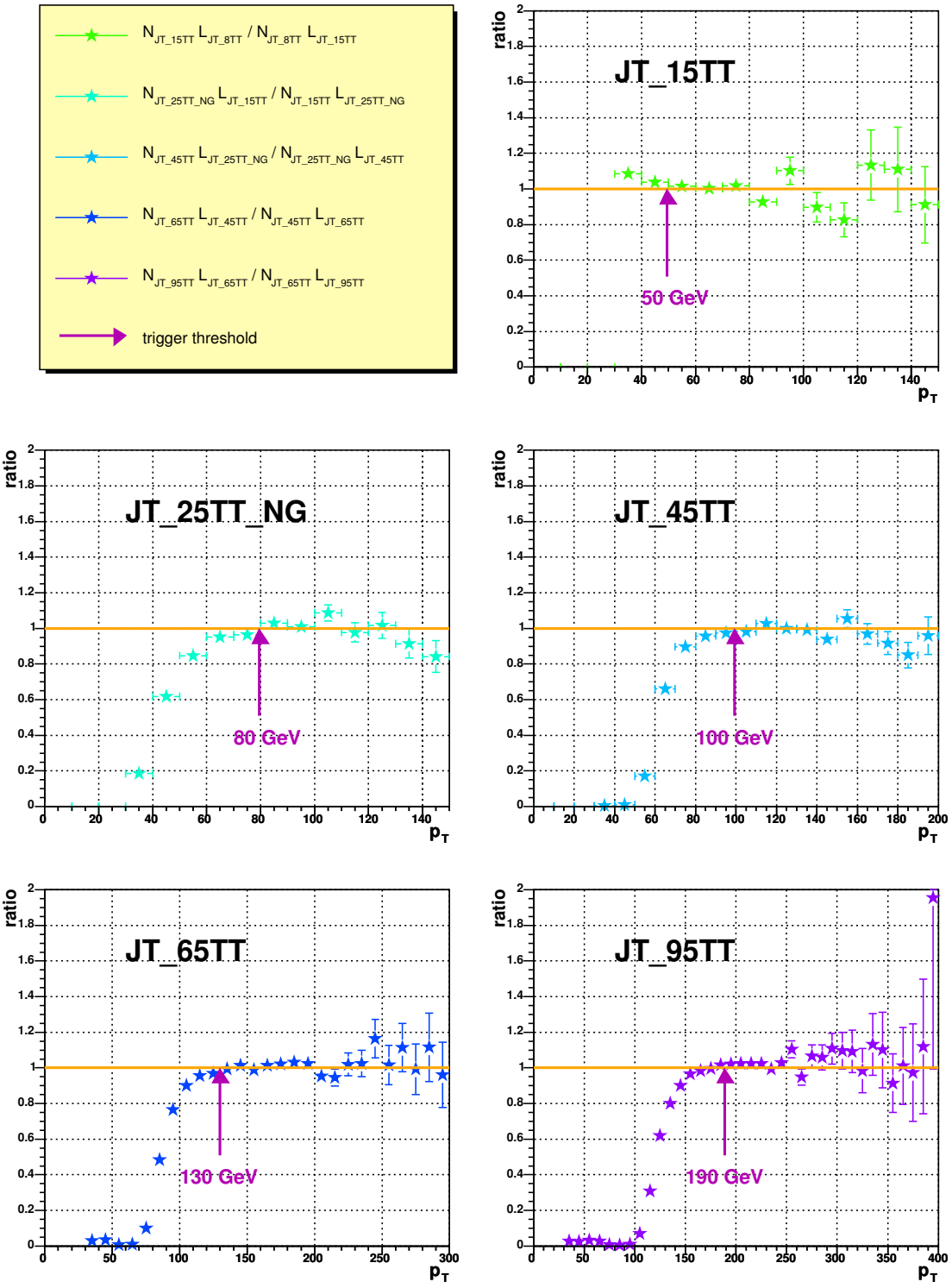

Figure 4.4: *Turn on curves of the single jet triggers.*

vertex has to be of reasonable quality. Therefore two cuts on the reconstructed primary vertex are applied.

- **Cut on the position of the reconstructed primary vertex:** $|z| < 50$ cm, $|z| \neq 0$
  The bunches in the tevatron collider have an expansion in the direction along the beam pipe z. The point of interaction called primary vertex does not have to be in the exact centre of the detector which would be at $z = 0$, called the nominal point of interaction, but is spread around this point in a Gaussian shape with a width of $\sigma_z = 25$ cm. Only events with a vertex position less than $2\sigma_z = 50$ cm away from the nominal point of interaction are used for this analysis. Tracks from vertices further away might not have been measured in the tracking system, resulting in a poorly measured primary vertex position, which would also affect jet kinematics. In events where no vertex could be reconstructed the position is taken to be $z = 0.0$ by the reconstruction software. These events are not used either.
- **Cut on the number of tracks to the primary vertex:** $N_{\text{tracks}} \geq 3$
  In a case where the vertex is reconstructed from less than three tracks the position is highly unreliable resulting in a huge error of the jet measurement. Hence these events are not used for the analysis.

These events are not unphysical events but rather badly measured. Therefore it is supposed that the efficiency of this cut is equal to the number of events with at least one jet passing all cuts divided by the number of events with at least one jet passing all cuts except the vertex cut. In Fig. 4.5 the number of all events passing the vertex cut compared to the ones without the vertex criteria applied are plotted versus the z position for the trigger `JT_25TT_NG`. The peak at $z = 0$ is due to events where no vertex could be reconstructed. The efficiency for the Monte Carlo events is higher because the detector simulation does not simulate the width of the vertex position correctly (see Fig. 4.6). In particular the peak at $z = 0$ is missing completely. This is probably due to the fact that no vertex could be reconstructed for interactions at large z. Since the width of the Monte Carlo distribution is much smaller, no events are at such large z. This results in different efficiencies for these cuts in data and Monte Carlo. The vertex efficiencies for different triggers and the PYTHIA Monte Carlo are given in Tab. 4.3.

4.4 Jet Identification

In some cases noise might have been reconstructed as a jet. To ensure that these "jets" do not contaminate the data sample, different quality cuts are applied to all jets. These cuts will be explained in the following. Uncorrected energy is the energy before jet energy scale corrections are applied as explained later in section 4.5.

trigger	`JT_8TT`	`JT_15TT`	`JT_25TT_NG`	`JT_45TT`	`JT_65TT`	`JT_95TT`	PYTHIA MC
ϵ_{vertex}	0.901	0.894	0.892	0.890	0.890	0.897	0.955

Table 4.3: *Efficiencies for the cuts on the vertex.*

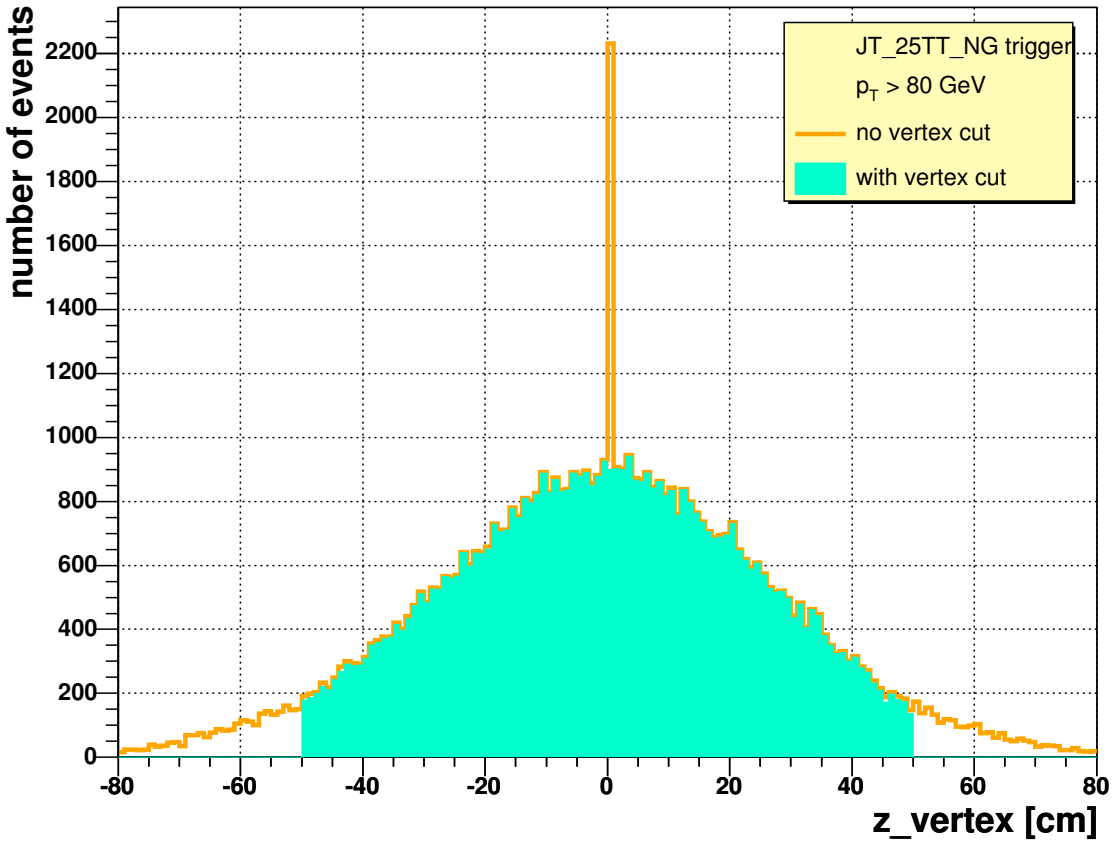

Figure 4.5: *The distribution of the reconstructed primary vertex position in z of events with at least one reconstructed jet with $p_T > 80$ GeV triggered with the trigger* `JT_25TT_NG`*. The orange line are all events, the filled area are events wich passed all vertex criteria.*

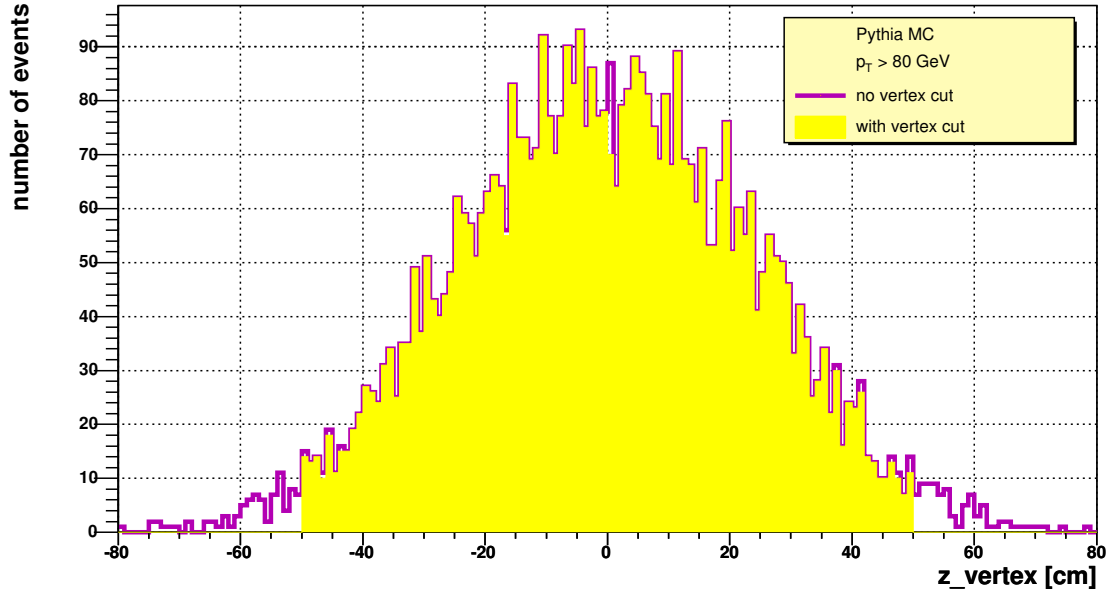

Figure 4.6: *The distribution of the reconstructed primary vertex position in z of events with at least one reconstructed jet with $p_T > 80$ GeV for* PYTHIA *Monte Carlo events. The pink line are all events, the filled area are events which passed all vertex criteria.*

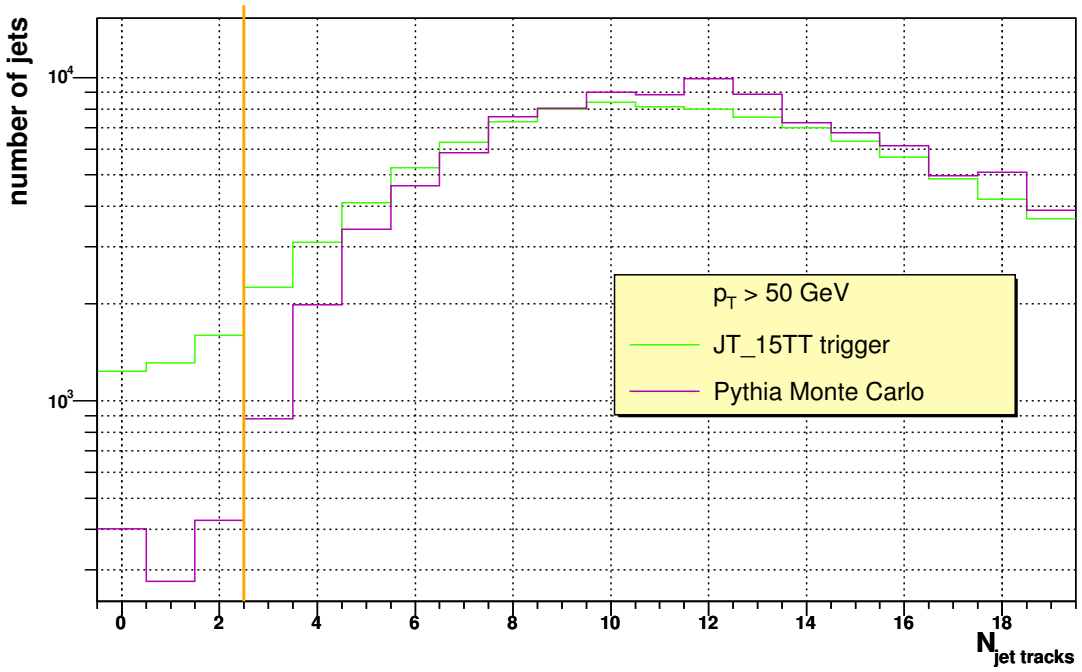

Figure 4.7: *The number of tracks found in a cone with $R = 0.5$ around the jet in data and Monte Carlo (normalised to the area below data).*

- **General kinematic and acceptance cuts:** $p_T > 30$ GeV and $|\eta| \geq 2.4$
  Only jets with a transverse momentum higher than 30 GeV are considered because below that threshold the error on the momentum is rising steeply mainly due to the error on the jet energy scale (see section 4.5). The cut on η is applied, as the triggers have not always been sensitive at high pseudorapidities.

- **Cut on the number of tracks pointing to the jet:** $N_{\text{jet tracks}} \geq 3$
  Since a jet contains a number of charged particles, one would expect tracks pointing in the direction of the jet. It is required that at least three tracks are found in a cone with $R = 1.0$ around the jet axis. In Fig. 4.7 the distribution of the number of tracks within this cone is shown for jets with a transverse momentum above 50 GeV and all jet cuts applied except this one. The number of tracks requirement removes approximately 2.5% of the jets in data events and 1% in Monte Carlo events. This supports the idea that a lage part of these jet like objects are no proper jets, since less occur in the Monte Carlo.

- **Cut on the electromagnetic fraction in the calorimeter:** $0.05 < EMF < 0.95$
  The electromagnetic fraction (EMF) is the fraction of the jet's uncorrected energy measured in the electromagnetic part of the detector. As shown in Fig. 4.8 it varies a lot. A jet might consist of many or few neutral pions which decay into photons depositing their energy in the electromagnetic part of the calorimeter. On the contrary, charged pions shower mainly in the hadronic part of the calorimeter. Thus only extreme values above 95% and below 5% are not allowed for jets because they are most probably caused by noise in the calorimeter cells. This removes 2% of the jets in the data events and 1.5% in the Monte Carlo events. High values of the electromagnetic

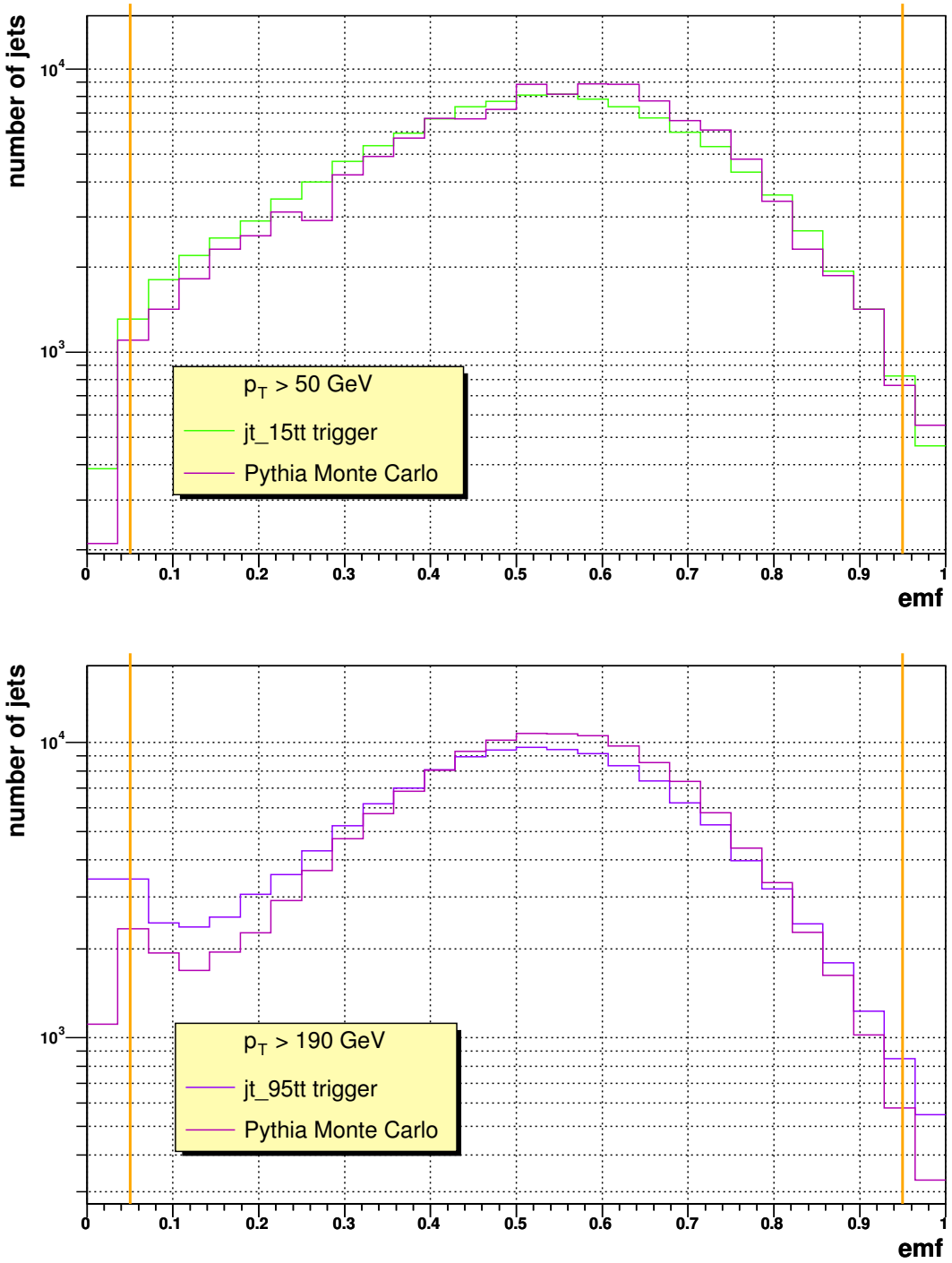

Figure 4.8: *The electromagnetic fraction of jets which satisfy all other jet cuts. At the top data from the trigger* JT_15TT *with a minimum transverse momentum of* 50 GeV *is compared with a* PYTHIA *Monte Carlo prediction. At the bottom data from the trigger* JT_95TT *with a minimum transverse momentum of* 190 GeV *is also compared to a* PYTHIA *Monte Carlo prediction (normalised to the area below data).*

fraction might also correspond to photons or electrons which were not identified as such, because their shower shape failed the cuts for electromagnetic objects. The fraction of jets with a low electromagnetic fraction increases with higher threshold for the transverse momentum. In Fig. 4.8 the electromagnetic fraction of jets with more than 50 GeV is compared with the one of jets with more than 190 GeV. While the electromagnetic fraction of the low p_T jets decends toward $emf = 0$, it rises again slightly for the high p_T jets. This behaviour is similar in data and in the Monte Carlo sample, although it is not as extreme in the Monte Carlo sample. A possible reason for this might be, that jets with a higer energy are longer so that more energy is deposited in the hadronic parts of the calorimeter leading to a lower electromagnetic fraction.

- **Cut on the coarse hadronic fraction in the calorimeter:** $CHF < 0.4$
  The coarse hadronic fraction (CHF) is the fraction of the jet's uncorrected energy, which is measured in the coarse hadronic part of the calorimeter. For the majority of jets this fraction is small (see Fig. 4.9) as big parts of the jet should have been absorbed in the electromagnetic and fine hadronic section of the calorimeter. The data has more events with a high coarse hadronic fraction than the Monte Carlo simulation, which underlines that jets with high values are very likely to originate from calorimeter noise and thus the Monte Carlo does not contain these "jets". Therefore it is required that the coarse hadronic fraction of the uncorrected energy is less than 40%. This cut removes approximately 3% of the jets in the data events and less than 1% in the Monte Carlo events.

- **Cut on the ratio of the cell with highest transverse energy to the second highest transverse energy cell:** $HotF < 10$
  The ratio between the largest uncorrected energy in a cell and the second largest uncorrected energy in a cell within a jet is called hot fraction ($HotF$). Usually the energy in a jet should be spread over many cells and no single cell should contain a major part of the energy. This is only likely to happen when there is noise in this cell of the calorimeter. Thus it is required that the hot fraction is below 10. As shown in Fig. 4.10, this is the case for most of the jets. Only 0.15% of the jets in data and 0.05% in Monte Carlo have a hot fraction of more than 10. The fact that less events in the Monte Carlo simulation show this behaviour is due to the fact that no noise is simulated in the Monte Carlo.

- **Cut on the number of towers with 90% of the jet transverse energy:** $n90 > 1$
  This variable, called $n90$ is the minimum number of towers containing 90% of the jet's energy. This should be more than one, otherwise it is very probable that the jet was caused by a noisy tower so the criterion on the $HotF$ does not work. But as shown in Fig. 4.11, after all other jet cuts are applied, no jets remain with less than two towers containing 90% of the jets energy. The reason this cut is kept is that it was used for the jet energy scale callibration.

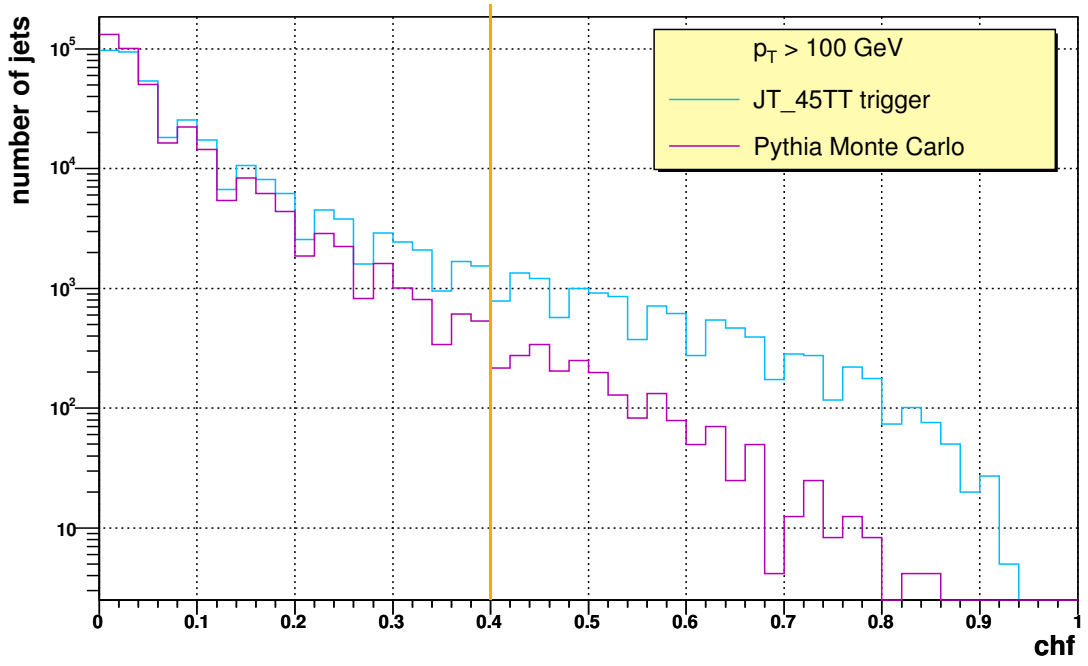

Figure 4.9: *The coarse hadronic fraction of jets which satisfy all other jet cuts. Data from the trigger* `JT_45TT` *with a minimum transverse momentum of* 100 GeV *is compared with a* PYTHIA *Monte Carlo prediction (normalised to the area below data). The shape is very similar for all transverse momentum thresholds.*

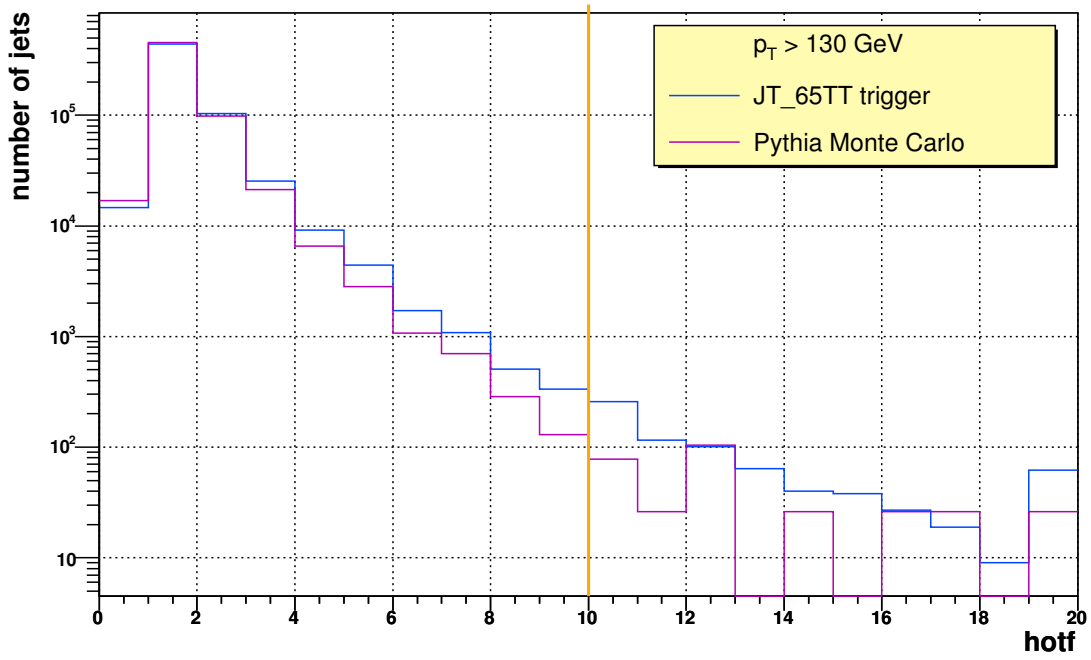

Figure 4.10: *The hot fraction of jets which satisfy all other jet cuts. Data from the trigger* `JT_65TT` *with a minimum transverse momentum of* 130 GeV *is compared with a* PYTHIA *Monte Carlo prediction (normalised to the area below data). The shape is very similar for all transverse momentum thresholds.*

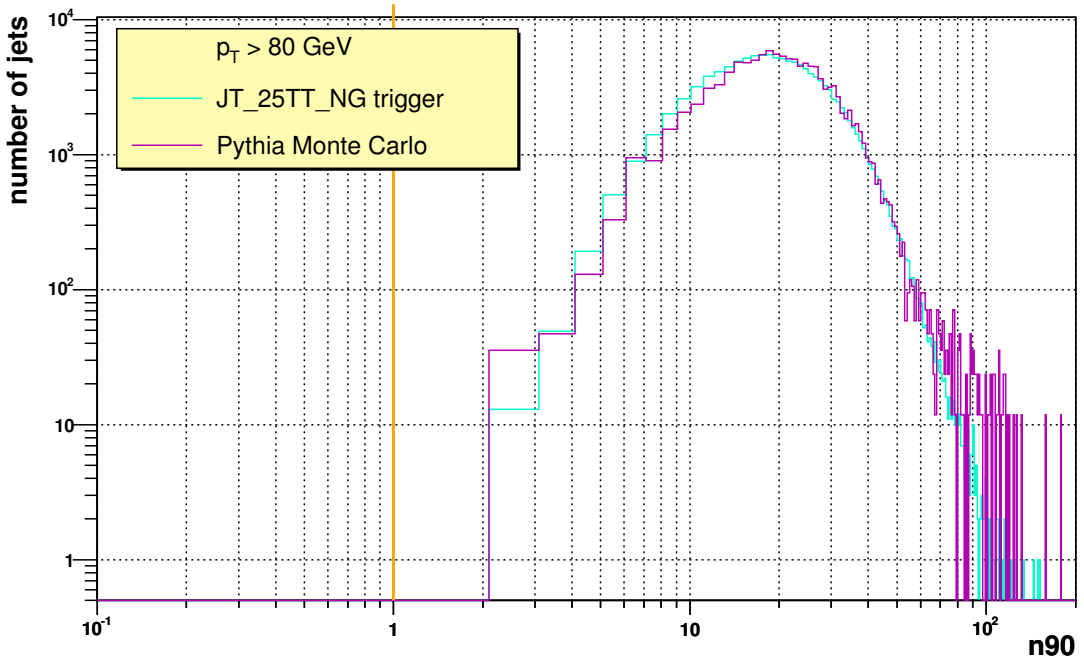

Figure 4.11: *The variable n90 of jets which satisfy all other jet cuts. Data from the trigger JT_25TT_TT with a minimum transverse momentum of* 80 GeV *is compared with a* PYTHIA *Monte Carlo prediction (normalised to the area below data). One can see that no further jets are removed by this cut. The shape is very similar for all transverse momentum thresholds.*

- **Cut on the energy seen by the Level-1 trigger compared to the reconstructed transverse energy:**

$$\frac{E(\text{level-1 trigger})}{p_T \cdot (1 - CHF)} > \begin{cases} 0.4 & : \text{ CC and EC region} \\ 0.2 & : \text{ ICD region} \end{cases}$$

Since the trigger readout does not produce much noise, this cut compares the energy seen by the Level-1-trigger to the reconstructed energy of the jet. Since the Level-1-trigger neither uses information of the coarse hadronic section of the calorimeter nor is this energy corrected by the jet energy scale (see section 4.5), it has to be compared to the transverse momentum without these components and before corrections. It is required that the fraction of energy seen by Level-1 should be more than 40% of the uncorrected transverse momentum of the jet. Since in the Inter Cryostat region not all information is used on Level-1, only 20% are required at minimum (see Fig. 4.12). This cut removes approximately 5% of the data. It is only applied on data and not on Monte Carlo as triggers are not simulated in Monte Carlo .

4.5 Jet Energy Scale

Different effects lead to the fact that the jet energy, simply being the energy deposited in the calorimeter within the jet cone, is not exactly the energy the jet had on particle level.

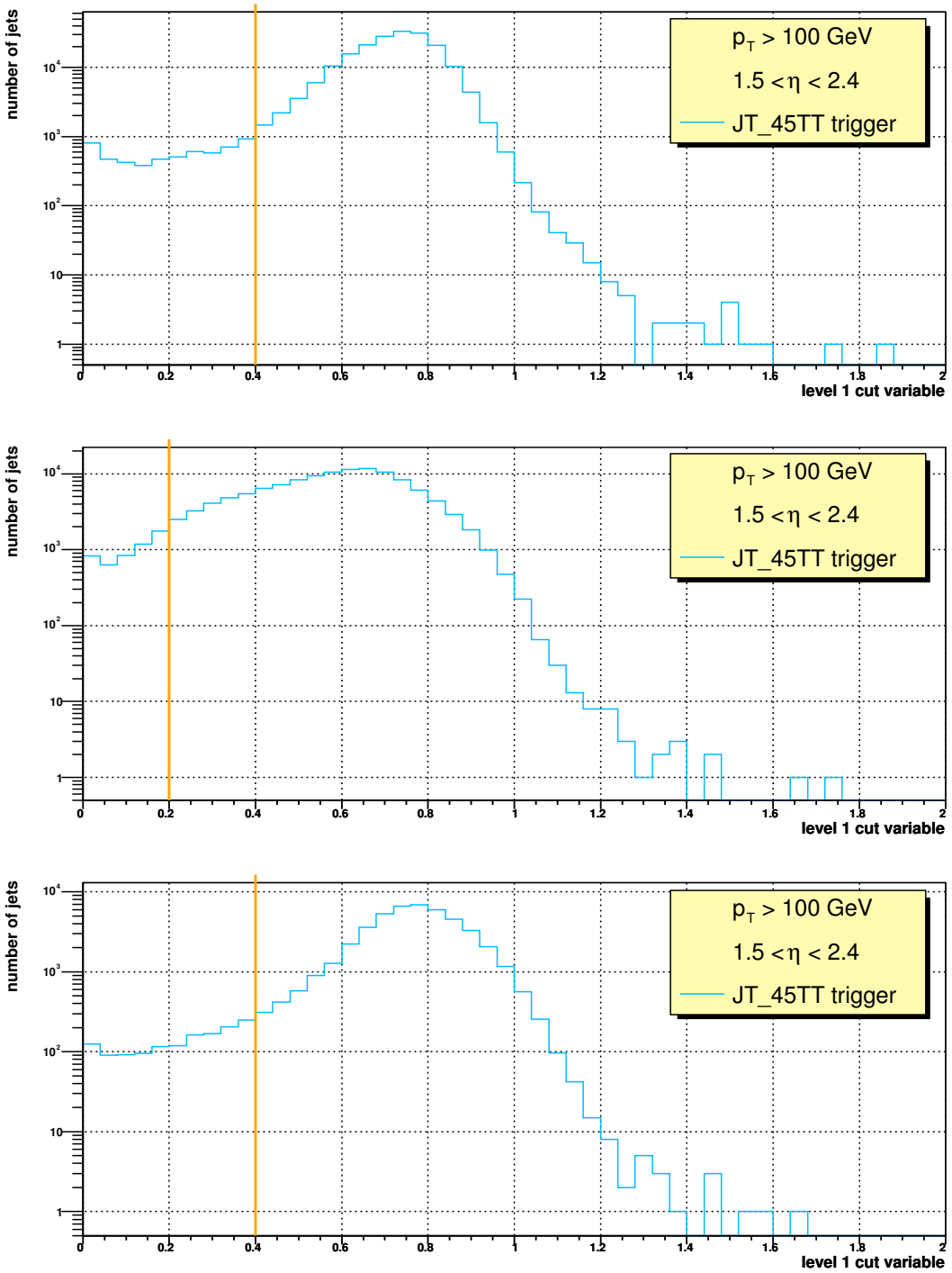

Figure 4.12: *The level-1 cut variabel of jets which satisfy all other jet cuts. Data from the trigger JT_45TT with a minimum transverse momentum of* 100 GeV *is shown.*

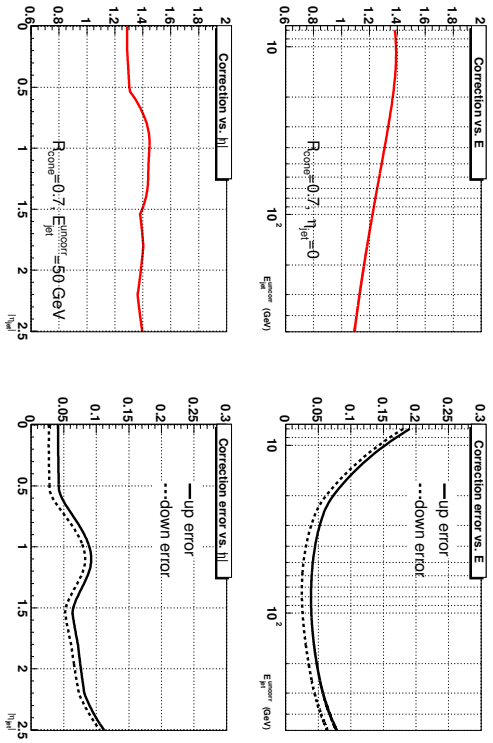

Figure 4.13: *Jet energy scale correction factor for DØ data and error versus transverse momentum and η for jets reconstructed with the improved legacy cone algorithm with $R = 0.7$ [28]. The higher factor for η between 0.6 and 1.5 and the higher error in this region is due to the change between central and endcap calorimeter*

Reasons for this are:

- energy deposited outside the jets cone
- different response in different regions of the detector
- an offset due to constant noise
- energy from underlying events
- different response to different particles

Since one is interested in the "true" energy of the jet, i.e. the energy the jets had on parton and particle level, a correction has to be made called jet energy scale (JES). It is parametrised in the following way with E_{corr} being the jet energy scale corrected energy and E_{uncorr} is the originally reconstructed energy within the jets cone:

$$E_{\text{corr}} = \frac{E_{\text{uncorr}} - O(\eta, \mathcal{L})}{R(E_{\text{uncorr}}, \eta) \cdot S(E_{\text{uncorr}}, \eta)} , \tag{4.3}$$

where O describes an offset due to calorimeter noise and additional simultaneous proton antiproton collisions. R corrects for the response of the calorimeter to the jet's energy. This factor takes into account that the calorimeter is instrumented differently depending on η, i.e. the uninstrumented parts in the Inter Cryostat region cause higher jet energy scales for this region in η than in regions of the central or endcap calorimeter. The fact that

not all of the jet's energy is deposited within the cone is corrected by S. The correction is parametrised as function of E_{uncorr} and η. In Fig. 4.13 the jet energy scale correction ($E_{\text{corr}}/E_{\text{uncorr}}$) is shown together with the error of the correction for improved legacy cone jets with a radius of $R = 0.7$. The uncertainty for jets above 30 GeV is approximately 6%.

The jet energy correction is determined from photon plus jets events in data and Monte Carlo simulation [29]. The photon's energy can be measured very precisely because the majority of its energy is deposited in one or at most two towers of the electromagnetic section so that no large event to event fluctuations occur. The energy of electromagnetic objects is calibrated using the decay of Z^0 or J/Ψ particles into electron positron pairs. Now it is required that the leading jet in a photon plus jets event lies in the opposite direction in φ to the photon. Using the law of momentum conservation, the jet's energy can be determined. Due to the fact that these events are rare at high transverse momentum, the statistical error rises in this region.

In this analysis the jet energy scale package jetcorr v5.3 is applied. Since the detector simulation is not perfect, a different jet energy scale has to be applied in data and Monte Carlo. This is done within the Top Analyze framework.

Chapter 5

Inclusive Jet Cross Section

In this chapter the measurement of the inclusive jet cross section is presented. A comparison between the measurement and theoretical predictions is made.

The cross section presented in this chapter is an inclusive differential jet cross section. "Inclusive" means that every event with at least one jet is used, no matter which other particles are in the event. Differential cross section in this analysis has the following meaning:

$$\frac{d\sigma}{dp_T} = \frac{N(p_{T\,\mathrm{bin}})}{\mathcal{L} \cdot \Delta p_{T\,\mathrm{bin}}}, \tag{5.1}$$

where p_T is the highest transverse momentum of a jet in an event. This jet is also called leading jet. The number of events with the transverse momentum within a bin with the mean $p_{T\,\mathrm{bin}}$ is $N(p_{T\,\mathrm{bin}})$. The measurement of the inclusive cross section was done for jets in different η regions, namely for $|\eta| < 0.5$, $0.5 < |\eta| < 1.0$, $1.0 < |\eta| < 1.5$, $1.5 < |\eta| < 2.0$ and $2.0 < |\eta| < 2.4$. Because the cross section decreases very steeply with increasing transverse momentum of the jet, different triggers as explained in Chapter 4 are used to minimise the amount of data but to have adequate statistics.

In addition to equation 5.1 efficiencies ϵ have to be taken into account. In particular this is the event selection efficiency ($\epsilon_{\mathrm{vertex}}$), which is approx. 89% for data and 95% for the PYTHIA Monte Carlo (see table 4.3). The jet cut effciency $\epsilon_{\mathrm{jetcut}}$ is determined from the Monte Carlo. It is assumed that the Monte Carlo events only contain propper jets, thus the inefficiency is 3%, which is the fraction of jets removed from the Monte Carlo by the jet cuts. Hence the differential cross section is:

$$\frac{d\sigma}{dp_T} = \frac{N_{\mathrm{jets}}(p_{T\,\mathrm{bin}})}{\mathcal{L} \cdot \Delta p_{T\,\mathrm{bin}} \cdot \epsilon_{\mathrm{vertex}} \cdot \epsilon_{\mathrm{jetcut}}} \tag{5.2}$$

5.1 Background

Due to the very high cross section of QCD processes, background from other Standard Model processes does not have to be considered.

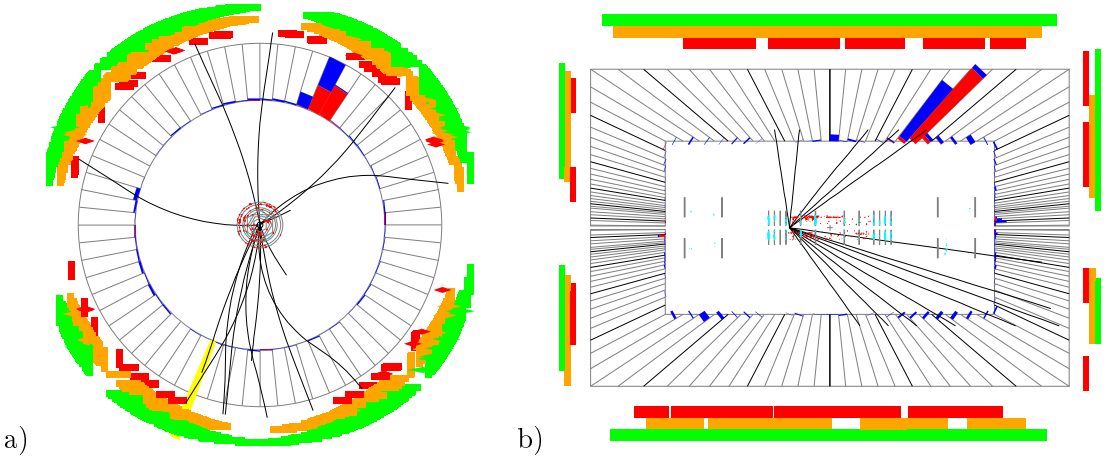

Figure 5.1: *A cosmic event captured by the DØ detector: a muon shower hit the detector which caused 45 muons to be reconstructed. Only one of the cosmic particles deposited a high energy in the calorimeter. Muons as minimal ionising particles usually deposit only a small energy in the calorimeter. a) is the view along the beam pipe and b) is the side view of the detector with protons coming from the left. The jet which was reconstructed has a transverse momentum of* $p_T = 569$ GeV *and the missing transverse energy not including the muons is* $E_T = 564$ GeV.

5.1.1 Cosmic Background

Cosmic showers are produced by high energy particles coming from anywhere in the universe. These particles interact with the atmosphere of the earth, generating many secondary particles of which mainly muons reach the ground. These particles interact with the detector. They might appear to be a "normal" event with strange properties, often with high missing transverse energy.

Because only events coming from hard proton antiproton interactions are of interest, it is not desired to leave such events in the final dataset. One could easily apply a cut against events with high missing transverse energy, but with these cuts interesting events with signatures for new physics might be removed, too. In order to be sensitive to such events, the fraction of events with a missing transverse energy higher than 70% of the highest transverse momentum of a jet was determined. In the complete sample this is a fraction of less than 0.5% so it is negligible compared to the uncertainty of the cross section measurement (see section 5.2). Only at transverse momenta above 400 GeV a closer look at these events is necessary. Out of approximately 70 events with jets above this transverse momentum, 12 were found to have such a high missing transverse energy, six of them with a transverse momentum of the highest jet above 500 GeV. Two representatives of these events are shown in Fig. 5.1 and 5.2.

10 of these events look much like cosmic events in the style of the one in Fig. 5.2 with hits in the muon chambers and entries on one side of the calorimeter as if a particle had gone sideways through the detector. Two look more like Fig. 5.1 with many hits in the muon system. Because no cut can be found which removes these events but does not remove possibel new phenomena, these events are removed by hand.

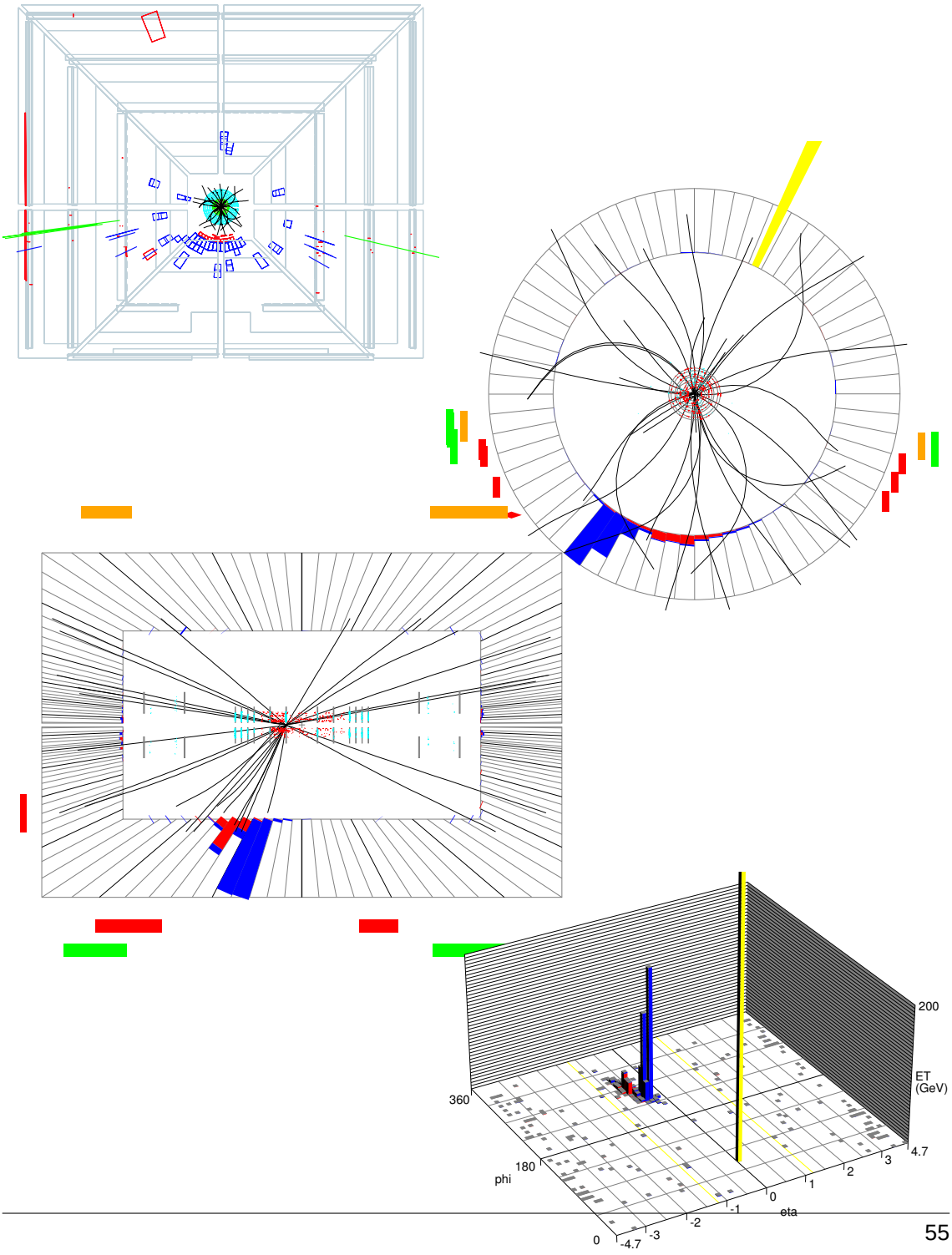

Figure 5.2: *Another example of an event caused by cosmic rays: A cosmic flew through the bottom of the detector leaving entries in the calorimeter as well as in the muon chambers. At the top left one can see the different detector components which were*

5.2 Error calculations

- **Statistical error:**
  The statistical error of each bin i with N entries is given by Poisson statistics [30]:

$$\Delta\left(\frac{d\sigma}{dp_T}\right)_{stat} = \left(\frac{d\sigma}{dp_T}\right) \cdot \frac{1}{\sqrt{N}} \,. \tag{5.3}$$

  This error is important at high transverse momenta of jets. For jets with a transverse momentum below 300 GeV the statistical error is less than 1%. Up to that point the bin width is taken to be 10 GeV for higher transverse momenta it is chosen to be bigger.

- **Systematic error:**

  – *Luminosity error:*
  As mentioned earlier, the luminosity can only be determined with an uncertainty of 6.5%.

  – *Jet energy scale error:*
  The error due to jet energy scale corrections is determined by varying the jet energy scale up and down by one σ and looking at the influence on the inclusive jet cross section. This is done on an event by event basis, as the error on the jet energy scale does depend on more parameters than just the transverse momentum. The one σ error for each bin is the difference between the measured value in this bin N and the value which would have been measured if the jet energy scale was one sigma higher or lower $N^{\pm jes}$:

$$\Delta\left(\frac{d\sigma}{dp_T}\right)_{jes} = \left|\frac{d\sigma}{dp_T} \cdot \frac{N - N^{\pm jes}}{N}\right| \,. \tag{5.4}$$

  This error is the dominant error in the measurement of the inclusive cross section. It is ≈20% for most of the bins in the central η region ($|\eta| < 0.5$), becoming even larger for higher transverse momenta or higher pseudorapidities.

  – *Other systematic errors:*
  Various other systematic errors come from the different cuts applied on events and jets. The vertex cut efficiency for example varies between 89% and 90%. Thus the overall vertex efficiency for the different triggers used is assumed to be $\epsilon_{\text{vertex}}(\text{data}) = (89.5 \pm 0.5)\%$ in data and $\epsilon_{\text{jetcut}}(\text{mc}) = (95.0 \pm 0.5)\%$ in Monte Carlo. The jet cuts remove approximately 7% of jets. The efficiency determined from Monte Carlo is 97%. The difference between this value and the number of events removed from the data is taken to be the error, thus $\epsilon_{\text{jetcut}} = (97^{+3}_{-4}\%)$.

According to error propagation of uncorrelated Gaussian errors [30] the overall systematic error on the differentioal cross section of each bin i is:

$$\begin{aligned}\left(\Delta\left(\frac{d\sigma}{dp_T}\right)_{sys}\right)^2 &= \left|\frac{d\frac{d\sigma}{dp_T}}{d\mathcal{L}}\right|^2 \cdot \Delta\mathcal{L}^2 + \left(\Delta\left(\frac{d\sigma}{dp_T}\right)_{jes}\right)^2 + \left[(0.5\%)^2 + (3\%)^2\right] \cdot \left(\frac{d\sigma}{dp_T}\right)^2 \\ &= \left(\frac{d\sigma}{dp_T}\right)^2 \cdot \frac{\Delta\mathcal{L}}{\mathcal{L}} + \left(\Delta\left(\frac{d\sigma}{dp_T}\right)_{jes}\right)^2 + \left[(0.5\%)^2 + (3\%)^2\right] \cdot \left(\frac{d\sigma}{dp_T}\right)^2 \\ &= \left(\Delta\left(\frac{d\sigma}{dp_T}\right)_{jes}\right)^2 + \left[(6.5\%)^2 + (0.5\%)^2 + (3\%)^2\right] \cdot \left(\frac{d\sigma}{dp_T}\right)^2 \qquad (5.5)\end{aligned}$$

The overall error for each bin is given by adding the statistical and the systematic error in quadrature.

5.3 Distribution in η and φ

To find detector problems affecting only some parts of the detector, the η and φ distributions were studied (see Fig. 5.3). No irregularities could be found. The distribution is flat in φ and symmetric in η. Data and Monte Carlo distributions of these variables are in good agreement. A η comparison between data and Monte Carlo for jets with a transverse momentum greater than 130 GeV is given in Fig. 5.4.

5.4 Results

The event with the highest transverse momenta contains two jets with transverse momenta above 500 GeV. This event is displayed in Fig. 5.5. These two jets are back to back in φ. This is exactly what is for a pure QCD process without leptons.

The inclusive jet p_T spectra for the different η regions are displayed in Fig. 5.6-5.10. These spectra are compared to a PYTHIA Monte Carlo with full detector simmulation and a next to leading order NLOJET++ [31] QCD calculation for jet production using the CTEQ6.1M parton distribution functions. The energy scale is chosen to be $\mu = p_T/2$. The next to leading order Monte Carlo were made for a transverse momentum above 50 GeV. The data of the first two bins has to be treated with care, since they were determined with the trigger `JT_8TT` of which no trigger efficiency was determined directly. One overlapping bin in p_T is printed between two triggers to see, weather the cross sections agree with each other within the errors. As one can see in Fig. 5.1-5.5 they do so. This comparison is not made between the triggers `JT_8TT` and `JT_15TT` since the statistics of the lower trigger were allready very poor.

Data and next to leading order calculation are in good agreement for the $|\eta| < 0.5$, $1.5 < |\eta| < 2.0$ and $2.0 < |\eta| < 2.4$. Only in the first bins in the central rapidity region the predictions seem to be to low. In the two other pseudorapidity bins $0.5 < |\eta| < 1.0$ and $1.0 < |\eta| < 1.5$ the data and NLOJET++ calculation do agree but a strong tendency for the data to be above the prediction. This region in η corresponds to the Inter Cryostat

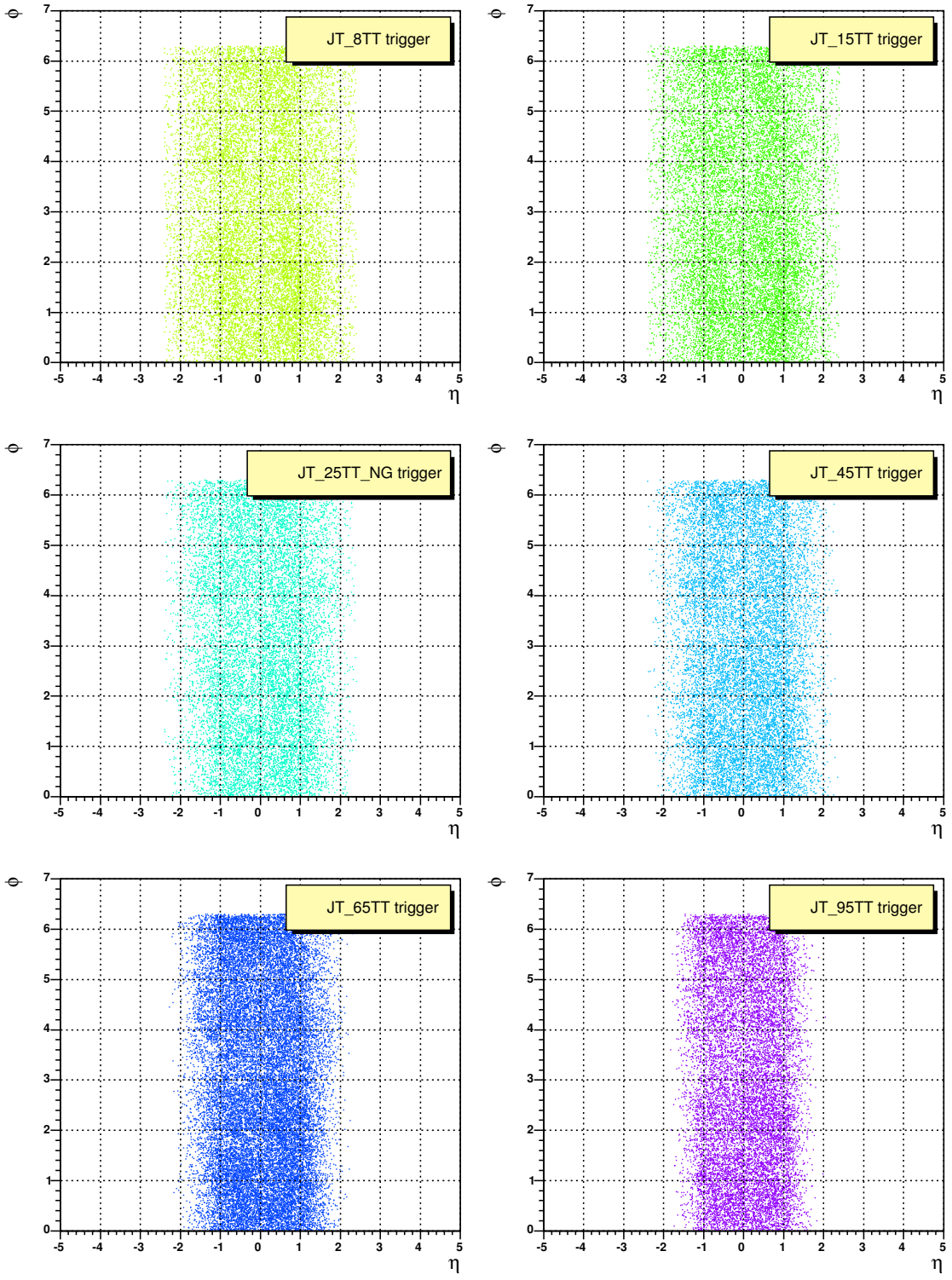

Figure 5.3: *The $\eta - \varphi$ distribution of the leading jet in each event for the different triggers.*

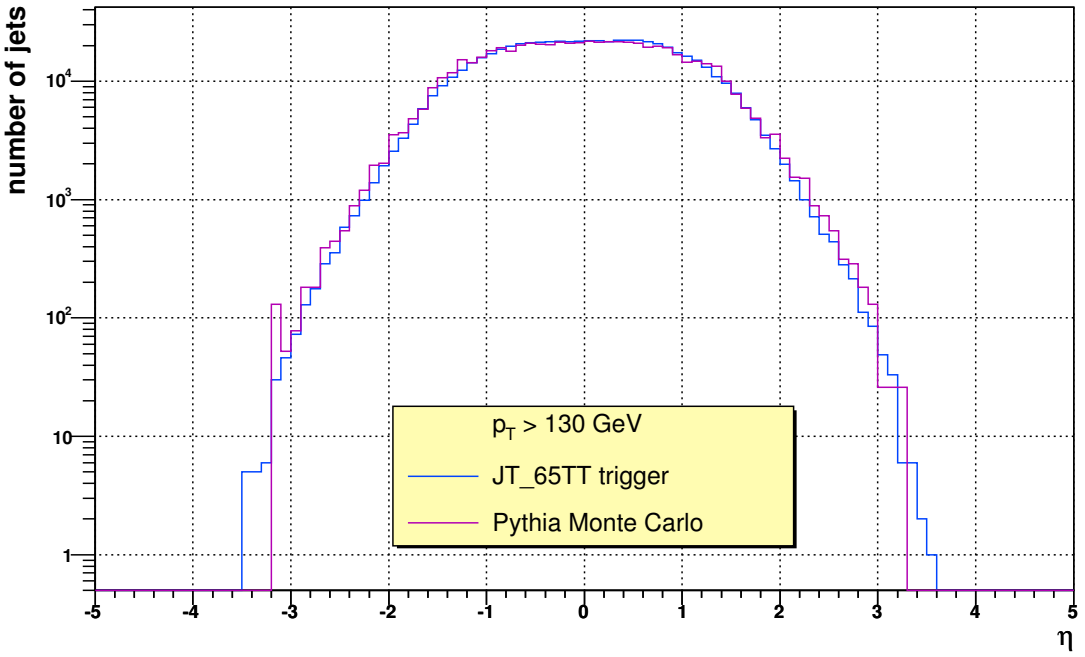

Figure 5.4: *The eta distribution in data and Monte Carlo for jets with* $p_T > 130$ gev.

Region of the detector. This region needs further understanding, in particular regarding the jet energy scale.

Another measurement of the inclusive jet cross section has been made within the DØ collaboration for jets with more than 80 GeV [32]. The two measurements agree with each other, however the other measurement tends to measure a slightly lower cross section ($\approx 10\%$) in the first five bins of the pseudorapidity regions $|\eta| < 0.5$ and $0.5 < |\eta| < 1.0$. But this is still within the systematic uncertainties.

The PYTHIA Monte Carlo predictions are generally lower than the next to leading order calculations except for some high p_T regions. This is probably due to missing higher orders. Only in the pseudorapidity range $1.0 < |\eta| < 1.5$ both predicions are very simmilar. Here the data is higher than the next to leading order calculation as well.

This measurement does not indicate any deviations from QCD predictions. Unfortunately the error due to the uncertainty in the jet energy scale is very large so that no small deviations, which might indicate new physics would be noticed.

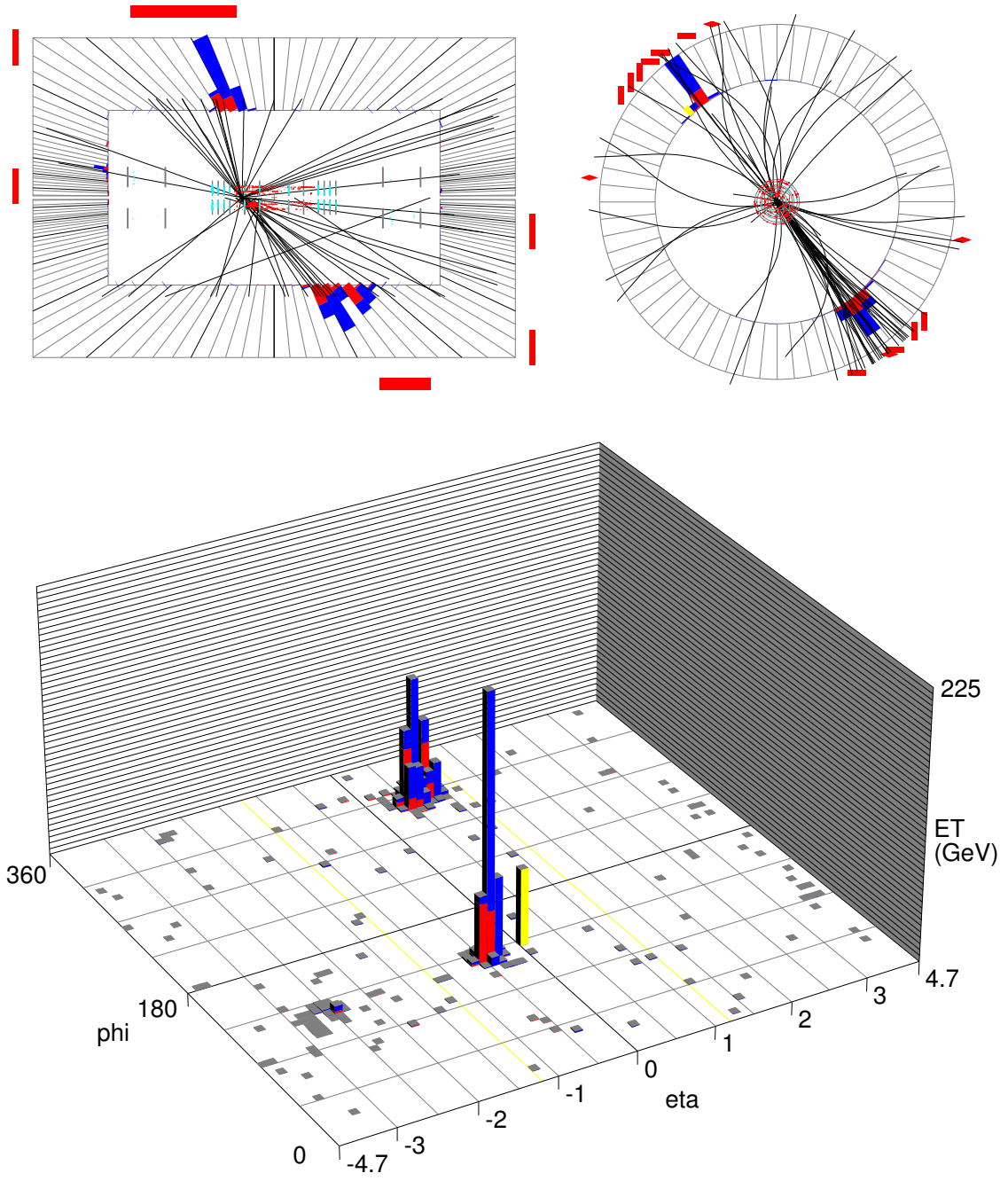

Figure 5.5: *Event with jets with the highest transverse momentum in the sample. Top left the side view on the detector with protons coming from the right, top right a view along the beam pipe. At the bottom a plot of the calorimeter entries in η and φ. The jet with highest transverse momentum was measured with $p_T = 528$ GeV, $\eta = 0.79$ and $\varphi = 307°$ the other jet with $p_T = 507$ GeV, $\eta = -0.26$ and $\varphi = 127°$ respectively. As expected for a pure QCD event they are back to back in φ.*

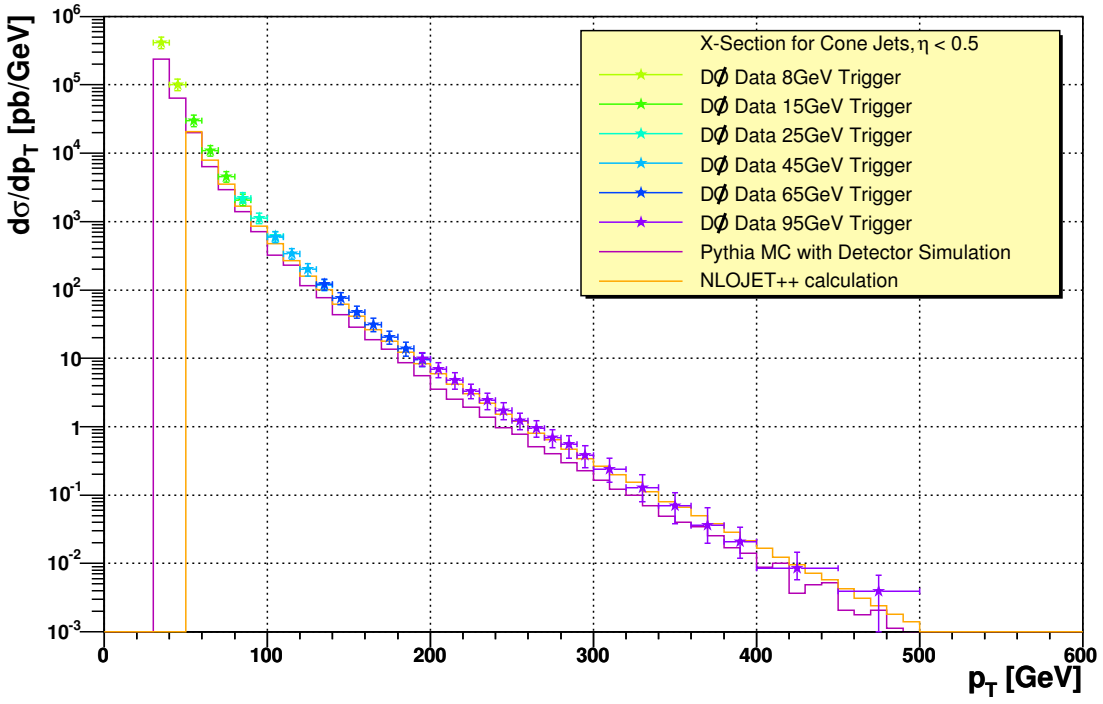

Figure 5.6: *The inclusive jet p_T spectrum for $\eta < 0.5$.*

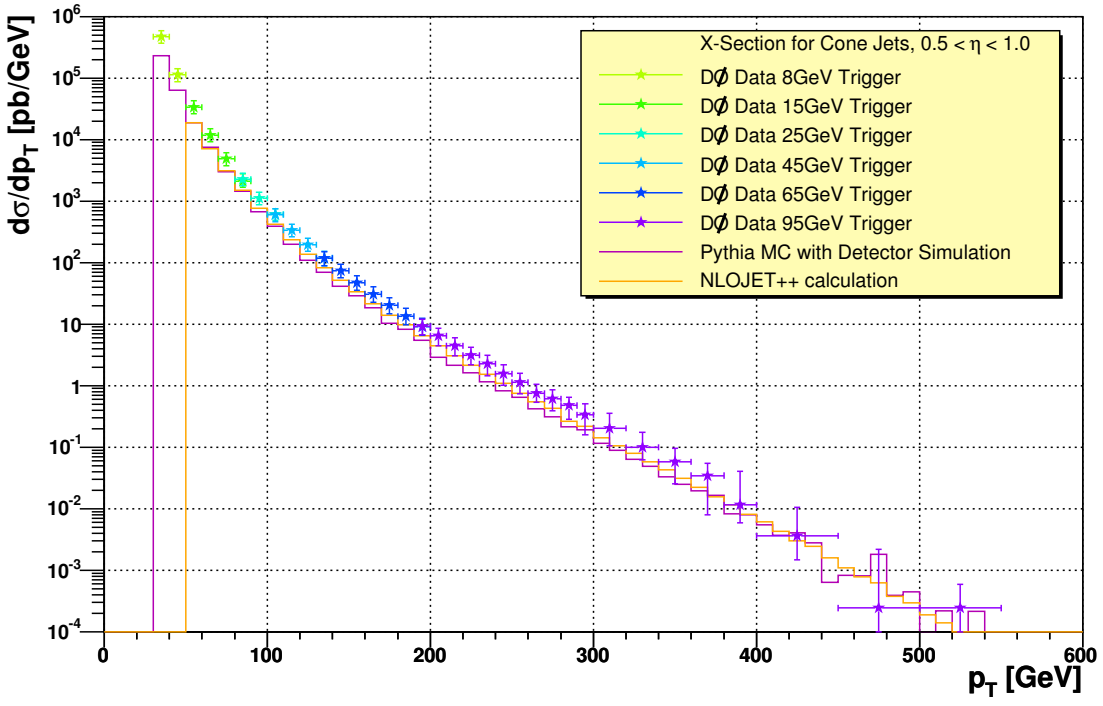

Figure 5.7: *The inclusive jet p_T spectrum for $0.5 < \eta < 1.0$.*

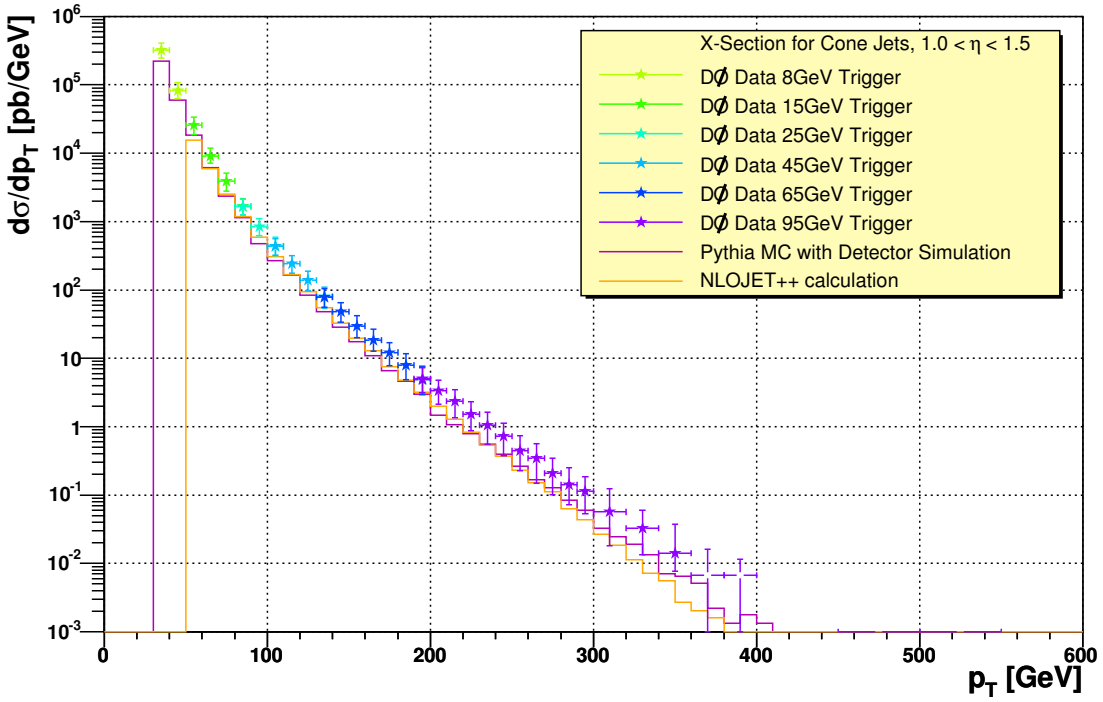

Figure 5.8: *The inclusive jet p_T spectrum for* $1.0 < \eta < 1.5$.

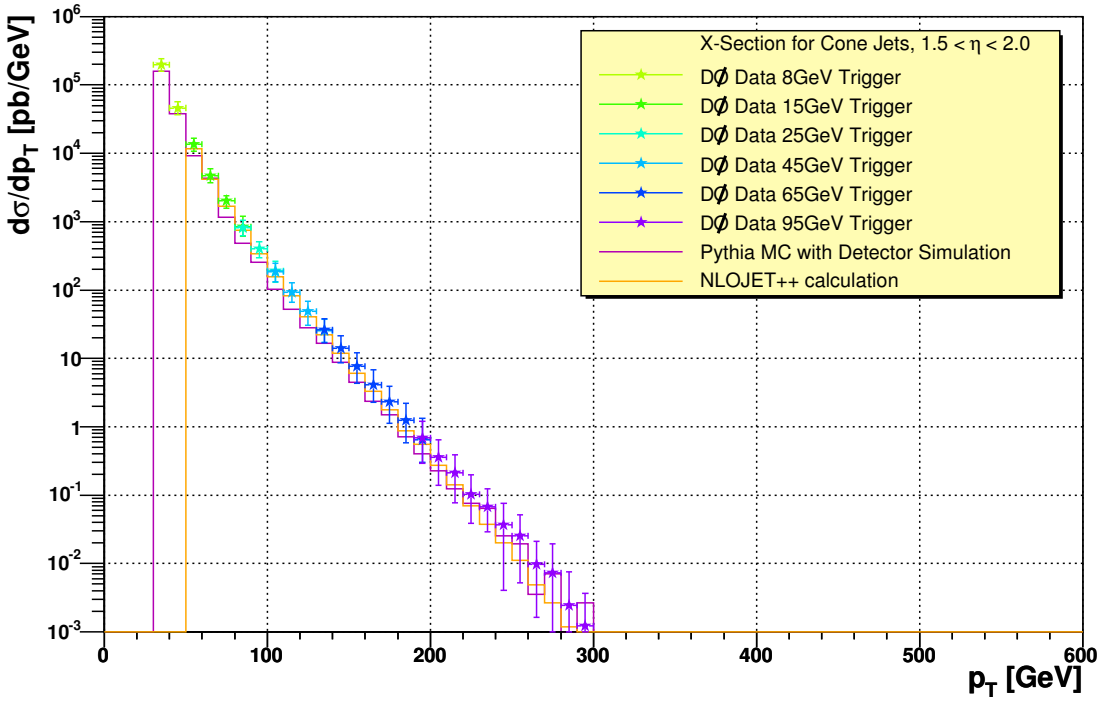

Figure 5.9: *The inclusive jet p_T spectrum for* $1.5 < \eta < 2.0$.

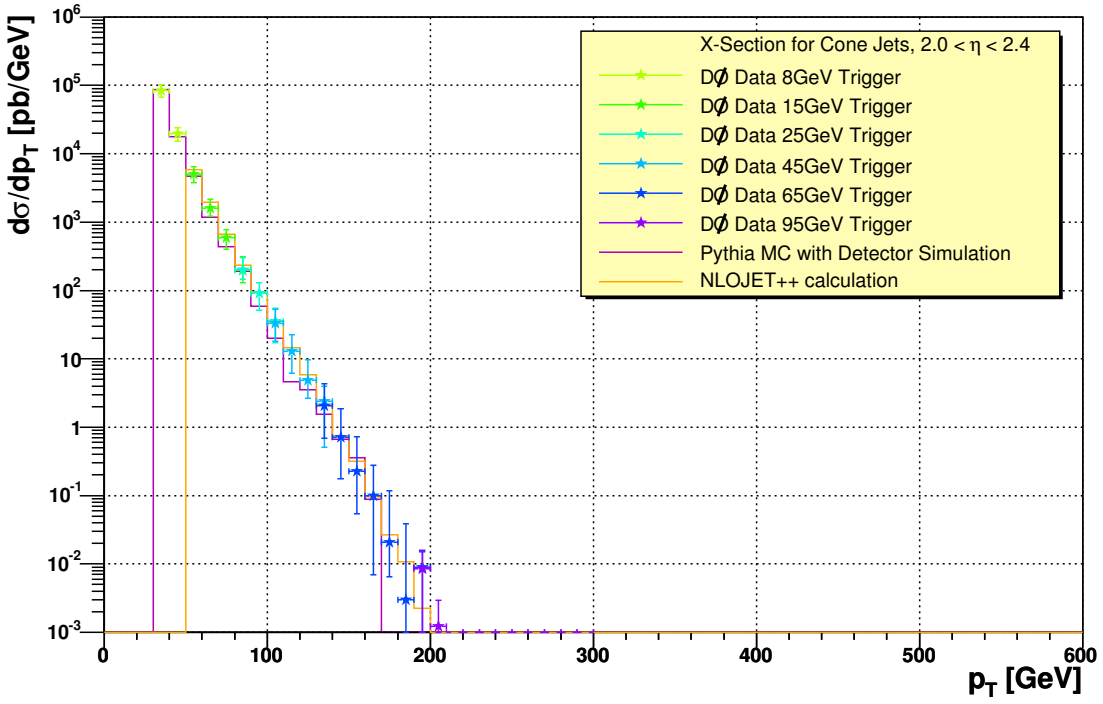

Figure 5.10: *The inclusive jet p_T spectrum for $2.0 < \eta < 2.4$.*

Table 5.1: *Inclusive jet cross section for $\eta < 0.5$.*

p_T range [GeV]	trigger	σ [pb]	stat [pb]	sys [pb]
30 - 40	JT_8TT	414600	2100	+87500 -75700
40 - 50	JT_8TT	100300	1000	+20500 -18300
50 - 60	JT_15TT	29800	300	+6200 -5300
60 - 70	JT_15TT	11000	200	+1800 -1900
70 - 80	JT_15TT	4600	100	+800 -800
80 - 90	JT_15TT	2070.7	70	+440 -350
80 - 90	JT_25TT_NG	2210	20	+410 -360
90 - 100	JT_25TT_NG	1120	20	+210 -190
100 - 110	JT_25TT_NG	610	10	+100 -110
100 - 110	JT_45TT	593	4	+114 -104
110 - 120	JT_45TT	337	3	+63 -56
120 - 130	JT_45TT	202	2	+39 -42
130 - 140	JT_45TT	117	2	+24 -19
130 - 140	JT_65TT	120.6	0.6	+23.5-21.8
140 - 150	JT_65TT	75.2	0.5	+16.5 -14.8
150 - 160	JT_65TT	47.5	0.4	+10.8 -9.0
160 - 170	JT_65TT	31.0	0.3	+7.3 -6.6
170 - 180	JT_65TT	20.5	0.2	+4.6 -4.3
180 - 190	JT_65TT	13.92	0.20	+3.31 -3.18
190 - 200	JT_65TT	9.49	0.17	+2.45 -1.93
190 - 200	JT_95TT	9.86	0.11	+2.42 -2.14
200 - 210	JT_95TT	6.87	0.09	+1.90 -1.62
210 - 220	JT_95TT	4.78	0.08	+1.44 -1.24
220 - 230	JT_95TT	3.32	0.06	+0.96 -0.78
230 - 240	JT_95TT	2.42	0.05	+0.65 -0.65
240 - 250	JT_95TT	1.72	0.05	+0.59 -0.46
250 - 260	JT_95TT	1.22	0.04	+0.41 -0.31
260 - 270	JT_95TT	0.94	0.03	+0.32 -0.24
270 - 280	JT_95TT	0.69	0.03	+0.23 -0.20
280 - 290	JT_95TT	0.55	0.03	+0.17 -0.21
290 - 300	JT_95TT	0.38	0.02	+0.17 -0.13
300 - 320	JT_95TT	0.240	0.012	+0.107 -0.084
320 - 340	JT_95TT	0.129	0.009	+0.069 -0.049
340 - 360	JT_95TT	0.070	0.007	+0.038 -0.032
360 - 380	JT_95TT	0.036	0.005	+0.029 -0.015
380 - 400	JT_95TT	0.0207	0.0035	+0.0129 -0.0081
400 - 450	JT_95TT	0.0085	0.0014	+0.0059 -0.0023
450 - 500	JT_95TT	0.0039	0.0010	+0.0027 -0.0032

Table 5.2: *Inclusive jet cross section for* $0.5 < \eta < 1.0$.

p_T range [GeV]	trigger	σ [pb]	stat [pb]	sys [pb]
30 - 40	JT_8TT	470300	2300	+118400 -98800
40 - 50	JT_8TT	112800	1100	+29600 -25300
50 - 60	JT_15TT	33400	300	+9100 -7300
60 - 70	JT_15TT	11800	200	+3100 -2600
70 - 80	JT_15TT	4900	100	+1200 -1100
80 - 90	JT_15TT	2120	70	+650 -420
80 - 90	JT_25TT_NG	2250	20	+5990 -490
90 - 100	JT_25TT_NG	1121	16	+278 -248
100 - 110	JT_25TT_NG	617	12	+140 -131
100 - 110	JT_45TT	599	4	+156 -133
110 - 120	JT_45TT	338	3	+86 -76
120 - 130	JT_45TT	196	2	+54 -44
130 - 140	JT_45TT	119.1	1.6	+34.4 -30.1
130 - 140	JT_65TT	118.4	0.6	+33.1 -28.6
140 - 150	JT_65TT	73.9	0.5	+20.4 -17.6
150 - 160	JT_65TT	47.2	0.4	+14.0 -11.5
160 - 170	JT_65TT	30.9	0.3	+9.5 -8.1
170 - 180	JT_65TT	20.3	0.2	+6.5 -5.7
180 - 190	JT_65TT	13.4	0.2	+4.8 -3.6
190 - 200	JT_65TT	9.16	0.17	+3.24 -2.54
190 - 200	JT_95TT	9.21	0.11	+3.43 -2.47
200 - 210	JT_95TT	6.50	0.09	+2.18 -2.00
210 - 220	JT_95TT	4.43	0.07	+1.80 -1.38
220 - 230	JT_95TT	3.15	0.06	+1.22 -0.94
230 - 240	JT_95TT	2.27	0.05	+0.91 -0.81
240 - 250	JT_95TT	1.57	0.045	+0.73 -0.55
250 - 260	JT_95TT	1.138	0.037	+0.545 -0.402
260 - 270	JT_95TT	0.757	0.030	+0.431 -0.213
270 - 280	JT_95TT	0.613	0.027	+0.268 -0.218
280 - 290	JT_95TT	0.477	0.024	+0.164 -0.189
290 - 300	JT_95TT	0.338	0.020	+0.162 -0.178
300 - 320	JT_95TT	0.202	0.011	+0.157 -0.096
320 - 340	JT_95TT	0.100	0.008	+0.075 -0.037
340 - 360	JT_95TT	0.0577	0.0059	+0.0386 -0.0319
360 - 380	JT_95TT	0.0346	0.0046	+0.0196 -0.0263
380 - 400	JT_95TT	0.0115	0.0026	+0.0286 -0.0050
400 - 450	JT_95TT	0.0036	0.0009	+0.0068 -0.0020
450 - 500	JT_95TT	0.00024	0.00024	+0.00195 -0.00002
500 - 550	JT_95TT	0.00024	0.00024	+0.00024 -0.00024

Table 5.3: *Inclusive jet cross section for* $1.0 < \eta < 1.5$.

p_T range [GeV]	trigger	σ [pb]	stat [pb]	sys [pb]
30 - 40	JT_8TT	320200	19008	+88200 -75700
40 - 50	JT_8TT	82500	900	+25700 -20100
50 - 60	JT_15TT	25600	240	+8150 -6760
60 - 70	JT_15TT	9090	140	+2670 -1930
70 - 80	JT_15TT	3880	90	+1200 -1090
80 - 90	JT_15TT	1670	60	+500 -430
80 - 90	JT_25TT_NG	1660	19	+462 -390
90 - 100	JT_25TT_NG	847	14	+257 -225
100 - 110	JT_25TT_NG	434	10	+153 -118
100 - 110	JT_45TT	433	3	+133 -112
110 - 120	JT_45TT	242	2	+76 -65
120 - 130	JT_45TT	138.3	1.8	+48.3 -40.4
130 - 140	JT_45TT	80.2	1.3	+30.2 -26.1
130 - 140	JT_65TT	77.9	0.5	+26.3 -21.8
140 - 150	JT_65TT	48.2	0.4	+17.3 -14.6
150 - 160	JT_65TT	29.7	0.3	+12.4 -9.6
160 - 170	JT_65TT	18.5	0.2	+8.0 -5.9
170 - 180	JT_65TT	12.2	0.2	+4.9 -4.4
180 - 190	JT_65TT	7.9	0.2	+3.8 -3.0
190 - 200	JT_65TT	4.9	0.1	+2.8 -1.9
190 - 200	JT_95TT	5.02	0.08	+2.78 -1.86
200 - 210	JT_95TT	3.34	0.06	+1.78 -1.21
210 - 220	JT_95TT	2.35	0.05	+1.18 -1.01
220 - 230	JT_95TT	1.51	0.04	+0.97 -0.64
230 - 240	JT_95TT	1.05	0.06	+0.69 -0.49
240 - 250	JT_95TT	0.721	0.030	+0.462 -0.343
250 - 260	JT_95TT	0.447	0.023	+0.379 -0.218
260 - 270	JT_95TT	0.346	0.021	+0.235 -0.196
270 - 280	JT_95TT	0.209	0.016	+0.169 -0.107
280 - 290	JT_95TT	0.142	0.013	+0.172 -0.069
290 - 300	JT_95TT	0.114	0.012	+0.084 -0.060
300 - 320	JT_95TT	0.057	0.006	+0.066 -0.038
320 - 340	JT_95TT	0.0328	0.0045	+0.0269 -0.0190
340 - 360	JT_95TT	0.0140	0.0029	+0.0231 -0.0056
360 - 380	JT_95TT	0.0067	0.0020	+0.0091 -0.0055
380 - 400	JT_95TT	0.0067	0.0020	+0.0043 -0.0061
400 - 450	JT_95TT	0.00049	0.00034	+0.00438 -0.00003

Table 5.4: *Inclusive jet cross section for* $1.5 < \eta < 2.0$.

p_T range [GeV]	trigger	σ [pb]	stat [pb]	sys [pb]
30 - 40	JT_8TT	197100	1500	+43400 -39000
40 - 50	JT_8TT	46000	700	+10800 -9100
50 - 60	JT_15TT	13500	170	+3050 -2770
60 - 70	JT_15TT	4730	100	+1190 -1030
70 - 80	JT_15TT	2018	67	+388 -446
80 - 90	JT_15TT	844	43	+347 -228
80 - 90	JT_25TT_NG	818	13	+239 -194
90 - 100	JT_25TT_NG	401	9	+104 -102
100 - 110	JT_25TT_NG	191.6	6.5	+73.8 -61.4
100 - 110	JT_45TT	185.7	2.0	+62.3 -54.0
110 - 120	JT_45TT	93.1	1.4	+35.2 -27.0
120 - 130	JT_45TT	48.9	1.0	+20.0 -18.3
130 - 140	JT_45TT	25.3	0.8	+12.2 -8.2
130 - 140	JT_65TT	26.0	0.3	+11.8 -9.2
140 - 150	JT_65TT	14.1	0.2	+7.2 -5.6
150 - 160	JT_65TT	7.64	0.15	+4.38 -3.33
160 - 170	JT_65TT	4.08	0.11	+2.76 -1.81
170 - 180	JT_65TT	2.31	0.08	+1.62 -1.18
180 - 190	JT_65TT	1.25	0.06	+0.96 -0.66
190 - 200	JT_65TT	0.642	0.044	+0.688 -0.335
190 - 200	JT_95TT	0.683	0.0288	+0.676 -0.388
200 - 210	JT_95TT	0.356	0.0208	+0.393 -0.217
210 - 220	JT_95TT	0.212	0.016	+0.230 -0.134
220 - 230	JT_95TT	0.102	0.011	+0.145 -0.063
230 - 240	JT_95TT	0.0669	0.0090	+0.0828 -0.0369
240 - 250	JT_95TT	0.0365	0.0067	+0.0463 -0.0317
250 - 260	JT_95TT	0.0255	0.0056	+0.0317 -0.0196
260 - 270	JT_95TT	0.0097	0.0034	+0.0158 -0.0073
270 - 280	JT_95TT	0.00730	0.0030	+0.0182 -0.0073
280 - 290	JT_95TT	0.00243	0.00172	+0.00973 -0.00243
290 - 300	JT_95TT	0.00122	0.00122	+0.00365 -0.00122

Table 5.5: *Inclusive jet cross section for* $2.0 < \eta < 2.4$.

p_T range [GeV]	trigger	σ [pb]	stat [pb]	sys [pb]
30 - 40	JT_8TT	83500	1000	+18100 -16200
40 - 50	JT_8TT	19740	460	+4490 -4350
50 - 60	JT_15TT	5010	110	+1450 -1270
60 - 70	JT_15TT	1600	60	+550 -390
70 - 80	JT_15TT	593	36	+173 -190
80 - 90	JT_15TT	198	21	+114 -64
80 - 90	JT_25TT_NG	202	7	+98 -56
90 - 100	JT_25TT_NG	90.5	4.5	+40.1 -39.0
100 - 110	JT_25TT_NG	35.2	2.8	+19.4 -17.8
100 - 110	JT_45TT	33.0	0.9	+19.9 -15.0
110 - 120	JT_45TT	12.82	0.53	+9.60 -6.64
120 - 130	JT_45TT	4.85	0.33	+4.84 -2.19
130 - 140	JT_45TT	2.40	0.23	+1.53 -1.88
130 - 140	JT_65TT	2.05	0.08	+2.27 -1.35
140 - 150	JT_65TT	0.72	0.05	+1.16 -0.54
150 - 160	JT_65TT	0.227	0.026	+0.496 -0.171
160 - 170	JT_65TT	0.099	0.017	+0.176 -0.090
170 - 180	JT_65TT	0.0209	0.0079	+0.0955 -0.0121
180 - 190	JT_65TT	0.0030	0.0030	+0.0358 -0.0002
190 - 200	JT_65TT	0.0090	0.0052	+0.0031 -0.0090
190 - 200	JT_95TT	0.0085	0.0032	+0.0049 -0.0085
200 - 210	JT_95TT	0.00122	0.00122	+0.00122 -0.00122

Chapter 6

Multijet Cross Section

In this chapter the rate of events containing three, four, five and more jets relative to the rate of events with two jets is studied. This ratio is not sensitive to the error of the luminosity. The error in the Monte Carlo prediction due to the uncertainty of the parton density function and the fact that higher orders are neglected is reduced by this approach, too. In order to obtain this ratio for particle level jets the data have to be unfolded. The unfolding algorithm as well as the results are presented here and compared to a leading order Monte Carlo prediction.

The following cuts are applied in this part of the analysis:

- The event satisfies the cuts expalained in chapter 4.3.
- The event contains at least one jet with: $p_T > 50$ GeV, $|\eta| < 2.4$.
- Only jets which fulfil the standard jet cuts (see chapter 4.4) are counted.
  $\Rightarrow$ only jets with $p_T > 30$ GeV, $|\eta| < 2.4$ are used.

The rates for up to three jets ar determined with events triggered by the trigger `JT_15TT`, higher rates with the trigger `4JT10`. The four-jet-rate determined from `JT_15TT` trigger events is in good agreement with the four-jet-rate from the `4JT10` trigger. Events with more than six jets are included in the six-jet-rate.

To compare the results obtained from the data with theoretical predictions events from ALPGEN as well as PYTHIA Monte Carlo generators are used. The events generated with ALPGEN are also used to undfold the data.

6.1 Background

As for the inclusive cross section, the background from other standard model processes can be neglected. But in the case of an underlying event high jet multiplicity might be faked. E.g. in case of a three-jet-event and an additional two-jet-event in the same bunch crossing, five jets are reconstructed. Since all jets are reconstructed pointing to the same

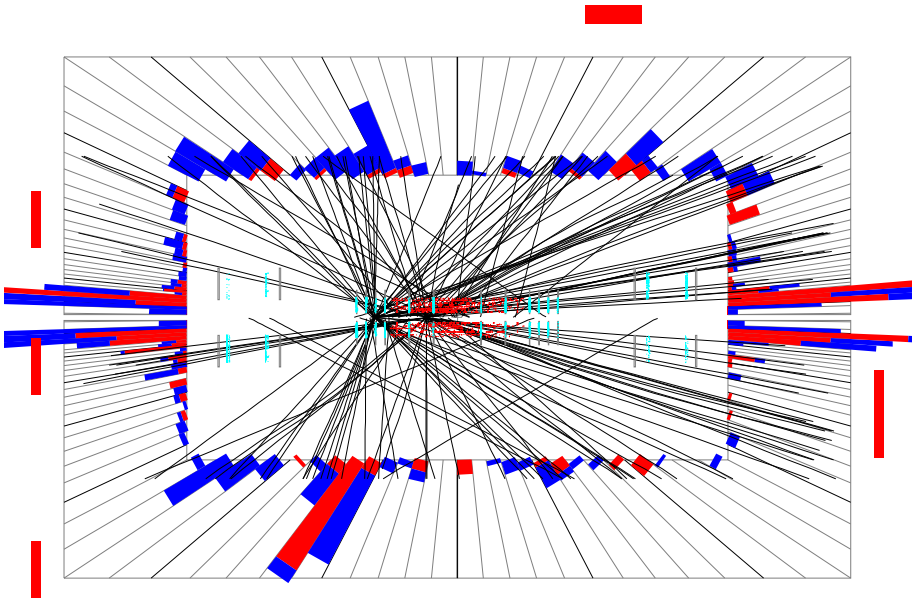

Figure 6.1: *An example of two interactions inside the same bunch crossing faking a high jet multiplicity.*

vertex (namely the one with the best fit), these two events cannot easily be separated. An example of such an event is given in Fig. 6.1.

The rate of these fake high jet multiplicities is estimated from the multijet cross sections derived from an ALPGEN Monte Carlo and the medium instantaneous luminosity of $\mathcal{L}_{\text{inst}} = 20 \cdot 10^{30}\ \text{cm}^{-2}\text{s}^{-1}$. The expected number for n jet production is determined, where n is the number of jets in an event and the minimum transverse momentum of all jets is 30 GeV and 50 GeV for the leading jet:

$$N_{n\text{jet}} = \mathcal{L}_{\text{int}} \cdot \sigma_{n\text{jet}} \ . \tag{6.1}$$

The resulting number of events for the different triggers are listed in Tab. 6.1. These numbers are based on the luminosity of the `4JT10` trigger of $\mathcal{L}_{\text{int}} = 1.19\ \text{pb}^{-1}$. Now the average number $\mu_{n\text{jet}}$ of n jet events per bunch crossing is calculated requiring a transverse momentum above 30 GeV for each jet. This number depends on the instantaneous luminosity, on the frequency of bunch crossings as well as on the cross section for n jets above 30 GeV [33]:

$$\mu_{n\text{jet}} = \frac{\mathcal{L}_{\text{inst}}}{\nu} \cdot \sigma_{n\text{jet}} \ . \tag{6.2}$$

The frequency of bunch crossings is $\nu = 1.7$ MHz. Only the rates for two, three and four-jet-production are of interest as events with more than six jets are included in the rate of

six jets and more. These rates are given in Tab. 6.1. E.g. the number of fake five-jet-events for the given luminosity is:

$$\begin{aligned} N_{5\text{jet}}(\text{fake}) &= \mu_{3\text{jet}} \cdot N_{2\text{jet}} + \mu_{2\text{jet}} \cdot N_{3\text{jet}} \\ &= 17.32\,. \end{aligned} \tag{6.3}$$

The expected number of fake events are given in Tab. 6.1. This estimate shows that the number of fake events is expected to be of order 1%, hence they are neglected.

6.2 Unfolding jet multiplicities

Only the number of detector jets per event can be extracted from the data. As mentioned in Chapter 3, the properties and multiplicity of these detector jets depend on geometry, jet energy scale and other detector effects. In order to be able to compare the results with other experiments or theory, the number of jets on particle level has to be determined, because these particle jets do not depend on detector properties.

First the probability to see i detector jets if j particle jets were produced is determined from an ALPGEN Monte Carlo. Five classes for events with two, three, four, five and six(plus more) events are introduced. In each case the leading jet has to have a transverse momentum above 50 GeV. The other jets must have a minimum transverse momentum of 30 GeV. Now the jet momentum on particle level is not exactly the one measured on detector level. Thus it is possible that there is one jet, e.g. with 51 GeV and two with more than 30 GeV transverse momentum, but on detector level the leading jet is reconstructed with 49 GeV. So the event is not counted in any of the classes described above. To avoid this problem, one more class, called "1-jet" is defined by requiring at least one jet with 30 GeV. Because there are still events in which no particle level jet fulfilling the requirements is found, on detector level, the "0-jet" or background class is added for the particle level jet classes. An event is added to this class if jets are reconstructed and satisfying the cuts on detector level. Thus all events with jets on detector level contribute to the conditional probability $P(i\text{Djets}|j\text{Pjets})$ i.e. the probability that i detector jets are seen on condition that j particle jets were in the event.

n jets	2	3	4	5	6
$\sigma_{n\text{jets}}$(50 GeV) [pb]	$5.6 \cdot 10^5$	$2.4 \cdot 10^4$	$6.4 \cdot 10^3$	$5.5 \cdot 10^2$	18
Number of events	666400	28560	7616	655	21
$\sigma_{n\text{jets}}$(30 GeV) [pb]	$1.5 \cdot 10^6$	$6.5 \cdot 10^4$	$4.6 \cdot 10^3$	—	—
$\mu_{n\,jets}$	$2.6 \cdot 10^{-5}$	$1.1 \cdot 10^{-6}$	$8.1 \cdot 10^{-8}$	—	—
Number of fake events	—	—	17.3	1.46	0.283

Table 6.1: *Expected number of events containing n jets (based on an* ALPGEN *Monte Carlo simulation).*

The unfolding is done with a multidimensional unfolding method by G. D'Agostini [34]. This method is based on Bayes' Theorem which connects the conditional probabilities $P(B|A)$ and $P(A|B)$:

$$P(B|A) = \frac{P(A|B) \cdot P(B)}{P(A)} . \tag{6.4}$$

In the case of jet multiplicities, A is the number of detector jets (iDJets) and B is the number of particle jets (jPJets) in one event. Using the law of total probability:

$$P(i\text{DJets}) = \sum_{k=0}^{n_{max}} P(i\text{DJets}|k\text{PJets}) \cdot P(k\text{PJets}) , \tag{6.5}$$

this leads to:

$$P(j\text{PJets}|i\text{DJets}) = \frac{P(i\text{DJets}|j\text{PJets}) \cdot P(j\text{PJets})}{\sum_{k=0}^{n_{max}} P(i\text{DJets}|k\text{PJets}) \cdot P(k\text{PJets})} . \tag{6.6}$$

The efficiency to detect an event with j particle jets on detector level is given by:

$$\epsilon_j = \sum_{i=1}^{n_{max}} P(i\text{DJets}|j\text{PJets}) . \tag{6.7}$$

Since no events with detector jets get lost, it has to be:

$$\sum_{j=1}^{n_{max}} P(j\text{PJets}|i\text{DJets}) = 1 \tag{6.8}$$

If $N(i\text{Djets})$ is the number of events with i jets seen by the detector, one can calculate the number of events with j true jets $M(j\text{PJets})$ on particle level with the knowledge of the conditional probability $P(j\text{PJets}|i\text{DJets})$:

$$M(jPJets) = \frac{1}{\epsilon_j} \sum_{i=1}^{n_{max}} N(i\text{Djets}) \cdot P(j\text{PJets}|i\text{DJets}) \tag{6.9}$$

$$\Rightarrow \quad P(j\text{PJets}) = \frac{M(j\text{PJets})}{\sum_{k=0}^{n_{max}} M(k\text{PJets})} . \tag{6.10}$$

The conditional probability $P(j\text{PJets}|i\text{DJets})$ is calculated in an iterative process starting with an initial probability $P_0(j\text{PJets})$:

$$P(j\text{PJets}|i\text{DJets}) = \frac{P(i\text{DJets}|j\text{PJets}) \cdot P_0(j\text{PJets})}{\sum_{k=0}^{n_{max}} P(i\text{DJets}|k\text{PJets}) \cdot P_0(k\text{PJets})} . \tag{6.11}$$

Using equation 6.9 and 6.10 one can calculate a new probability $P_0(j\text{PJets}) = P(j\text{PJets})$ and start the process again. The initial probability $P_0(j\text{Pjets})$ is assumed to be distributed uniformly. 100 iteration steps are made, then the result is stable.

6.3 Error calculation

Different sources of errors have to be taken into account. Most of them are implemented in the unfolding algorithm.

- **statistical error in data**
  To see what influence the statistical error $\sigma_{\text{stat}} \propto \sqrt{N_{\text{events}}}$ has on the result of the unfolding, the particle level jet rate is calculated for different hypothetical detector level rates. These rates are distributed according to Poisson statistics of the original number of events in each detector jet multiplicity class.

- **jet energy scale error**
  As already explained in chapter 5, the influence of this error on the cross section is estimated by varying the jet energy scale one σ_{jes} up and one σ_{jes} down.

- **statistical error in the Monte Carlo used for unfolding**
  Similar to the statistical error in the data, the numbers of Monte Carlo events used for the conditional probability $P(i\text{Djets}|j\text{Pjets})$ are varied according to Poisson statistics. This was done 10^6 times, while varying the data at the same time.

- **systematic errors in Monte Carlo simulations**
  The Monte Carlo events and cross sections have different uncertainties. The hadronisation process is not fully understood, it can be estimated by comparing the parton level jets with particle level jets. Also the choice of the parton distribution of the proton influences the results. The major uncertainty is due to missing higher orders. All these effects were studied in [33], the combination of these three sources of systematic errors leads to errors of the total cross sections $\sigma_{n\text{jet}}$ for n jet production. They are given by the factors f which have to be applied in both directions (see Tab.6.2, the true value is in the interval $\left(\frac{1}{f_n} \cdot \sigma_{n\text{jet}},\ f_n \cdot \sigma_{n\text{jet}}\right)$. Since these factors are correlated, the error on the n jet rate relative to the 2 jet rate is f_n/f_2 (see Tab. 6.2).

- **error due to the unfolding**
  The error of the unfolding algorithm was estimated by using two independent Monte Carlo samples, one was used for the unfolding and the other one was treated as data. The output of the unfolding was compared with the expexted distribution for particle jets. It differs up to 10% from the true value, but this is consistent with statistics.

Because a ratio of cross sections is studied, the error on the luminosity measurement cancels itself out. The error due to theoretical uncertainties, e.g. the parton density function is minimised by this approach as well.

n jets	2	3	4	5	6
f	1.4	1.7	2.0	2.3	2.6
f_n/f_2	1	1.2	1.4	1.6	1.9

Table 6.2: *Systematic errors of the n jet cross section $\sigma_{n\,jet}$ from the* ALPGEN *Monte Carlo generator. The true value of the cross section (1σ) is in the interval $\left(\frac{1}{f_n} \cdot \sigma_{njet},\ f_n \cdot \sigma_{njet}\right)$*

6.4 Results

As mentioned earlier, the detector jet rate for multiplicities up to three is determined using the `JT_15TT` trigger. For higher rates the `4JT10` trigger was used. Five events with even seven jets were found. These events are included in the six and more jet-class. One of these events is displayed in Fig. 6.2, while the jets properties are listed in Tab. 6.3

In the following "jet" ratio is the cross section of events containing n jets relative to the cross section of events containing two jets. This ratio measured on detector level is given in Tab. 6.4. The particle jet rate was determined using the unfolding algorithm described in section 6.2. All errors mentioned in section 6.3 are included in Tab. 6.4 . The fact that the relative error of the five jet rate is higher than in the six jet rate is due to the fact that the entries in the unfolding matrix $P(i\text{Djets}|j\text{Pjets})$ are chosen randomly according to the original entries derived from Monte Carlo. One of the entries in $P(i\text{Djets}|5\text{Pjets})$ arises from only one event in this class, thus the error is of the same magnitude. The corresponding values for the particle level rates in the Monte Carlo simulated samples are given in Tab. 6.4, too. Again the detector level rates are given as reference. Pythia only produces entries for events with up to four jets, this is the reason why the five and six-jet-rates are missing.

The large errors in the data jet ratios arise mainly from the uncertainty on the jet energy scale in particular for the high jet multiplicities. In the five-jet-class this error is already $\approx$80%, in the six-jet-class it is $\approx$100%. In the Alpgen prediction the errors are to a large extent due to the systematic errors, although the statistical error still makes up a non-negligible part of the total error. The unfolding process is accompanied by a lage uncertainty since only limited statistics of the Alpgen Monte Carlo were available for the analysis.

A graphic comparison of the particle level rates is given in Fig. 6.3. The agreement between data and simulation is reasonable. Except for the last bin the Alpgen Monte Carlo prediction is higher than the data for detector level as well as particle level. One reason for this behaviour of the last bin is that only multiplicities with up to six partons were generated. But events with seven of more partons have probably a great influence on this class. And in the data the six-jet-class includes all events with six and more jets. The detector level ratios are all lower than the particle level ratios. This meets the expectations as the detector and the reconstruction are not fully efficient.

The ratio determined with the Pythia Monte Carlo is lower than the Alpgen prediction, as is expected for a generator not using the exact matrix elements for the higher multiplicities.

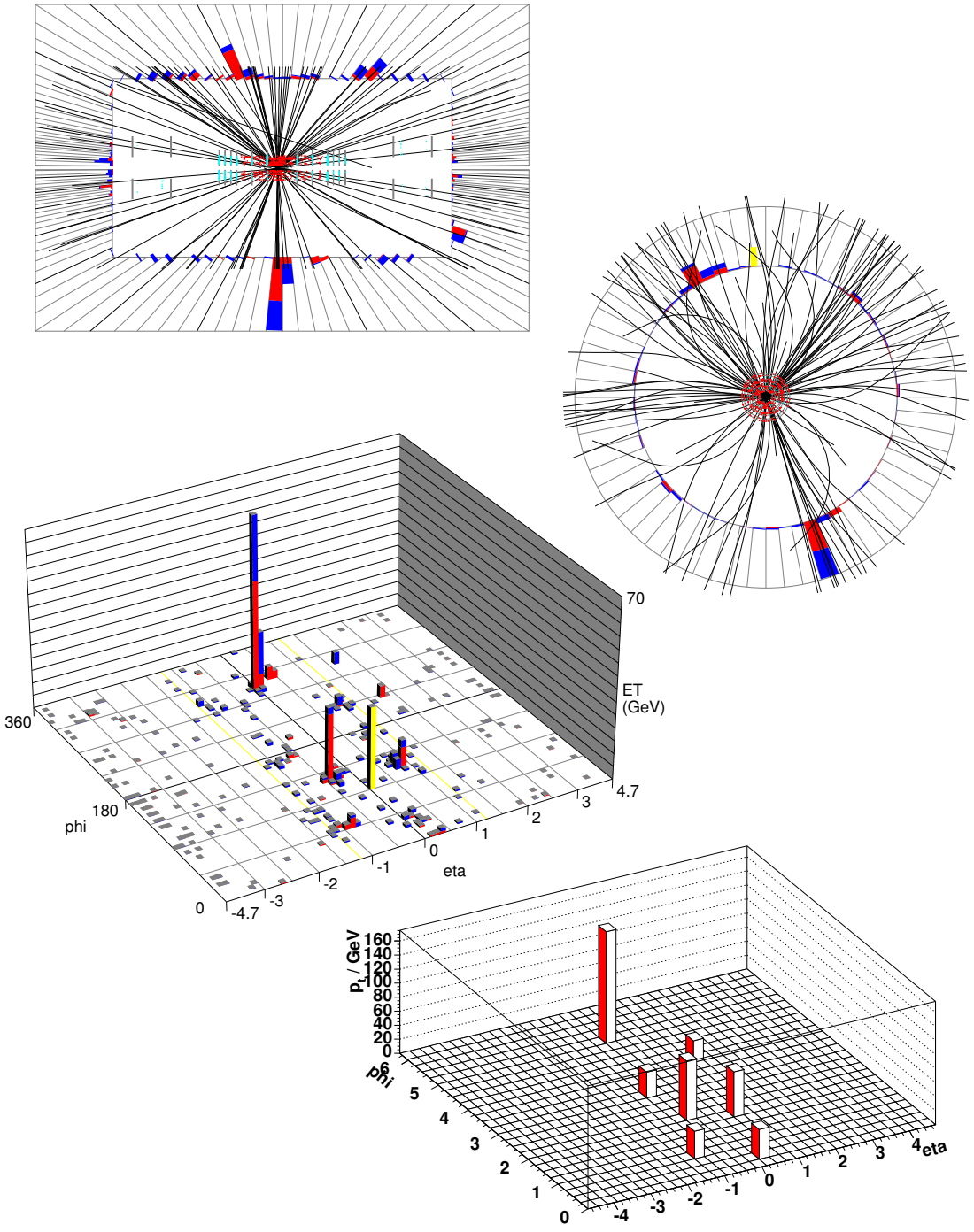

Figure 6.2: *An event with seven reconstructed jets. At the top left, a side view of the detector is given. At the top right, the view is along the beam pipe. At the bottom the energy depositions in the calorimeter (left) are compared with the reconstructed jets (right). The highest transverse momentum of a jet in this sample is* 159 GeV. *The transverse momenta as well as* η *and* φ *of all seven jets are given in Tab. 6.3*

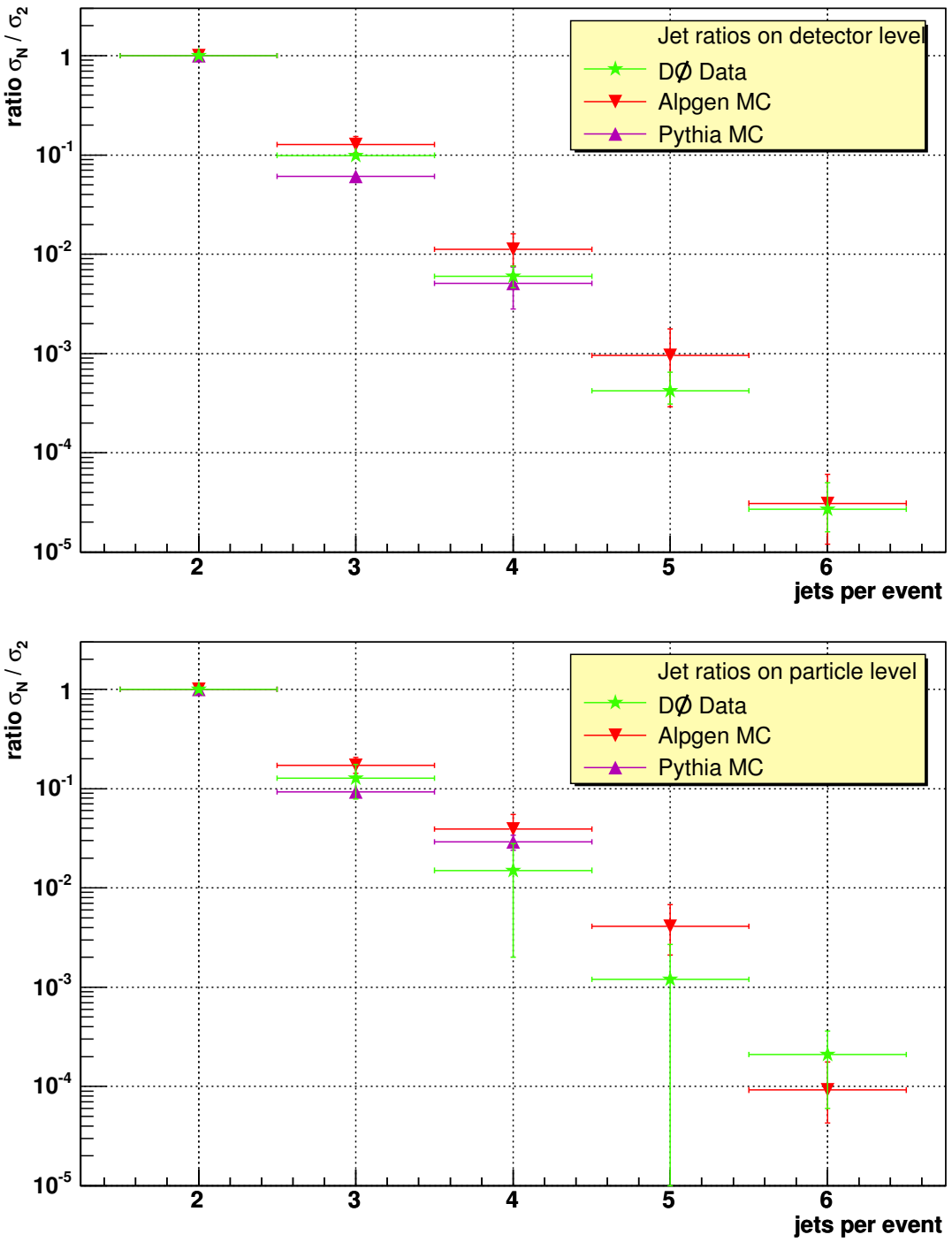

Figure 6.3: *The number of events with n jets related to the number of events with 2 jets on detector level (top) and particle level (bottom) for events containing at least one jet with* $p_T > 50$ GeV. *Only jets with* $|\eta| < 2.4$ *and* $p_T > 30$ GeV *are used. The data jet multiplicities are unfolded from detector level jets to particle level jets with the algorithm explained. All systematic and statistical errors are taken into account for the data and* ALPGEN *Monte Carlo events. For the* PYTHIA *Monte Carlo ratio, only statistical errors are given.*

jet	1	2	3	4	5	6	7
p_T / [GeV]	159.2	85.0	64.3	41.5	39.5	36.7	31.0
η	0.02	-0.40	0.83	0.20	-1.04	-0.65	1.29
φ	5.07	2.12	2.00	0.34	0.91	3.13	3.96

Table 6.3: *The properties of a seven-jet-event. The corresponding event displays are shown in Fig. 6.2*

n jets	DØ data	
	detector rate	particle rate
2	1	1
3	$(0.99 \pm 0.07) \cdot 10^{-1}$	$(1.27 \pm 0.48) \cdot 10^{-1}$
4	$(6.0^{+1.6}_{-1.4}) \cdot 10^{-3}$	$(1.5 \pm 1.3) \cdot 10^{-2}$
5	$(4.2^{+2.3}_{-1.1}) \cdot 10^{-4}$	$(1.2^{+1.5}_{-1.2}) \cdot 10^{-3}$
6	$(2.7^{+3.0}_{-1.6}) \cdot 10^{-5}$	$(2.1 \pm 1.3) \cdot 10^{-4}$
n jets	ALPGEN Monte Carlo	
	detector rate	particle rate
2	1	1
3	$(1.27^{+0.26}_{-0.22}) \cdot 10^{-1}$	$(1.71^{+0.35}_{-0.29}) \cdot 10^{-1}$
4	$(1.12^{+0.48}_{-0.36}) \cdot 10^{-2}$	$(3.9^{+1.6}_{-1.2}) \cdot 10^{-2}$
5	$(0.96^{+0.81}_{-0.67}) \cdot 10^{-3}$	$(4.1^{+2.7}_{-2.0}) \cdot 10^{-3}$
6	$(3.1^{+3.0}_{-1.9}) \cdot 10^{-5}$	$(9.2^{+8.5}_{-4.9}) \cdot 10^{-5}$
n jets	PYTHIA Monte Carlo	
	detector rate	particle rate
2	1	1
3	$(6.1 \pm 0.6) \cdot 10^{-2}$	$(9.3 \pm 0.9) \cdot 10^{-2}$
4	$(5.1 \pm 2.3) \cdot 10^{-3}$	$(2.9 \pm 0.5) \cdot 10^{-2}$

Table 6.4: *Ratio for multijet production normalised to the 2 jet rate, data from DØ is compared with an* ALPGEN *and* PYTHIA *prediction. The particle rate for DØ data is the result of the unfolding process. For data and* ALPGEN *Monte Carlo rates all errors are included. For* PYTHIA *Monte Carlo rates, only the statistical error is given. No jet multiplicities higher than four were observed in the* PYTHIA *Monte Carlo simulation*

Chapter 7

Conclusions

The important process of jet production at hadron colliders was studied in this analysis in two different ways.

A measurement of the inclusive jet cross section $d\sigma/dp_T$ integrated over five different η regions was presented. These regions are: $|\eta| < 0.5$, $0.5 < |\eta| < 1.0$, $1.0 < |\eta| < 1.5$, $1.5 < |\eta| < 2.0$ and $2.0 < |\eta| < 2.4$. A good agreement with a next to leading order NLOJET++ prediction was found. Some small deviations in the Inter Cryostat regions indicate an incomplete understanding of this part of the detector.

The multijet production was examined by studying the ratio of the cross section for n jets ($n = 3..6$) whithin $|\eta| < 2.4$ relative to the cross section for two jets, requiring a transverse momentum of at least 50 GeV for the leading jet and 30 GeV for all other jets. The data at detector level was unfolded with a Bayesian approach to be able to compare the measured ratios with the expected ratios at particle level. The results agree with the prediction from an ALPGEN Monte Carlo with full detector simulation for all jet multiplicities, although the simulation tends to be slightly above the measured data. Additionally, the data was compared to a PYHTIA Monte Carlo prediction with full detector simulation for the three and four-jet ratio. Here, too, the data agreed with the predictions. Five and six-jet ratios were not compared, since the model PYTHIA uses does not produce any multiplicities higher than four. This analysis could improve a lot if more events generated with ALPGEN were available. This would minimise the uncertainty due to the unfolding process.

Both of the analyses show that QCD is understood to a large degree, but in order to be able to gain more information much work will have to be done to reduce the dominant source of uncertainty in the measurements, namely the Jet Energy Scale. Unless no improvement in this sector is made, the reduction of the statistical error by using more data is useless. This reduction is also desirable from the point of view of new physics. Small deviations from QCD predictions indicating such new phenomena will only be found if the error on the measurement becomes small.

Bibliography

[1] DESY. TESLA, an international, interdisciplinary center for research, 2001. http://tesla.desy.de/new_pages/TDR_CD/brochure/.

[2] E. Noether. Invariante variationsprobleme. *Nachr. d. König. Gesellsch. d. Wiss. zu Göttingen, Math-phys. Klasse*, pages 235–257, 1918.

[3] S. Eidelman et al. Review of particle physics. *Physics Letters B*, 592:160–165, 2004.

[4] Christoph Berger. *Elementarteilchenphysik*. Springer, 2002.

[5] Peter Schmüser. *Feynman-Graphen und Eichtheorien für Experimentalphysiker*. Springer, 1995.

[6] S. Eidelman et al. Review of particle physics. *Physics Letters B*, 592:104–113, 2004.

[7] S. Eidelman et al. Review of particle physics. *Physics Letters B*, 592:169, 2004.

[8] Fermilab Beams Devision. Run II Handbook. Fermilab Beams Devision Run II webpage. http://www-bd.fnal.gov/runII/index.html.

[9] Visual Media Services FERMILAB USA. Photo database. http://vmsfmp2.fnal.gov/v1/VMSChoice.htm.

[10] S. Abachi et al. The DØ detector. *Nucl. Instrum. Meth.*, A338:185–253, 1994.

[11] S. Abachi et al. The DØ upgrade: The detector and its physics. FERMILAB-PUB-96-357-E.

[12] Gregory Arthur Davis. *First Measurement of the Differential Inclusive Cross Section for Jet Production at DØ Run II*. PhD thesis, University of Rochester, 2004.

[13] DØ Physics detector drawings. http://www-d0.fnal.gov/Run2Physics/WWW/drawings.htm.

[14] DØ Top Group. DØ Top Analysis and Data Sample for the Winter Conferences 2004. DØ Note 4419, 2004.

[15] What is SAM (Sequential data Access via Meta-data). http://projects.fnal.gov/samgrid/WhatisSAM.html.

[16] Gerald C. Blazey et al. Run II jet physics. In U. Baur, R.K. Ellis, and D. Zeppenfeld, editors, *QCD and Weak Boson Physics in Run II*, pages 47–77, 2000. FERMILAB-PUB-00/297.

[17] http://www-subatech.in2p3.fr/ photons/subatech/physics/collisionneurs/node58.html.

[18] Alexander Kupčo. Jet energy scale and resolution in the DØ calorimeter. Talk given at CALOR'04, 2004.

[19] Torbjorn Sjostrand et al. High-energy-physics event generation with PYTHIA 6.1. *Comput. Phys. Commun.*, 135:238–259, 2001.

[20] Rene Brun and Fons Rademakers. ROOT - An Object Oriented Data Analysis Framework, Users Guide 3.05. 2001.

[21] Markus Klute, Lukas Phaf, and Daniel Whiteson. TopAnalyze - a framework analyze package for top group analyses. DØ Note 4122, 2003.

[22] Michelangelo L. Mangano, Mauro Moretti, Fulvio Piccinini, Roberto Pittau, and Antonio D. Polosa. ALPGEN, a generator for hard multiparton processes in hadronic collisions. *JHEP*, 07:001, 2003.

[23] MC_Runjob webpage. http://www-clued0.fnal.gov/runjob/.

[24] Common Sample Group main page. `http://www-d0.fnal.gov/Run2Physics/cs/index.html`.

[25] Offline Run Quality Database. `http://d0db-prd.fnal.gov/qualitygrabber/qualQueries.html`.

[26] Laurent Duflot, Viatcheslav Shary, Robert Zitoun, and Ingo Torchiani. cal_event_quality package. DØ Note 4614, 2004.

[27] The good luminosity block selection for JET/MET available at the web page. `http://www-clued0.fnal.gov/~pverdier/d0_private/MetRunSel/`.

[28] Certified Jet Energy Scale (jetcorr v5.3) for data with r=0.7 cone without t42 algorithm. `http://www-d0.fnal.gov/phys_id/jes/d0_private/certified/certified.html`.

[29] D Elvira. Jet Energy Scale at DØ. DØ Note 4614, 2004.

[30] Glen Cowan. *Statistical Datat Analysis*, chapter 2. Oxford University Press, 1998.

[31] Zoltan Nagy. Next-to-leading order calculation of three-jet observables in hadron hadron collision. *Phys. Rev.*, D68:094002, 2003.

[32] DØ QCD Group. Measurement of inclusive jet and dijet cross sections. DØ Note 4382, 2004.

[33] Thomas Hebbeker. What to do with Multijet Events. DØ Note 4465, 2004.

[34] G. D'Agostini. A multidimensional unfolding method based on Bayes' theorem. *Nucl. Instrum. Meth.*, A362:487–498, 1995.

Acknowledgements

First of all I would like to thank my parents which made it possible for me to study, visit Edinburgh for a year and supported me in all situations.

Furthermore I would like to thank the following persons, which played an important role in the completion of this work:

- Prof. Hebbeker for giving me the opportunity to write this thesis, as well as for the help on Monte Carlo production, statistics and many other topics. I am greatful that I had the possibility to visit Fermilab where I was able to see the detector from inside.
- Prof. Erdmann for agreeing to be my second referee and for giving me new ideas from an outside point of view.
- my colleges of the local DØ group in Aachen, as well as the former members. They were all a great help and answerd many questions I came up with. In particluar I would like to thank Philipp for the sweet supply.
- Christian Autermann, Philipp Biallaß, Michael Bontenackels, Roland Heinesch, Martin Holtschneider, Daniela Käfer , Josi and Peter Marsden and Frank Reininghaus for proof-reading this thesis.
- Markus Wobisch for answering all mails concerning jets and nexst to leading order calculations.
- All my friends, for compensating for the work and its problems with their indispensable companion and cheering up, and for numerous good times at parties having nothing to do with Physics.

Eventually I would like to thank my boyfriend Bernd, just for being there for me.